Freeze Casting ,

Ulrike G. K. Wegst[1,2,*], Paul H. Kamm[2,3,†], Kaiyang Yin[4,†], Francisco García-Moreno[2,3,*]

[1] Biomimetic Design Laboratory, Department of Physics, Northeastern University, Boston, MA, USA
[2] Process Imaging Laboratory, Institute of Materials Science and Technology, Technische Universität Berlin, Berlin, Germany
[3] Process Imaging Laboratory, Institute of Applied Materials, Helmholtz-Zentrum Berlin für Materialien und Energie, Berlin, Germany
[4] Laboratory of Micro and Materials Mechanics, Department of Microsystems Engineering, University of Freiburg, Freiburg, Germany

† These authors contributed equally to this work.

* Corresponding authors.
ulrike.wegst@northeastern.edu;garcia-moreno@helmholtz-berlin.de;

Abstract

When solutions and slurries are directionally solidified, complex dynamics of solvent crystal growth and solvent-templating processes determine the structure formation and final hierarchical architecture of the freeze-cast material. By employing continuous X-ray tomoscopy, it is now possible to study and quantify in situ, time-resolved, and in 3D otherwise elusive, intricate ice crystal growth phenomena, which define a variety of performance-defining features at several length scales of the resulting cellular solids. These phenomena are responsible not only for the material's pore morphology at the first level of the hierarchy, but also the molecular, fibrillar, and particle self-assembly of the components that form the cell walls, at the second, and the typically unilateral cell wall surface structures, at the third. What makes the freeze casting process attractive is that the features of the final hierarchical material architecture, which determine the structural, mechanical, and physical properties of freeze-cast materials, can be custom-designed for a given application. Overall porosity, pore size, geometry, and orientation, for example, as well as particle packing within the cell walls of the cellular solid, and cell wall surface features can be tailored for applications that range from biomedical materials to components for energy generation and storage, and power conversion.

[H1] Introduction

The freeze casting **[G]** process is based on the directional solidification **[G]** of solutions or particle slurries, Figure 1, Box 1. It is a two-step process: first a solution or slurry is directionally solidified, then the solid solvent phase is removed either by sublimation, thus via freeze drying (lyophilization), or by solvent exchange.[1–5] In the case of freeze-cast ceramics and metals, the samples are sometimes analysed and used in the form of "green bodies"[6–8] but are more frequently first sintered [9–16] or carbonised,[17,18] or otherwise thermally or chemically treated and used only after this third processing step.[19,20] Because structure formation occurs primarily during solidification, we focus, here, on crystal growth and solvent-templating phenomena.[21] However, we also briefly introduce the effects of the lyophilization and sintering steps on the material structure.

A number of solvents, such as water, camphene,[22] cyclohexane,[23] cyclooctane,[23] dimethyl carbonate,[23] dioxane,[23] naphthalene-camphor,[9] tert-butyl alcohol (TBA),[24] and TBA-cyclohexane,[25] have been investigated. We focus in this primer on aqueous material systems, since these are the most studied and still dominate the field. However, most of the principles and phenomena, and the respective characterization techniques we describe are applicable also to other solvent systems. Initially investigated primarily as a batch process, freeze casting has matured and progressed to include also continuous material production routes in recent years.[26,27] Collated, the various discoveries made over the past 40+ years ease the custom-design and manufacture by freeze casting of materials with new and improved properties.

Fundamental to the freeze casting process are ice crystal growth phenomena, because predominantly the ice phase shapes the architecture of the final material. Aiming to enable the custom design of materials, initially primarily empirical research was performed with a focus on robust structure-property-processing correlations.[28–33] Increasingly, researchers took a more science-based approach applying a variety of newly-developed experimental and simulation tools and techniques. With these, new insights could be gained and a significantly improved fundamental understanding of the physics of ice crystal growth and structure formation by ice-templating **[G]** could be obtained.[21,34] Since complex dynamics of solvent crystal growth and solvent-templating processes determine the final hierarchical architecture with at least three length scales of structural features of freeze-cast materials,[5,21] one characterization technique, continuous X-ray tomoscopy, was found to be particularly well suited to study the freeze casting process.

X-ray tomoscopy is time-resolved X-ray tomography.[35–37] X-ray tomography is an imaging technique that takes advantage of the short wavelengths of X-rays of 10^{-9}–10^{-11} m, which is about 1000 times shorter than that of visible light ($4–7 \cdot 10^{-7}$ m).[38,39] Because of the shorter wavelength, a significantly higher spatial resolution **[G]** can be achieved with X-rays than with visible light. Recently, over 2,000 tomograms per second **[G]** (tps) have been achieved with synchrotron X-rays.[35,36,40] X-ray tomoscopy is considerably more powerful than post mortem or sequential X-ray tomography and sequential or continuous 2D radiography, which is also known as radioscopy, because artefacts due to feature overlap and sequential X-ray illumination are avoided;[41–43] Tomoscopy enables the truly continuous 3D imaging for prolonged periods of time of several minutes.[37]

Since complex dynamics of solvent crystal growth and solvent-templating processes determine the final hierarchical architecture with at least three length scales of structural features of freeze-cast materials,[5,21] X-ray tomoscopy is particularly well suited to study and quantify in situ in 3D the otherwise elusive and intricate crystal growth phenomena which define the performance-defining features at several length scales of the resulting cellular solids.[34–36] We highlight, here, the advantages of X-ray tomoscopy, which was specifically developed for the time-resolved, in situ observation in 3D of dynamic phenomena during materials processing and structure formation and evolution [34,39,44–47] and discuss challenges and opportunities encountered, when it is applied to analyse and quantify the dynamics of the freeze casting process in 3D[34].

With this Primer, we wish to provide a broad, introductory overview of the manufacture of materials by freeze casting rather than a comprehensive review. We address both experimental techniques and the state-of-the-art fundamental science of structure formation during ice templating of polymer, ceramic, metals, and composite systems. Additionally, a range of sample preparation and material characterization techniques and tools are introduced, accompanied with illustrative examples, contrasting, where appropriate, advantages and disadvantages of static versus dynamic approaches.

In particular, we highlight the X-ray tomoscopy technique and illustrate how unique and powerful they are for a quantitative in situ analysis of the dynamics of crystal growth and ice-templating processes that determine the hierarchical architecture of freeze-cast materials.[21,34] Tomoscopy possesses the required spatio-temporal resolution to capture the evolution of dynamic crystal growth and solvent-templating phenomena that are otherwise elusive and inaccessible with ex situ methods.[34] We illustrate, how structure-processing and structure-property correlations are determined, on the basis of which it is possible to formulate structure-property-processing corelations for the custom-design of materials for a given application. How broadly the resulting freeze-cast materials can be applied is illustrated with examples, which show what makes freeze-cast polymers, ceramics, metals, and their composites so attractive for use in the rather diverse fields of biomedicine, environmental engineering, and energy generation and storage. In our outlook, we highlight challenges and opportunities for freeze casting as a manufacturing process and X-ray tomoscopy as the currently only technique with which the dynamics of the freeze-casting process can be captured in real time and 3D.

[H1] Experimentation

Illustrated in Figures 2 are several of different freeze casting moulds and systems for batch and continuous processing with which the temperature gradient that drives the directional solidification can be defined and structure formation can be controlled, also in the absence or presence of externally applied fields. Additional mould options are shown in Figure S2-S3.

[H2] The Freeze Casting Process

The schematic of Figure 1a illustrates the directional solidification process of an aqueous polymer solution and its phase-separation into pure ice (blue) and a second phase (red), here a polymer.[21] A frequently used freeze casting set-up is shown. For ease of sample removal, a PTFE (polytetrafluoroethylene) mould is sealed with a copper bottom plate and filled with an aqueous solution or slurry. [5] The mould is placed on a copper coldfinger, which is frequently cooled by liquid nitrogen and equipped with a band heater near the top to adjust the coldfinger surface temperature and cooling rate, $\dot{C}$, via a PID (proportional–integral–derivative) controller[3,4,21,48,49]. A controlled cooling rate, frequently in the range of $\dot{C} = 0.1 - 10$ °C/min [7,28–30,50–52], is applied. When the mould bottom is sufficiently undercooled, ice crystals nucleate on its surface. [53,54] Because nucleation **[G]** control in freeze casting is a rather complex subject in its own right, [55] it is beyond the scope of this primer.

The initially high cooling rate upon nucleation results in a textureless chill zone consisting of fine, equiaxed grains. Competitive crystal growth follows in the general direction of maximum heat flow, which is imposed by the thermal gradient **[G]** , *G*.[56] Grains, whose fastest crystal growth direction $\langle 11\bar{2}0 \rangle$ (Figure 1a insert) is most closely aligned with the thermal gradient, eliminate less favourably oriented ones, and define both the size and the orientation of the domains **[G].** The domains are defined by their uniform lamellar orientation[2] due to dendritic ice crystal growth **[G]**.

In the beginning, each of the winning grains possesses an approximately planar freezing front which progresses at a velocity, *v*, with solute (and particles) being partitioned into the

liquid phase. [7,34,56–58] As a result, the freezing front pushes ahead of it an exponentially decaying concentration profile, $C > C_0$, defined by a solutal diffusion length (Figure 1a insert):

$$l_D = D/v \quad \text{Eq 1}$$

where C_0 is the initial solute concentration, and D is the diffusion coefficient in the liquid phase[21].

The solute build up ahead of the freezing front causes the planar freezing front to become constitutionally supercooled and thermodynamically unstable once the ratio v/G exceeds a threshold value that is dependent on the composition of the solution or slurry.[21,59] The constitutional supercooling provides the driving force for a phase separation **[G]** to occur, due to which morphological instabilities in the form of sinusoidal perturbations form; these initial instabilities are named after Mullins and Sekerka,[60] who first studied them. The ensuing competition between destabilizing solute diffusion in the liquid phase, the temperature gradients at small and large wavelengths, respectively, and restabilizing capillarity effects amplify the perturbations until a preferred wavelength, λ_0, for a given set of material and processing parameters is reached. This wavelength defines the lamellar spacing of the initially cellular, then dendritic ice crystal growth. Because water solidifies pure, solute (or solute and particles) form a second interdendritic phase which is templated by the ice-crystal growth.[21,34]

The ice crystal growth characteristics determine both the pore size **[G]**, shape, and alignment, within the lyophilized material and predominantly unilateral surface features on the cell walls detailed in. Partially faceted, anisotropic ice crystal growth and the crystal growth instabilities that form during directional solidification are responsible for the morphology of the various cell wall surface features: 1) smooth "ridges," which may be partially detached; (2) ridges with triangular, "shark teeth"-like undulating tips; (3) "jellyfish caps," where two ridges merge and continue as one; (4) "jellyfish tentacle"-like extensions, which may form part of a "jellyfish array" or "ridge," and can be partially or completely detached along their length; and (5) wavy or wrinkled cell walls. [21,34]

Figure 1b illustrates how, along the height of the sample, freeze cast scaffolds reflect the progression of crystal growth: first a chill layer of higher density with small ice crystals or pores after lyophilization, second, a cellular layer, and third a lamellar layer [31]. Transverse and longitudinal cross sections of the freeze cast chitosan scaffolds (figures adapted from [21]) are shown to highlight the highly anisotropic material structure and aligned honeycomb-like porosity which results from directional solidification.[33,61] The schematic in Figure 1c of a freeze cast collagen scaffold, highlights fibrillar pillars and bridges, which are typical features when fibrillar slurries composed, for example, of collagen or nanocellulose, are freeze cast.[29] Additionally shown are the differences in particle packing within the cell walls of small and large particles, and their bimodal mix (7:3 large:small), and platelets. [22,2.] All of these structural features affect the property profile and performance of freeze-cast materials.

The experimentally obtaines counterparts to the schematics shown in Figure 1 are presented in Figure S1. In Figure S1Aa, the transverse cross section of an ice-polymer composite is shown in its still frozen state, revealing ice-templated ridges on the polymer lamellae [2]. Figures S1Ab-d show on the cell walls of chitosan scaffolds [21] the unilateral cell wall features (1) to (5) defined in the schematic of Figure 1a. Figures S1Ba-d depict transverse and longitudinal cross sections of a freeze cast collagen scaffolds which exhibit fibrillar pillars and bridges. [29] Figures S1Ca-d show examples of particle packing in the cell wall consisting of (Ca) small particles, (Cb) a bimodal particle size distribution, (Cc) large particles, and (Cd) platelets forming a nacre-like structure. [7,8]

While the various material-dependent microstructures and architectures of freeze-cast materials are primarily formed during the processing step of directional solidification, one should additionally be aware of the fundamentals of the second processing step of lyophilization to ensure that suitable freeze-drying parameters are chosen and appropriate corrections to these are made, when samples emerge deformed or cracked. Once the sample is completely solidified, it is placed in a lyophilizer to remove the ice phase by freeze drying. By converting the

ice phase into vapor without first forming a liquid phase, which would happen at ambient conditions, it is possible to preserve the ice-templated sample structure.

Typical freeze-cast samples consist predominantly of the solvent water. The solute and particles that, during directional solidification, become increasingly upconcentrated in the interdendritic spaces possesses a freezing temperature lower than that of water. This means that samples may appear to be fully frozen before the second solute-rich phase has reached its phase transition temperature. However, only when also this second phase, which depending on its composition forms either a eutectic or a polymeric glass, has reached its eutectic or glass transition temperature, respectively, is the sample fully solidified. For the freeze-drying process to be successful, it is critical that the sample is placed in a lyophilizer whose cold trap (ice collector) is at least 20 °C cooler than the eutectic or glass transition temperatures.

Freeze drying is a two-step process. Primary drying of the sample by sublimation begins, when sample temperature and chamber pressure correspond to the sublimation conditions defined by the sublimation line on the pressure-temperature phase diagram (Supplementary Figure S?). Secondary drying starts, once the pure ice phase has been removed completely, and remnant moisture (frequently the 5-8%) bound to the cell wall material is removed by isothermal desorption. This secondary drying step typically takes up to one third of the overall drying time.

Misleading can be that the sample feels dry already after the primary drying step. When, for example, purely polymeric samples emerge deformed from the lyophilizer, exhibiting an hourglass rather than a regular cylindrical wine-cork-like shape, residual moisture which acts as a plasticizer was likely retained permitting plastic sample deformation to occur when forces due to the vacuum were acting on it. In the case of freeze-cast slurries, these factors and non-uniform drying of the green bodies can cause cracks to form during lyophilization. Reasons for retained moisture tend do be incomplete freezing or incomplete drying of the solute phase. Both factors can readily be corrected with adjustments of freezing and drying parameters.

Originally, freeze casting started as a batch process, for which a great variety of moulds were developed over the years to expand the process' capabilities. Also the process itself has been adapted, to include, for additional structure control, the application of external fields while directionally solidifying a sample (Figures 2a-e, S2a-f). More recently, continuous freeze-casting processes have been added to the portfolio (Figures S3a-d). Fundamental to all of these variations of the process is a means to apply a well-controlled thermal gradient, G, to drive the directional solidification of the sample in a controlled fashion, meaning with a reproducible applied and local cooling rate **[G]**, $\dot{C}$, or freezing front velocity **[G]** , v, to achieve materials in a reproducible fashion (Figures 1a).

[H2] Batch Freeze Casting

[H3] Unilateral and bi-lateral cooling

When freeze casting in batches, one or more samples are made simultaneously in one or more moulds. Most commonly, the thermal gradient in the mould is generated in the vertical direction and parallel to the mould axis (Figures 1a, 2a). While close to steady-state and unidirectional crystal growth conditions and thereby close to constant lamellar spacing **[G]** can be achieved with a unilateral mould cooling configuration[5,33,49], bi-lateral cooling permits to obtain true steady-state conditions by, for example, lowering the top and bottom mould temperature in parallel with a mould that is thermally highly conductive at one or two opposing sides of the mould in contact with a cold source (Figure 2b).[52,62] Double sided moulds also invite a comparison to be made between bottom up (against the gravity vector) and top down (parallel to the gravity vector) freeze casting and their respective effects on ice crystal growth and structure formation.[63] Samples prepared in these types of moulds typically possess a polydomain structure.[64] The moulds frequently are 50-60 mm high with one large, e.g. 18-20 mm diameter, or several small diameter, e.g. five to seven 2 mm diameter, bores.

[H3] Thermocouple moulds

An essential tool to determine fundamental directional solidification parameters, also for modelling purposes, is a mould, compatible with the freeze casting system in question, that is equipped with an array of regularly spaced thermocouples to determine how the temperature in the sample changes along the height of the mould as a function of applied cooling rate **[G]**. From these measurements, the local cooling rate, $\dot{C}_{\mathrm{loc}}$, can be determined for each thermocouple position. For example, plotting temperature contours for the phase transition temperature of a given material system, such as 0 °C in the case of pure water or diluted aqueous solutions, the freezing front velocity, *v*, can be determined and the temperature gradient, *G*, at the solid-liquid interface can be calculated (Figure S2a).[7,21,52,65]

[H3] Thermal gradient design

Adding an insulating wedge to the cooled surface, usually in a mould with a square or rectangular cross-section, drives large area monodomain formation by grain selection. Ice nucleation initiates along the well-defined straight line formed by the wedge-mould bottom interface, the orientation of the effective thermal gradient, *G*, in the mould is the sum of the applied vertical and a horizontal component that depends on the wedge angle, while isotherms parallel the edge of the wedge (Figure 2c).[66,67] This means that a second driving force for grain selection exists, in contrast to the traditional flat mould bottom, in which the thermal conditions perpendicular to *G* are sufficiently equivalent, so that the alignment of the ice lamellae within the selected domains is effectively random.

As in the case of a flat bottom mould (Figure 1), domains with the fastest ice crystal growth direction $\langle 11\bar{2}0 \rangle$ most closely aligned with the effective thermal gradient are favored also in the presence of the insulating wedge. Of these domains those dominate, whose ice crystal lamellae are with their second fastest growth direction $\langle 1\bar{1}00 \rangle$ best aligned with the lateral thermal gradient component. The result is, again, a honeycomb-like scaffold structure, which is characterized by a unidirectionally aligned porosity. However, instead of a polydomain structure with random lamellar orientation in the different domains formed without an insulating wedge, the samples possess a large-area monodomain structure with unidirectional lamellar alignment.

Radial thermal and structural gradients result, when the mould bottom is a thermal insulator but either or both the mould itself and an inner pin extract the heat (Figures 2d, S2b).[29] One or two layers of radially aligned porosity result, respectively, with a chill-zone on the cooled mould surfaces and a membrane-like interfacial layer where the two freezing fronts meet[68–71]. Attractive structural variations can be achieved with both small and large diameter moulds, also through the pairing of mould components with different thermal conductivities (e.g. copper, brass, aluminium, polymers), which allow to control separately the crystal growth velocities, from each mould component at one applied cooling rate with additional control also over the position at which the two freezing fronts meet.[29,32]

Cooling can also be applied from all sides of a mould (Figure S2c)[72,73]. The result is crystal growth roughly toward the geometric centre of the mould, where all growth fronts join and a small pore size is formed; such pore orientation arrangements give rise to negative Poisson's ratio of the material. As in the case of bilateral or radial freezing, an interfacial membrane or layer is formed where freezing fronts meet[71,73]. While a symmetrical mould shape is shown in Figure S2c for this case, moulds can be free-form and take also very complex shapes, with carefully designed thermal gradients to drive crystal growth into the desired directions.

[H3] Applied fields

Additional control over ice crystal growth, pore architecture, particle alignment and cell wall self-assembly, and the resulting material properties can be taken by applying an external magnetic[13,74,75] (Figures 2e, S2d), electric[76,77] (Figure S2e), or acoustic field[78] (Figure S2f), during the directional solidification process.

Most studied is the application of externally applied magnetic fields. Magnetic fields can be uniform or not uniform. When an externally applied magnetic field created by a pair of permanent magnets is applied to a cylindrical mould, the field lines decrease in strength from the outside to the centre of the mould[13] (Figure S2d). Such a non-uniform magnetic field is desired, when the goal is less that of a homogeneous particle distribution and alignment but more one of defined particle redistribution and translation into regions of higher field strength.[79] Rotating such a non-uniform magnetic field during directional solidification results in samples, in which magnetic or surface-magnetized particles form a helix at the sample-mould interface and along the direction of solidification.[13,79]

When a uniform magnetic field is applied during directional solidification, magnetic or magnetized particles can rotate, and thus be re-oriented and aligned without additional particle translation (Figures 2e). A very successful example for this is the alignment of magnetic (Sendust) flakes in a uniform magnetic field, which results not only in a highly organized, nacre-like cell wall structure but also an alignment of the cell walls into a monodomain material structure perpendicular to the freezing direction, thereby forming a honeycomb-like aligned porosity parallel to the freezing direction.[75]

Much less explored than the effect of an externally applied field on the structure and properties of freeze-cast materials are the effects of an externally applied electric field during solidification, which affects structure formation through interactions also with the strongly polar water molecules (Figure S2e).[77]

Most recently, the effects of an externally applied acoustic field have been explored (Figure S2f). Standing ultrasonic waves were found to concentrate particles in their nodes thereby forming concentric rings of alternating low and high particle concentrations. The outcome were samples exhibiting rings of alternating high and low porosities and densities.[78]

[H2] Continuous Freeze Casting

Continuous freeze casting is a mould-free process, which may also be termed freeze-printing or freeze-extrusion (Figure S3). Its advantage over batch processing is that long components with complex cross-sections, or larger components with added architectures, and also surface coatings[70,71] can be manufactured.

The smallest continuously formed freeze-cast components are what one might wish to call 0D particles or droplets, when an appropriate solution, slurry, or ink is sprayed or dripped into a cold bath (e.g. liquid nitrogen) or onto a freeze-cast or frozen sample[70,71] or onto a sacrificial ice core (Figure S3a)[80]. Individual particles and droplets typically have a radial porosity as a result of flash freezing.[81]

Fibres, cylinders, and tubes, thus 1D structures, with a plethora of pore morphologies can be created by freeze spinning and freeze extrusion of liquids or semi-frozen starting materials, which pass through a cold zone that, for a given flow rate, determines through shape and applied thermal gradient, ice crystal growth and through it the templated pore architecture[26,81] (Figure S3b).

Porous sheets, thus 2D structures, can continuously be formed, when a liquid or semi-frozen film of a solution or slurry is passed through a cold zone formed by one or a pair of cooled rollers or an externally applied thermal gradient, through which the material passes on a conveyer belt-like system for directional solidification [82] (Figure S3c). While pore size and orientation are also in this case defined by the magnitude of the thermal gradient and its orientation, along with transport velocity, the porosity typically exhibits a monodomain structure[83–88].

Surface coatings, for example by freeze casting around a sacrificial ice core or spray-frozen onto a freeze-cast scaffold in the frozen or lyophilized scaffold, permit to custom-design a desired property gradient across a sample section (Figure S3d).[70] With these methods, tubular scaffolds can be custom-made for applications that are either homogeneous in structure or require compositional, structural, mechanical, and physical property gradients.[70,71,80]

Complex 3D structures, which can also include multiple structural and performance gradients, can be created when freeze spinning, direct ink writing, or freeze extrusion is performed drop-by-drop or layer-by-layer to add a third dimension[27,71,89,90] , or when freeze casting and 3D printing are combined[91] (Figure S3e). In these processes, a solution or solution with a relatively low viscosity is deposited either on a cold surface, on which the dispensed solution is quickly solidified and turned into a self-supporting structure, or in its partially frozen, yet elastically or plastically deformable state, in a cold reservoir.

Depending, when crystal growth starts and is completed, the resulting 3D structure has a pore alignment primarily oriented perpendicular to the cold plate[27] or predefined by the freeze printing or extrusion process.[26] Sophisticated components with structural and compositional gradients can be formed with coaxial nozzle designs, or through the use of multiple nozzles, which may include also support materials, so that complex geometries can be formed within the material strand and the built-up construct.[27,80]

Freeze-printing and freeze-casting techniques can also be combined, for example, by placing a 3D printed polymer scaffold in a mould filed with a ceramic slurry, to achieve multi-material scaffolds with additional features and levels of complexity introduced to the hierarchical architecture and porosity.[91,92]

[H1] Results

The complex dynamics of solvent crystal growth and solvent-templating processes, which determine structure formation and material properties, can best be assessed in situ (Figure 3). While 2D investigations by optical[93–95] and confocal microscopy[96–99] provided first insights into ice crystal growth and materials assembly during directional solidification (Figure 4A-B), only 3D imaging techniques of sufficiently large size to minimize boundary effects are truly suitable for a quantitative analysis of the freeze casting process. We found X-ray tomoscopy to be particularly powerful and well suited for this purpose (Figures 3, 4Da–Dd).[34]

Post mortem techniques complement in situ material characterization techniques (Figure 4Ea–Id). With cryo-SEM (scanning electron microscopy) and cryo-EBSD (electron back-scatter diffraction), the freeze-cast material structure can be quantified directly after directional solidified by batch or continuous freeze casting, while the ice phase is still present (Figure 4Ga–b).[2] Both the templating ice-crystal orientation and ice-templated material structure can be analysed.[2] However, because cryo-microscopy techniques are rarely available, structural, mechanical, and physical characteristics of the freeze cast cellular solids are most commonly determined, once the sample has been lyophilized and, in the case of ceramics and metals, frequently after an additional processing step of sintering, thermal or chemical reduction, in the case of carbon-based scaffolds, has been performed.

Because lyophilization, sintering, and carbonization tend to cause overall shrinkage and possible shape changes.[14,15] The structure-property-processing correlations required for a better understanding of the fundamental science and mechanisms of freeze casting are best determined on samples that still contain the ice phase. Similarly, correlations required for the custom-design and manufacture for a materials specific application are best obtained in the state in which they will be used, i.e. fully hydrated in the case of polymers or composites for biomedical application (Figure 4Fa–b)[28,29] and sintered or thermally treated in the case of ceramics and metals.

In the remainder of this section, we detail both in situ and post mortem materials characterization techniques that are particularly well suited for an analysis of freeze-cast materials and we illustrate, how materials performance can be evaluated and compared. Finally, we also discuss experimental and statistical considerations and present example structures, properties, and correlations.

[H2] In situ Techniques

Critical for a fundamental understanding of crystal growth and structure formation phenomena is, in addition to a knowledge of the phase diagram, diffusion coefficients, *D*, and correlation between cooling rate, temperature gradient, and freezing front velocity, a thorough knowledge of both the crystal growth morphology and the crystal growth dynamics.[21,56]

[H3] Optical microscopy in 2D

Traditionally, the dynamics of directional solidification is analysed and quantified in 2D using a Bridgman-type gradient freezing stage with samples contained in a Hele-Shaw cell.[94,96–101] (Figure S4). In a Hele-Shaw cell, a thin (0.05–0.2 mm thick material) film is held within a capillary or between microscope slides. Passing the material film through a thermal gradient, *G*, at a sufficiently low and constant velocity, *v*, which defines the freezing front velocity, steady state conditions can be maintained, and the applied cooling rate can be calculated as,

$$\dot{C} = Gv. \qquad \text{Eq 2}$$

With such a set-up, correlations can be determined, for example, between freezing front velocity and lamellar spacing, λ, and crystal growth morphologies and instability **[G]** formation, all of which are characteristic ice-templating and structure formation parameters and phenomena.

When choosing a material film thickness for such experiments, a compromise needs to be struck between convection, which increases with increasing film thickness, and surface tension effects at the capillary or Hele-Shaw cell wall, which increase with decreasing film thickness. Typically, sample thicknesses are kept at about 100 µm. Applying typical freezing front velocities at this film thickness, the primary spacing of the growing dendrites is comparable to the film thickness, and the sample containing walls act as no flux planes.[102,103]

Traditionally, 2D crystal growth studies have been performed in situ in an optical microscope, limiting such experiments to either transparent solutions or slurries with low particle loading.[94,100] Recently, confocal microscopy has been shown to offer a powerful expansion of this optical technique to samples, which can be imaged through-thickness, offering to obtain additional information, because a third dimension can be added to the otherwise optically obtained projections **[G]**, and because different components of a material system can be stained, and thus better distinguished from one another, for a more detailed analysis also of slurries with low particle concentrations.[97]

Nevertheless, despite considerable improvements to 2D analysis capabilities, a key disadvantage of dynamic experiments in 2D in optical systems remains, namely that observations are limited to thin and transparent material systems which, due to spatial sample confinements, behave differentially to true 3D systems, so that sample behaviour cannot readily be extrapolated into true 3D bulk material performance.

[H3] X-ray radioscopy

Thanks to the high penetration depth and short wavelength of X-rays, it is possible to expand 2D dynamic imaging and analysis further to optically opaque and thicker materials, by performing high-resolution *in situ* X-ray radioscopy[42,43] (Figure 4Ca–c). X-ray radioscopy produces 2D radiographs of the X-ray absorption distribution of a material integrated along the beam direction.

For components with similar X-ray absorption coefficients, phase contrast can be exploited to distinguish different constituents of similar absorption.[104] To reveal the internal structural evolution of matter, e.g. during structure formation or evolution, X-ray radioscopy can be applied, typically with a high temporal resolution in the range of several images per second up to Megahertz acquisition rates for extremely fast processes.[105,106]

Radioscopy thus permits to investigate and quantify directional solidification behaviour. For example, the 2D shape and propagation kinetic of the solid/liquid interface in solutions and slurries can be measured. In slurries with sufficiently small particles, also information on

particle freezing front interactions as well as particle redistributions in the particle-enriched phase can be obtained. Similarly, particle self-assembly and particle packing in the interdendritic spaces can be evaluated, which is of interest, because form the cell walls of the and determine the properties of the freeze-cast cellular solid after lyophilization.[42,43,107,108]

However, the advantages that radioscopy offers over optical and confocal microscopy come at the cost of a higher energy entry and absorption, which may affect both solidification and self-assembly processes. Additionally, in situ imaging by radioscopy shares the shortcomings of other 2D techniques that a quantitative extrapolation of phenomena from 2D to 3D structure formation cannot be made. Necessary for a reliable quantification of crystal growth and structure formation phenomena is a 3D in situ technique, which in the form of X-ray tomoscopy has recently become available[34] (Figure 3).

[H3] X-ray tomoscopy

X-ray tomoscopy is the dynamic form of X-ray tomography.[36] X-ray tomography is based on the recording of a certain number of 2D X-ray micro- or radiographs, so called projections, taken at regularly spaced angles over a 180° or 360° sample rotation, in parallel or divergent beam geometries, respectively. Using dark-field and flat-field images, with the latter taken without the sample present, and without and with X-ray illumination, respectively, the radiographs of the 2D projections are first darkfield and flatfield corrected to remove detector artifacts, such as detector errors, dark currents, or uneven illumination.

Traditionally exploited in X-ray imaging applications is absorption contrast (Figure 3c), when both X-ray absorption and differences in X-ray absorption coefficients, which scale with atomic number, are sufficiently large to distinguish one component or phase from another (Figure 3c).[38,39] Phase contrast **[G]** is used for materials with low X-ray attenuation coefficients **[G]** and small differences in atomic number and electron density, such as water, ice, and polymers (Figure 3b). Phase contrast offers the added benefit that it enhances interfaces between constituents and thereby increases the contrast and clarity of fine features (Figure 3c).[38] Synchrotron X-rays offer to select and balance absorption and phase contrast, so that all classes of materials can be imaged by tomoscopy both in their liquid (solutions, particle suspensions, melts) and their solid form. To extract phase-contrast only information, the radiographs are filtered with a single-distance propagation-based phase contrast algorithm, before they are reconstructed into a 3D sample volume.[109–111]

X-ray tomography is a well-stablished, high-resolution method for the non-destructive characterization of materials of all classes.[39] The digital twin of the sample is ideally suited not only for a qualitative analysis of a sample by virtually dissecting it, but also for truly quantitative analyses to determine, for example, the volume fractions of different phases or the amount and topology of a sample's porosity. Such 3D analyses of usually large data tomograms are computationally intensive. They are typically performed on workstations with either open-source or commercial 3D visualization and data analysis tools and techniques. Examples for such tools are ImageJ[112], usually with many bundled plugins such as Fiji[113], Dragonfly [114], or Avizo [115]; into these, the image stacks can be loaded for user-friendly viewing and data analysis in both the spatial and time domain.

X-ray tomoscopy employs ever increasing acquisition speeds to image and resolve with both high spatial and high temporal resolution, highly dynamic in situ and operando structural changes.[36] Because of its requirement of high flux and ideally both absorption and phase-contrast. X-ray tomoscopy is currently primarily been performed at synchrotrons.[35,36,44].

Figures 3a-b shows a schematic of the tomoscopy setup used for the analysis of ice-crystal growth and templating during freeze casting. For imaging, a custom-designed copper coldfinger is mounted onto a custom-designed fast rotation stage detailed previously.[36] The sample solution or slurry is filled with a syringe into a Kapton tube mounted on the coldfinger with a second Kapton tube acting as thermally insulating container and protection against airflow (Figure 3b). To directionally solidify the sample under well-defined conditions, the coldfinger temperature is controlled by a nitrogen cryogenic jet with a defined temperature. The specifics of the temperature gradient, G, the freezing front velocity, v, and the global and local

cooling rates, $\dot{C}$ and $\dot{C}_{\mathrm{loc}}$, respectively, are determined with a custom-designed thermocouple mould (Figure 3b).

Typical freezing front velocities of 1–50 µm/s can easily be achieved in tomoscopy experiments performed to quantify the dynamic processes of crystal growth and structure formation; at these freezing front velocities, feature sizes typically fall within the range of 5–200 µm and thus within the limits of resolution. The sample diameter depends on the material system studied, not only because of considerations of X-ray absorption and transmission, feature sizes and their numbers for statistical reasons, but because the sample rotates at high speed during imaging, thereby generating and experiencing centripetal forces which can compromise sample homogeneity. While high quality results have been obtained with samples of 2–4 mm diameter, resolving features with an effective spatial resolution of a few microns at 1–100 tps [36], larger diameters are possible and smaller diameters might be required. Overall, a good compromise needs to be found between the field of view **[G]** and the desired spatial and temporal resolutions by adjusting the rotation speed, the exposure time per projection, the number of projections, and the duration of the experiment; the compromise depends on the scientific questions to be answered.

Finally, an appropriate X-ray energy, flux and sample-detector distance need to be selected, also in the light of the above parameters, to achieve optimal absorption and/or phase-contrast of the sample while at the sample avoiding delays in solidification, radiation damage or centripetal forces that could affect the experimental results. Section 6.2 and Box 2 provide more detailed considerations of these effects. The X-ray radiography data acquired by X-ray cameras or detectors are typically stored and processed in 8-, 16- or 32-bit containers, depending on the bit depth of the detector (typically more than 12 bit) and the byte-based storage architecture. These image files are typically either ".raw"-files, which contain a matrix of intensities, or ".tif"-files (TIFF = Tagged Image File Format), which store in their header additional information (metadata) about the acquisition process. Similarly, the reconstructed 3D data of the tomogram **[G]**, can consist of a ".tif"-file image stack, or a ".raw"-volume. The disadvantage of its 32-bit register is that the maximum size of classic TIFF files is 4 GB. This problem of storing large numerical data together with its metadata is overcome by the increasingly popular HDF5-file (Hierarchical Data) format; HDF5 allows multidimensional data to be organised and read efficiently (for example, also only in parts). However, further efforts are needed to develop a universal file format that is interchangeable among different imaging facilities. The 3D data set, which can be visualized and analysed, is reconstructed from the image corrected 2D radiographs by mathematically backprojecting the 2D data to form the 3D data volume termed "tomogram" using algorithms such as, for example, gridrec. [116]

[H3] Radioscopy and tomoscopy data analysis

With the best possible data quality obtained thanks to experimental and data processing optimization, the 3D tomograms can be segmented, which means the different components or phases of the sample can be virtually separated based on their X-ray attenuation or phase shift generated contrast. The simplest form of segmentation is based on greyscale **[G]** threshold values. However, since the same grey values are often found in different phases, approaches based on local conditions or region growing are often advantageous. Other powerful segmentation methods are based on supervised machine learning, in which each pixel is first classified subjectively marking the pixels by hand followed by a prediction provided by the algorithm based on a number of filters and local measures (e.g. by using a random forest approach). An improvement in the quality of results can be achieved by iteratively applying the procedure [117,118].

Many convolutional neural network (CNN)-based approaches to segmentation, based on manually segmented training data, have evolved in recent years, of which one of the most popular and most widely used is probably the U-net architecture[119]. Limitations in resolution or contrast can cause neighbouring but separate regions to touch, leading to erroneous

measurements when analysing individual object features. To overcome this, the well-established watershed transformation is used to separate the individual objects from each other, but machine learning approaches similar to those already mentioned can also be used for image segmentation[120]. To improve the often still noisy, binarized images, morphological filters can be used, which, for example, allow regions to be removed or connected by means of erosion and dilation operators. Complementing the cited commercial software, many useful, fast and user-friendly open-source tools exist for such pipelines.[121–124]

In addition to global process parameter, such as the freezing front velocity for the entire sample volume (Figure 5A–B), also more site-specific information can be extracted from the data sets. Examples are volume fractions of individual phases in a volume of interest, or the number of crystals or pores (also divided into open and closed porosity[125]). It is also possible to measure features locally and even individually, such as the local thickness of lamellae (Figure 3d, Figure 5C–D) or the orientation and angular incline with respect to the mould axis of the lamellar cell walls of freeze cast materials [126] (Figure 5D). Particularly valuable is that also the evolution of such features can be quantified, in the case of freeze cast materials at the local level, for example, to evaluate and compare the evolution of domains (Figure 5A) or analyse also individual features, such as instability formation and structure templating on individual lamellae (Figures 5D–E).

Similarly, the evolution of particle interactions, orientation and self-assembly into the final cell wall structure can be observed [127] (Figures Fa–d) to compare the behaviour of different particle sizes and geometries, such as equiaxed with plate- or flake-like particles [8] (Figure Ga-d) also as a reflection of interdendritic flows and externally applied fields in combination with crystal growth phenomena such as instability formation. For this purpose, the directional statistics of the images or segmented objects can be evaluated. This can be done, for example, by computing the local structure tensors, which describe the grey level gradients of their neighbourhood, or by a principal component analysis **[G]** of the voxels **[G]** belonging to each object, which define the directions of largest variations and therefore the orientation and shape of the individual objects.[121,123,128].

[H2] Post Mortem Characterization Techniques

Structure-property-processing correlations are required to tailor material structure and properties for optimal performance in a given application. Lacking the fundamental science for material systems more complex than binary solutions.[21], such correlations are difficult to impossible to formulate from first principle. Particularly complex are slurry-based systems for the manufacture of freeze-cast ceramics and metals, because these typically contain not only a solvent and particles, but also solutes such as dispersants and binders. We therefore still rely predominantly on the results of empirical studies, on the basis of which structure-property-processing correlations can be formulated.

Because the hierarchical architecture of freeze-cast materials encompasses length scales from a few nanometers for individual components to several centimeters for the entire sample, a careful material characterization is required of each of the three main levels of the hierarchy. Based on the results obtained, it is then possible to arrive at robust, empirical structure-property-processing correlations for the custom-design of new and improved materials.

At the 1st level of the hierarchy, we focus on the pore morphology of the freeze-cast material, which determines whether a foam-like bending or a honeycomb-like stretch dominated mechanical performance is to be expected, and how strong the property anisotropy **[G]** of the cellular solid is[129,130]. At the 2nd level of the hierarchy, we focus on the cell wall material structure, which determines the cell wall sold properties, that define the mechanical and physical properties. And at the 3rd level of the hierarchy, we analyse the cell wall surface features which add additional functionality to freeze-cast materials (see Figure S1). At this level also polymer and particle structure and morphology, for example, whether it is crystalline or amorphous, or porous, such as activated carbon, or lamellar as in the case of clay and MXenes, and and their effect on materials performance, is of great interest.

[H1] Applications

Due to their honeycomb-like structure, which is characterized by a highly aligned porosity, freeze cast materials usually exhibit a structural anisotropy **[G]** and an associated property anisotropy with superior mechanical[1,7,31], electrical[18], magnetic[75], flow and other properties[26,61,73,82,131–133] parallel to the freezing direction and honeycomb's long pore axis.

The anisotropy of freeze-cast materials distinguishes them from others and results in an efficiency in material performance, which we illustrate here using the Gibson-Ashby scaling laws and their graphic presentations for mechanical properties of cellular materials.[130]. Two types of cellular solids are compared: foams, in which the pores are more or less equiaxed, and honeycombs, in which the pores are unidirectional and aligned (Figure S6A-B).

Three properties dominate the mechanical performance of foams and honeycombs: the solid from which the foam is made, the pore topology and connectivity, and the relative density of the cellular solid, which is the density of the foam, ρ^*, divided by the density of the solid, ρ_s, from which it is made and defines the materials overall porosity as $P = 1 - \frac{\rho^*}{\rho_s}$. Taking modulus and strength of foams and honeycombs as examples, we find that both properties decrease linearly as a function of relative density in the case of honeycombs:

$$E \propto E_s \left(\frac{\rho^*}{\rho_s}\right)^1 \text{ and } \sigma \propto \sigma_s \left(\frac{\rho^*}{\rho_s}\right)^1 \qquad \text{Eq 3}$$

while they decrease to the power of 2 and 1.5 with relative density, respectively, in the case of foams:

$$E \propto E_s \left(\frac{\rho^*}{\rho_s}\right)^2 \text{ and } \sigma \propto \sigma_s \left(\frac{\rho^*}{\rho_s}\right)^{1.5} \qquad \text{Eq 4}$$

(Figure S6A-B, [129]). This means that a honeycomb with a relative density of 2% thus an overall porosity of 98% (which is typical for freeze-cast polymer scaffolds) is parallel to the pore alignment about 100 times stiffer and about 10 times stronger than than a foam of the same density, thus 100 and 10 times more efficient, respectively, when efficiency is measured as function per unit weight.

Because not only the relative density but also the solid that forms the cell walls and cell-wall alignment and organization of the freeze-cast sample determines its material properties, these can be further enhanced through appropriate material selection, a structural optimization of the cell wall material, and the custom design of the domain structure. For example, when also the cell wall materials exhibit a preferential structural alignment due to the directional solidification, and an externally applied field, for example (Figure 6). Plotting the modulus of freeze cast alumina ceramics freeze cast from spherical and platelet-like particles and magnetic Sendust flakes freeze cast in the absence and the presence of an externally applied field versus their respective relative densities, illustrates how significant structural optimization is for improved material performance (Figure S6D-F,[75]).

The combination of anisotropic structure and properties, and typically considerably higher property values parallel to the freezing directions, make freeze cast materials promising for a wide range of uses. Of these, we highlight biomedical and energy-related applications here. A few examples for the many other possible applications of freeze-cast materials [134]are membranes for filtration and separation, catalysts, and sensors[135] mechanical energy absorption,[6] thermal insulation,[26] acoustical absorption,[136] electromagnetic shielding, [87,137] supercapacitors,[138] solar absorbers[139], and piezoresistive pressure sensors.[140] Many of these applications are enabled by the use or addition of solid, porous, or layered materials, such as such as graphene, reduced graphene oxide (rGO), clay and 2D metal carbides and nitrides

(MXenes), which offer particular geometries (e.g. whiskers, fibrils, fibers, flakes or platelets) mechanical and physical (electric, piezoelectric, magnetic, optical) properties.

[H2] Biomedical Applications

While first reports explored the directional solidification of sludge as a route of energy efficient waste disposal[48,141,142], biomedical applications quickly emerged as a particularly promising field for the use of freeze-cast materials, such as collagen, chitosan, and nanocellulose, and hydroxyapatite and tri-calcium phosphate for both soft and hard tissue regeneration, respectively.

For soft-tissue regeneration, both "smooth" and "fibrillar" polymers have been explored in fundamental and applied studies to investigate structure-property-processing correlations. These were primarily performed with agar[142], collagen,[28,29,143–147] chitosan[33], alginate[18], and nanocellulose,[148] and their composites[6,31]. Significantly fewer studies have been performed to determine the biocompatibility of freeze-cast polymer scaffolds in vitro[61,149–154] and in vivo[152,155–160]. Fewer studies, still, have been performed to evaluate in vivo their functional promise for specific application, such as nerve regeneration,[155,160] permanent female sterilization,[158,161] ureteral stents,[32] and skin grafts.[162] Increasingly, important effects of composition, pore size, and regenerative efficacy have been observed, also taking advantage of new tools for the analysis of gene expression in response to an implant.[156,157] One company is currently commercializing freeze-cast materials for biomedical applications.

For hard-tissue regeneration, primarily hydroxyapatite, tri-calcium phosphate and their composite scaffolds have been studied, also here first to determine structure-property-processing correlations,[49,163–167] then to test scaffolds in vitro [149] and in vivo.[159] Because toughness is not only of particular importance in hard tissue substitutes, for bone for example, but also generally in technical ceramics, freeze casting was quickly applied to the manufacture of artificial nacre, a 95% ceramic 5% polymer composite[168], with the intent to simultaneously achieve high strength and toughness, which is of great commercial value.[8,53,169–171] Attempting to emulate nacre, a range of freeze-cast composites resulted, both made from ceramics and metals, not only with a polymer glue phase within the cell wall, but also in the form of a porous freeze cast material infiltrated with a polymer phase, for example[14,170,172].

Overall, freeze cast scaffolds possess attractive structural [61,171] and mechanical properties [4,7,28,29,33] in combinations that "mimic" structure and performance of many natural tissues[171,173], making them promising in tissue regeneration. Freeze cast polymeric scaffolds can serve, many different functions, for example, as a nerve conduit tube or "shell" with radial porosity that protects the "core" whose honeycomb-like aligned porosity guides neurite growth and regeneration, also with the addition of growth factors or viral vectors [71,152,155,160,174,174–176]. In the case of bone substitution, freeze cast ceramic-polymer hybrid scaffolds provide both the mechanical and the structural support and guidance features to facilitate bone regeneration [49,126,159,164]. Similarly, structural, mechanical, and chemical cues of freeze-cast materials can be custom-designed for cartilage regrowth[92,177], cardiac tissue engineering[178], wound healing[149,162,179], and permanent female sterilization[158]. Radially freeze cast, tubular scaffolds can be used as soft ureteral stents[32] due to the resilience and high permeability offered by the hierarchical pore architecture **[G]**.

[H2] Energy Applications

[H3] Energy generation

Porous materials are highly attractive also for energy applications. In the case of energy generation, freeze-cast ceramic and metal matrices infiltrated with nucleotide-rich material have been considered as an advanced fuel form designed to reduce the amount of long-lived radioactive isotopes that need to be disposed of as waste.[180] The rational being a well-defined

placement of the fuel into the host matrix for higher burn up, higher power, and greater margins to fuel melting then yet achieved.[180] Ceramic-based electrodes for fuel cell[83,87] have also been created by freeze casting.

[H3] Energy storage

The highly aligned porosities created by freeze casting and other freeze casting-based continuous methods in electrodes provide low tortuosity pathways for mass and charge transport as well as increased access to active material (Figures 6Da–Db). Carbon-based electrodes for batteries[181–185] and super capacitors[186,187] possess promising properties, as do ceramic-based electrodes for iron-air batteries.[188] Other well performing freeze-cast components include sulfur electrodes[85] and lithium salt electrodes[132,189–193] for lithium ion batteries. Thermal energy storage is being explored with freeze-cast phase-change materials. [194]

[H3] Power conversion

Freeze-Cast magnetic composites with a nacre-like brick-and-mortar structure composed of magnetic flakes that are separated by an insulating film and are magnetically aligned to form a monodomain structure have shown promise as magnetic cores for high frequency power conversion applications (Figures 6Aa–Cd). The particle geometry and their alignment in the composite result in considerably reduced Eddie current losses in an alternating magnetic field; and the composite possesses high quality factors in at least two directions [75]

[H1] Reproducibility and Data Deposition

[H2] Freeze Casting

Reproducibility of results is assured, when all experimental details for sample preparation from the composition of the solution or slurry to the specific sample processing condition, including the mould design, type of cooling system and set-up used, and applied cooling rates, $\dot{C}$, are reported. Particular attention needs to be paid to the homogeneity and stability of the slurry, adjusting viscosity and adding dispersants, also taking the duration of sample processing into account, where necessary, and mixing slurries once more directly before freeze casting, because of sedimentation both before and during the freeze casting process. Parameters can be adjusted, depending on desired outcomes, i.e., whether sample homogeneity or property gradients are desired.

Similarly important are the lyophilization or solvent exchange system and conditions used, and sample preparation procedures for material characterization. Many freeze casting systems and moulds result, for example, in local cooling rate, $\dot{C}_{\mathrm{loc}}$, variations along the length of the mould, which are reflected in a sample's structure and properties in structure. It is, therefore, important to report also the exact sample location for which structure and properties are measured, for example by stating the height of the sample centre from the mould bottom, and the distance of the sample centre to the mould wall (Figure 7).

A procedure for a high reproducibility of results is illustrated taking the most common freeze-casting set-up as an example, namely the one-sided mould design of Figure 2a. In a mould and set-up like this, changes in the local cooling rates as well as sedimentation effects are reflected in structural, physical and mechanical property variations along the length of the mould. After lyophilization, each sample cylinder is fixed with its bottom on a ceramic plate for cutting into predetermined shapes and sizes, according to the scheme illustrated in Figure 7, for structural and mechanical characterisation using, for example a diamond wire saw with a

220 μm diameter diamond-decorated steel wire at a wire speed of 0.7 ms^{-1} on a Well 4240 saw (WELL Diamond Wire Saws, Inc., Norcross, GA).

For structural, mechanical, electrical, thermal, and magnetic characterisation, cubes with a side length of 4 mm or 5 mm are cut at three standard heights, measured from the bottom of the sample with cube centres at 7 mm, 17.5 mm and 28 mm, respectively. From each of the three sample cylinders, four or five cubes are cut, marking cube position and orientation within the sample, and tested assorted by sample height to determine the density. For mechanical characterization, two cubes are tested parallel and two perpendicular to the freezing directions to determine their respective properties, and mechanical anisotropy **[G]** and performance (Figure 7). With this testing procedure, it is possible to quantify sedimentation and component packing effects in the freeze-cast scaffolds, as a function of particle shape, size, size distribution, and particle loading, slurry composition and viscosity, and applied cooling rate, for example, and also their effect on sample shrinkage in the case of samples that are sintered after lyophilization.

For mechanical testing, frequently, cubes of 5 mm side length are chosen for several reasons: to maximize the volume of material tested while at the same time avoiding size and edge effects that are associated with mechanical testing of porous materials [195,196], and to minimize shear, which may be enhanced due to cell wall misalignments with the loading direction, and structural gradient effects along the height of freeze-cast samples. The standard for mechanical testing requires an ideal aspect ratio of ~2 for compression testing, [197] because non-uniform sample stresses, such as stress-concentrations at corners, can occur in samples with a lower aspect ratio, like cubes. An additional concern in low aspect ratio samples is an increased sample sensitivity to frictional effects, because of lateral compressive forces and regions of reduced strain[14]. While friction during testing can be minimized by placing Teflon tape between sample and plates, the fact that cubic samples result in higher strength values needs to be borne in mind when comparisons are made with results obtained with samples of higher aspect ratios (≥2). Typical strain rates used for compression testing are $\dot{\varepsilon} = 10^{-2}/\mathrm{s}$; depending on the material, strain hardening should be taken into consideration.

The modulus of freeze-cast materials is the slope of a linear fit to the initially linear stress-strain curve. The toughness is frequently reported as the area underneath the stress–strain curve from 0% to 60% strain. Finally, the yield strength of freeze-cast polymeric and ceramic freeze-cast materials is determined as the intersection of the tangents to the elastic and the plateau or collapse of the stress strain curve; in the case of metals, the 0.2% strain offset method is frequently applied [14]. The mechanical properties of the thin cell walls in the freeze cast samples, especially those with biopolymers[198], are significantly affected by the moisture content. It is, therefore, necessary to report the relative humidity of the acclimatization and testing environments as well as the hydration state of the sample[28,29,31,199].

The most comprehensive data repository currently available for freeze-cast materials of all classes is FreezeCast.net,[4] in which the reader finds collated more than 800 experimental results covering different solvent systems, compositions, and freezing conditions. This repository provides highly valuable information for comparison with new results, and also complement one's own results with literature values, aiding to establishment structure-property-processing correlations[200]. While ideally such correlations are best established on results obtained using identical experimental conditions, thus the same freeze casting set-up and sample processing conditions, this if often not possible.

Finally, an easily accessible visualization of freeze-cast material properties for an objective material evaluation, comparison, and selection are material property charts combined with material indices [28–31,33,201]. The log-log representation makes it easy to compare freeze cast materials of different compositions and classes prepared under different processing conditions, to discover clusters of similarities, and to spot white areas for further exploration; they reveal also possible structure-property-processing correlation. Several software package are available to create such charts [202,203].

[H2] X-ray Tomoscopy

X-ray tomography and tomoscopy allow a variety of qualitative and quantitative statements to be made about the samples, whereby the accuracy of the results always depends on the image quality of the reconstructed volumes and the method of quantification. The most important step is the segmentation of the components. In addition, complementary calibration methods, e.g., for sample density, can be performed to adjust the parameters for proper segmentation. Further decisive steps are feature reconcilement and feature tracking. For all these steps artificial intelligence plays already an important role and is expected to play a much more decisive role in the future, in distinguishing the features of interest beyond simple binarization or segmentation algorithms.

In order to be able to reproduce the results obtained with different X-ray scanners, a detailed record of the imaging parameters is required. These parameters are: the beam energy, the filters used, the type of scintillator, optic or detector, the amount of phase contrast, the pixel size (or better the measured spatial resolution), the field of view, the exposure time per projection, the number of projections per tomogram, the total experimental time and the acquisition rate in tomograms per second. These parameters correspond, more or less, to the parameters listed in Box 2. Unfortunately, many of these relevant parameters are often omitted in the literature, making it impossible to reproduce and verify some measurements.

Several databases [204,205] with published results are available on the internet or in repositories where original series of tomograms can be downloaded and analysed with own methods or parameters [206].

[H1] Limitations and Optimisations

[H2] Freeze Casting

A number of challenges and limitations of the freeze casting process exist. Aqueous materials systems tend to be safe and environmentally benign, but also limit the chemistries of components to those that are either water soluble or compatible with water. Particle sizes and solvents and their properties must be chosen and adapted for a given solvent/binder/dispersant system to assure that the slurry viscosity is sufficiently high to minimize sedimentation and keep it within an acceptable range for the duration of sample processing. This poses an upper limit as to how large a particle may be at a given material density. However, particle sizes may also not become too small when the particle material is comparatively reactive (e.g. titanium, tantalum). Alternative solvents can sometimes offer a solution, here, when the associated change (due to a different crystal growth morphology) in sample architecture is acceptable.

Undesired smaller and larger bubbles in solutions and slurries, which when micronized often are due to oxygen dissolved in the water, are best reduced when the water is outgassed before sample mixing and the sample is once more outgassed after mixing, and the moulds are filled holding the injecting system underneath the sample surface. When additional porosities are desired, deliberate pre-foaming the sample is a tested method.[207]

Freeze casting in batches, using either moulds for multiple samples or using systems with multiple cold-fingers, offers advantages and disadvantages. Advantages are that a greater versatility of sizes and possibly also more complex shapes and thermal gradients, thus material architectures, can be manufactures while it also eases the processing of multiple identically sized and shaped samples at a given set of conditions. Continuous freeze casting methods, overcome the production volume disadvantage of batch processing at the cost of shape versatility. At the same time, complex shapes can be cut or stamped out from freeze-cast sheets or volumes, and additional structural and property gradients can be introduced through 3D freeze printing.

Many freeze casting systems still used liquid nitrogen or its chilled off-gas as the cooling source. Alternative cooling sources, such as dry ice and Peltier-cooled plates are alternatives, also in combination with chillers which support these or cool systems using solvents with higher phase transition temperatures. Cost, energy, and material waste and efficiency considerations tend and will drive these innovations in processing technology forward; also from the perspective of sustainability, such improvements are necessary and welcome.

Often a little neglected are considerations with respect to coldfinger surface corrosion and sample mould material reactions. For example, keeping both copper coldfinger and copper mould bottom flat, highly polished and corrosion free at all times, by using a regular surface cleaning with a salt in vinegar solution, for example, insures best possible thermal contact between the two. Similarly, covering the copper mould bottom surface with a thin polymer film, prevents direct integrations of the solution or slurry with the copper and helps to preserves a clean copper surface for thermal transport with minimal losses through the polymer, while preventing the sample solution or slurry reactions with it. Acetic acid, frequently used to dissolve collagen and chitosan, can otherwise react with, for example, oxides formed on the copper mould bottom and cause undesirable sample contamination.

[H2] X-ray Tomoscopy

Although much progress has been made in the development of X-ray tomography and tomoscopy, several physical and technical limitations remain to be overcome. For example, strongly X-ray absorbing materials, i.e. materials with a high X-ray absorption coefficient, μ, such as gold, lead or even titanium, and very dense and thick objects are still very difficult to image. One challenge is to obtain sufficient contrast. Contrast is required to distinguish between different components and to characterize structural features. The contrast of the images obtained depends on the interaction of X-rays with matter. Absorption contrast results from the different attenuation coefficients (μ) and thickness (d) of the constituents, which obeys Beer-Lambert´s attenuation law, which describes the intensity drop between the initial beam intensity (I_0), and the transmitted intensities (I):

$$I = I_0\, e^{-\mu d} \qquad \text{Eq 3}$$

Phase contrast is caused by the phase difference of the beam as it passes though different constituents delimited by a boundary. To achieve a desirable contrast, the beam energy and flux must be adjusted to the materials and thickness of the sample. For tomoscopy, mostly white (full spectrum) or pink (reduced spectrum) beam with high flux, instead of a monochromatic beam with lower flux, are used, as the transmitted intensities need to be high to allow fast acquisition.

When applying X-ray tomoscopy, sample damage can occur. Tomoscopy requires a high X-ray flux and high sample rotation speeds. Both can have a detrimental effect on the sample integrity. The former is especially critical for polymeric or temperature-sensitive samples, the latter can affect sample shape or distribution of constituents due to high centrifugal forces leading to a radial acceleration (a) which depends on the rotation frequency (f) and on the sample diameter ($\emptyset$) according to[37]:

$$a = 2\emptyset\pi^2 f^2. \qquad \text{Eq 4}$$

[H1] Outlook

[H2] Applications of Freeze-cast Materials

While, initially, the freeze casting process was primarily developed for cell and tissue preservation, soon its potential for soft (e.g., nerve, skin)[152,155,162,174] and hard (e.g., bone)[49,126,159,164,208]tissue repair and regeneration was discovered, because freeze-cast materials possess architectures well suited to support healing processes and integrate well into host

tissues. Since then, freeze-cast materials for these applications have been refined through functionalization with growth factors and viral vectors, and numerous non-medical applications have emerged. These applications include materials for energy generation and storage, from safer nuclear fuels to battery and supercapacitor electrodes, similarly materials for filters and catalytic converters, sorbents, and thermally conducting or insulating materials, thermoelectric materials, and electromagnetic shielding materials.

[H2] The Freeze-casting Method

Freeze casting or, more generally, solvent casting has over the past three to four decades been advanced considerably as a manufacturing technique. In parallel, also the fundamental science of directional solidification of solutions and slurries, primarily of aqueous systems, has matured. A large number of exploratory and systematic empirical studies with all classes of materials have been performed to determine robust structure-property-processing correlations. Similarly, the dynamics of ice crystal growth and ice-templating processes have become better understood because of advances in experiments combined with phase-field simulations. For the custom-design of materials, we are still lacking predictive models which, in addition to diffusional effects, take into account also those due to thermo-solutial convection, sedimentation, and forces that are generated by the volumetric expansion of water during the liquid-solid phase transition, forces caused by interdendritic extensional shear flow **[G]** , as well as mechanical and other forces due to mould shrinkage and externally applied forces, be they magnetic, electric, or acoustic.

Experiments in microgravity on the International Space Station are planned to help advance the field by reducing, in the first instance, sedimentation and thermo-solutial effects. Phase-field and other simulation techniques will need to be expanded or combined to include also flow and internally and externally applied forces. Also the dynamics of particle interactions with one another and the freezing front, and component and additive interactions with the ice phase deserve further attention to shed more light on structure formation, structural organization, and cell-wall self-assembly processes, in addition to those already mentioned above, and their respective effects on the properties of freeze-cast materials.

In contrast to the non-faceted transparent model material systems that form cubic crystals, such as camphene-naphthalene and succinonitrile-camphor traditionally used in directional solidification studies on Earth and in Space, water exhibits hexagonal, partially faceted crystal growth **[G]** , which until recently had been comparatively little studied. The most recent additions to the portfolio are solvents with fully faceted crystal growth **[G]**. The goal for their use is two-fold: to further expand hierarchical pore and material architectures and to advance our study of crystal growth dynamics aiming to complete our fundamental understanding of the different crystal growth phenomena.

Other physical and chemical processes, such as self-assembly[148], crosslinking even when the ice is still present[209–211], and salting out[131], either caused by the freezing process or externally induced, can further improve the resulting properties, and simplify the post processing requirements to stabilize the freeze cast materials. The fundamental mechanism of the processes has, to date, been little studied both experimentally and in simulations due to the complicated multiphysical processes. However, the versatility of these additionally introduced processes to hybrid and composite materials systems merits further investigation.

Also the design and construction of new freeze-casting systems continues, with increasing research attention applied to continuous freeze casting, freeze spraying, freeze-spinning, freeze printing, and freeze extrusion processes and also the freezing of thinner or thicker films with a range of pore morphologies and orientations. Upscaling production of these materials is eased by the fact that both freezing and lyophilization processes are standard in the food industry, both in the form of batch and continuous processing lines. This means that it is more a question of process adaptation than invention to accommodate new solution and slurry chemistries, sample and component geometries, and batch sizes.

Finally, there is room for improvement concerning sample quality and quality control. Desirable are standards, on which the community agrees, to enable easier comparisons of results obtained with different material systems, in different studies and labs, in addition to best possible lab-independent uniformity, consistency. Greater attention will also need to be paid to environmental impact assessments and minimization of both the freeze-casting process itself and the materials made with it. Needed are systematic eco-audits of the processes and materials systems used, to determine, for example, pros and contras of the different cooling systems, to quantify process and material efficiencies, to enable an object comparison and selection of solvents, also from this perspective, to determine potentials for waste reduction, and to enable also an objective comparison of the freeze casting with other manufacturing processes and the materials made with it.

References

1. Deville, S., Saiz, E., Nalla, R. K. & Tomsia, A. P. Freezing as a Path to Build Complex Composites. *Science* **311**, 515–518 (2006).
2. Donius, A. E. *et al.* Cryogenic EBSD reveals structure of directionally solidified ice–polymer composite. *Mater. Charact.* **93**, 184–190 (2014).
3. Schoof, H., Bruns, L., Fischer, A., Heschel, I. & Rau, G. Dendritic ice morphology in unidirectionally solidified collagen suspensions. *J. Cryst. Growth* **209**, 122–129 (2000).
4. Scotti, K. L. & Dunand, D. C. Freeze casting – A review of processing, microstructure and properties via the open data repository, FreezeCasting.net. *Prog. Mater. Sci.* **94**, 243–305 (2018).
5. Wegst, U. G. K., Schecter, M., Donius, A. E. & Hunger, P. M. Biomaterials by freeze casting. *Philos. Trans. R. Soc. Math. Phys. Eng. Sci.* **368**, 2099–2121 (2010).
6. Donius, A. E., Liu, A., Berglund, L. A. & Wegst, U. G. K. Superior mechanical performance of highly porous, anisotropic nanocellulose–montmorillonite aerogels prepared by freeze casting. *J. Mech. Behav. Biomed. Mater.* **37**, 88–99 (2014).
7. Hunger, P. M., Donius, A. E. & Wegst, U. G. K. Structure–property-processing correlations in freeze-cast composite scaffolds. *Acta Biomater.* **9**, 6338–6348 (2013).
8. Hunger, P. M., Donius, A. E. & Wegst, U. G. K. Platelets self-assemble into porous nacre during freeze casting. *J. Mech. Behav. Biomed. Mater.* **19**, 87–93 (2013).
9. Araki, K. & Halloran, J. W. Room-Temperature Freeze Casting for Ceramics with Nonaqueous Sublimable Vehicles in the Naphthalene–Camphor Eutectic System. *J. Am. Ceram. Soc.* **87**, 2014–2019 (2004).
10. Cheng, Q., Huang, C. & Tomsia, A. P. Freeze Casting for Assembling Bioinspired Structural Materials. *Adv. Mater.* **29**, 1703155 (2017).

11. Chino, Y. & Dunand, D. C. Directionally freeze-cast titanium foam with aligned, elongated pores. *Acta Mater.* **56**, 105–113 (2008).
12. Fukasawa, T., Deng, Z.-Y., Ando, M., Ohji, T. & Kanzaki, S. Synthesis of Porous Silicon Nitride with Unidirectionally Aligned Channels Using Freeze-Drying Process. *J. Am. Ceram. Soc.* **85**, 2151–2155 (2002).
13. Porter, M. M. *et al.* Magnetic freeze casting inspired by nature. *Mater. Sci. Eng. A* **556**, 741–750 (2012).
14. Weaver, J. S., Kalidindi, S. R. & Wegst, U. G. K. Structure-processing correlations and mechanical properties in freeze-cast Ti-6Al-4V with highly aligned porosity and a lightweight Ti-6Al-4V-PMMA composite with excellent energy absorption capability. *Acta Mater.* **132**, 182–192 (2017).
15. Wilke, S. K., Mack, J. B., Kenel, C. & Dunand, D. C. Evolution of directionally freeze-cast Fe2O3 and Fe2O3+NiO green bodies during reduction and sintering to create lamellar Fe and Fe-20Ni foams. *J. Alloys Compd.* **889**, 161707 (2021).
16. Kádár, C. *et al.* Investigation of the Compressive Behavior of a Freeze-Cast Cu Foam Using Acoustic Emission Measurement. *Adv. Eng. Mater.* **24**, 2100378 (2022).
17. Picot, O. T. *et al.* Using graphene networks to build bioinspired self-monitoring ceramics. *Nat. Commun.* **8**, 14425 (2017).
18. Qiu, K. & Wegst, U. G. K. Excellent Specific Mechanical and Electrical Properties of Anisotropic Freeze-Cast Native and Carbonized Bacterial Cellulose-Alginate Foams. *Adv. Funct. Mater.* **32**, 2105635 (2022).
19. Qiu, L., Liu, J. Z., Chang, S. L. Y., Wu, Y. & Li, D. Biomimetic superelastic graphene-based cellular monoliths. *Nat. Commun.* **3**, 1241 (2012).
20. Wang, C. *et al.* Freeze-Casting Produces a Graphene Oxide Aerogel with a Radial and Centrosymmetric Structure. *ACS Nano* **12**, 5816–5825 (2018).

21. Yin, K. *et al.* Hierarchical Structure Formation by Crystal Growth-Front Instabilities During Ice Templating. *Proc. Natl. Acad. Sci.* **120**, e2210242120 (2023).
22. Lee, E.-J., Koh, Y.-H., Yoon, B.-H., Kim, H.-E. & Kim, H.-W. Highly porous hydroxyapatite bioceramics with interconnected pore channels using camphene-based freeze casting. *Mater. Lett.* **61**, 2270–2273 (2007).
23. Naviroj, M., Voorhees, P. W. & Faber, K. T. Suspension- and solution-based freeze casting for porous ceramics. *J. Mater. Res.* **32**, 3372–3382 (2017).
24. Chen, R., Wang, C.-A., Huang, Y., Ma, L. & Lin, W. Ceramics with Special Porous Structures Fabricated by Freeze-Gelcasting: Using tert-Butyl Alcohol as a Template. *J. Am. Ceram. Soc.* **90**, 3478–3484 (2007).
25. Naviroj, M., Miller, S. M., Colombo, P. & Faber, K. T. Directionally aligned macroporous SiOC via freeze casting of preceramic polymers. *J. Eur. Ceram. Soc.* **35**, 2225–2232 (2015).
26. Cui, Y., Gong, H., Wang, Y., Li, D. & Bai, H. A Thermally Insulating Textile Inspired by Polar Bear Hair. *Adv. Mater.* **30**, 1706807 (2018).
27. Zhang, Q. *et al.* 3D Printing of Graphene Aerogels. *Small* **12**, 1702–1708 (2016).
28. Caruso, I., Yin, K., Divakar, P. & Wegst, U. G. K. Tensile properties of freeze-cast collagen scaffolds: How processing conditions affect structure and performance in the dry and fully hydrated states. *J. Mech. Behav. Biomed. Mater.* 105897 (2023) doi:10.1016/j.jmbbm.2023.105897.
29. Divakar, P., Yin, K. & Wegst, U. G. K. Anisotropic freeze-cast collagen scaffolds for tissue regeneration: How processing conditions affect structure and properties in the dry and fully hydrated states. *J. Mech. Behav. Biomed. Mater.* **90**, 350–364 (2019).
30. Divakar, P., Yin, K. & Wegst, U. G. K. Values and property charts for anisotropic freeze-cast collagen scaffolds for tissue regeneration. *Data Brief* **22**, 502–507 (2019).

31. Yin, K., Divakar, P. & Wegst, U. G. K. Plant-Derived Nanocellulose as Structural and Mechanical Reinforcement of Freeze-Cast Chitosan Scaffolds for Biomedical Applications. *Biomacromolecules* **20**, 3733–3745 (2019).
32. Yin, K., Divakar, P. & Wegst, U. G. K. Freeze-casting porous chitosan ureteral stents for improved drainage. *Acta Biomater* **84**, 231–241 (2019).
33. Yin, K., Divakar, P. & Wegst, U. G. K. Structure-property-processing correlations of longitudinal freeze-cast chitosan scaffolds for biomedical applications. *J Mech Behav Biomed Mater* **121**, 104589 (2021).
34. Kamm, P. H. *et al.* X-Ray Tomoscopy Reveals the Dynamics of Ice Templating. *Adv. Funct. Mater.* 2304738 (2023) doi:10.1002/adfm.202304738.
35. García-Moreno, F. *et al.* Using X-ray tomoscopy to explore the dynamics of foaming metal. *Nat. Commun.* **10**, 3762 (2019).
36. García-Moreno, F. *et al.* Tomoscopy: Time-Resolved Tomography for Dynamic Processes in Materials. *Adv. Mater.* **33**, 2104659 (2021).
37. García-Moreno, F., Neu, T. R., Kamm, P. H. & Banhart, J. X-ray Tomography and Tomoscopy on Metals: A Review. *Adv. Eng. Mater.* **25**, 2201355 (2023).
38. Betz, O. *et al.* Imaging applications of synchrotron X-ray phase-contrast microtomography in biological morphology and biomaterials science. I. General aspects of the technique and its advantages in the analysis of millimetre-sized arthropod structure. *J. Microsc.* **227**, 51–71 (2007).
39. Withers, P. J. *et al.* X-ray computed tomography. *Nat. Rev. Methods Primer* **1**, 1–21 (2021).
40. Yashiro, W., Voegeli, W. & Kudo, H. Exploring Frontiers of 4D X-ray Tomography. *Appl. Sci.* **11**, 8868 (2021).

41. Deville, S., Adrien, J., Maire, E., Scheel, M. & Di Michiel, M. Time-lapse, three-dimensional in situ imaging of ice crystal growth in a colloidal silica suspension. *Acta Mater.* **61**, 2077–2086 (2013).

42. Deville, S. *et al.* In Situ X-Ray Radiography and Tomography Observations of the Solidification of Aqueous Alumina Particle Suspensions—Part I: Initial Instants. *J. Am. Ceram. Soc.* **92**, 2489–2496 (2009).

43. Deville, S. *et al.* In Situ X-Ray Radiography and Tomography Observations of the Solidification of Aqueous Alumina Particles Suspensions. Part II: Steady State. *J. Am. Ceram. Soc.* **92**, 2497–2503 (2009).

44. Kamm, P. H., Neu, T. R., García-Moreno, F. & Banhart, J. Nucleation and growth of gas bubbles in AlSi8Mg4 foam investigated by X-ray tomoscopy. *Acta Mater.* **206**, 116583 (2021).

45. Maire, E., Le Bourlot, C., Adrien, J., Mortensen, A. & Mokso, R. 20 Hz X-ray tomography during an in situ tensile test. *Int. J. Fract.* **200**, 3–12 (2016).

46. Maire, E. & Withers, P. J. Quantitative X-ray tomography. *Int. Mater. Rev.* **59**, 1–43 (2014).

47. Seitzman, N. *et al.* Operando X-ray Tomography Imaging of Solid-State Electrolyte Response to Li Evolution under Realistic Operating Conditions. *ACS Appl. Energy Mater.* **4**, 1346–1355 (2021).

48. Tong, H., Noda, I. & Gryte, C. C. CPS 768 Formation of anisotropic ice-agar composites by directional freezing. *Colloid Polym. Sci.* **262**, 589–595 (1984).

49. Deville, S., Saiz, E. & Tomsia, A. P. Freeze casting of hydroxyapatite scaffolds for bone tissue engineering. *Biomaterials* **27**, 5480–5489 (2006).

50. Lloreda-Jurado, P. J. *et al.* Structure–processing relationships of freeze-cast iron foams fabricated with various solidification rates and post-casting heat treatment. *J. Mater. Res.* **35**, 2587–2596 (2020).

51. Waschkies, T., Oberacker, R. & Hoffmann, M. J. Investigation of structure formation during freeze-casting from very slow to very fast solidification velocities. *Acta Mater.* **59**, 5135–5145 (2011).

52. Waschkies, T., Oberacker, R. & Hoffmann, M. J. Control of Lamellae Spacing During Freeze Casting of Ceramics Using Double-Side Cooling as a Novel Processing Route. *J. Am. Ceram. Soc.* **92**, S79–S84 (2009).

53. Munch, E., Saiz, E., Tomsia, A. P. & Deville, S. Architectural Control of Freeze-Cast Ceramics Through Additives and Templating. *J. Am. Ceram. Soc.* **92**, 1534–1539 (2009).

54. Naviroj, M., Wang, M. M., Johnson, M. T. & Faber, K. T. Nucleation-controlled freeze casting of preceramic polymers for uniaxial pores in Si-based ceramics. *Scr. Mater.* **130**, 32–36 (2017).

55. Cline, C. *et al.* Heterogeneous Ice Nucleation Studied with Single-Layer Graphene. *Langmuir* **38**, 15121–15131 (2022).

56. Kurz, W. & Fisher, D. J. *Fundamentals of solidification*. (Trans Tech Publications, 1998).

57. Deville, S. *Freezing Colloids: Observations, Principles, Control, and Use: Applications in Materials Science, Life Science, Earth Science, Food Science, and Engineering*. (Springer International Publishing, 2017). doi:10.1007/978-3-319-50515-2.

58. Petrenko, V. F. & Whitworth, R. W. *Physics of Ice*. *Physics of Ice* (Oxford University Press, 2002).

59. Tiller, W. A., Jackson, K. A., Rutter, J. W. & Chalmers, B. The redistribution of solute atoms during the solidification of metals. *Acta Metall.* **1**, 428–437 (1953).

60. Mullins, W. W. & Sekerka, R. F. Stability of a Planar Interface During Solidification of a Dilute Binary Alloy. *J. Appl. Phys.* **35**, 444–451 (1964).

61. Riblett, B. W., Francis, N. L., Wheatley, M. A. & Wegst, U. G. K. Ice-Templated Scaffolds with Microridged Pores Direct DRG Neurite Growth. *Adv. Funct. Mater.* **22**, 4920–4923 (2012).

62. Heschel, I., Lückge, C., Rödder, M., Garberding, C. & Rau, G. Possible Applications of Directional Solidification Techniques in Cyobiology. in *Advances in Cryogenic Engineering* (ed. Kittel, P.) vol. 41 13–19 (Springer US, 1996).

63. Arai, N. & Faber, K. T. Gradient-controlled freeze casting of preceramic polymers. *J. Eur. Ceram. Soc.* **43**, 1904–1911 (2023).

64. Bouville, F. *et al.* Templated Grain Growth in Macroporous Materials. *J. Am. Ceram. Soc.* **97**, 1736–1742 (2014).

65. Pawelec, K. M., Husmann, A., Best, S. M. & Cameron, R. E. Understanding anisotropy and architecture in ice-templated biopolymer scaffolds. *Mater. Sci. Eng. C* **37**, 141–147 (2014).

66. Bai, H., Chen, Y., Delattre, B., Tomsia, A. P. & Ritchie, R. O. Bioinspired large-scale aligned porous materials assembled with dual temperature gradients. *Sci. Adv.* **1**, e1500849 (2015).

67. Davidenko, N. *et al.* Biomimetic collagen scaffolds with anisotropic pore architecture. *Acta Biomater.* **8**, 667–676 (2012).

68. Harley, B. A., Hastings, A. Z., Yannas, I. V. & Sannino, A. Fabricating tubular scaffolds with a radial pore size gradient by a spinning technique. *Biomaterials* **27**, 866–874 (2006).

69. Su, F. Y., Mok, J. R. & McKittrick, J. Radial-Concentric Freeze Casting Inspired by Porcupine Fish Spines. *Ceramics* **2**, 161–179 (2019).

70. Yin, K., Mylo, M. D., Speck, T. & Wegst, U. G. K. 2D and 3D graphical datasets for bamboo-inspired tubular scaffolds with functional gradients: micrographs and tomograms. *Data Brief* **31**, 105870 (2020).

71. Yin, K., Mylo, M. D., Speck, T. & Wegst, U. G. K. Bamboo-inspired tubular scaffolds with functional gradients. *J Mech Behav Biomed Mater* **110**, 103826 (2020).

72. Li, D., Bu, X., Xu, Z., Luo, Y. & Bai, H. Bioinspired Multifunctional Cellular Plastics with a Negative Poisson's Ratio for High Energy Dissipation. *Adv. Mater.* **32**, 2001222 (2020).

73. Tian, L. *et al.* Tailoring centripetal metamaterial with superelasticity and negative Poisson's ratio for organic solvents adsorption. *Sci. Adv.* **8**, eabo1014 (2022).

74. Niksiar, P., Frank, M. B., McKittrick, J. & Porter, M. M. Microstructural evolution of paramagnetic materials by magnetic freeze casting. *J. Mater. Res. Technol.* **8**, 2247–2254 (2019).

75. Yin, K., Reese, B. A., Sullivan, C. R. & Wegst, U. G. K. Superior Mechanical and Magnetic Performance of Highly Anisotropic Sendust-Flake Composites Freeze Cast in a Uniform Magnetic Field. *Adv. Funct. Mater.* **31**, (2020).

76. Tang, Y., Qiu, S., Miao, Q. & Wu, C. Fabrication of lamellar porous alumina with axisymmetric structure by directional solidification with applied electric and magnetic fields. *J. Eur. Ceram. Soc.* **36**, 1233–1240 (2016).

77. Tang, Y. F., Zhao, K., Wei, J. Q. & Qin, Y. S. Fabrication of aligned lamellar porous alumina using directional solidification of aqueous slurries with an applied electrostatic field. *J. Eur. Ceram. Soc.* **30**, 1963–1965 (2010).

78. Ogden, T. A., Prisbrey, M., Nelson, I., Raeymaekers, B. & Naleway, S. E. Ultrasound freeze casting: Fabricating bioinspired porous scaffolds through combining freeze casting and ultrasound directed self-assembly. *Mater. Des.* **164**, 107561 (2019).

79. Porter, M. M. *et al.* Torsional properties of helix-reinforced composites fabricated by magnetic freeze casting. *Compos. Struct.* **119**, 174–184 (2015).

80. Moritz, T. & Richter, H.-J. Ice-mould freeze casting of porous ceramic components. *J. Eur. Ceram. Soc.* **27**, 4595–4601 (2007).

81. Yu, R. *et al.* Graphene Oxide/Chitosan Aerogel Microspheres with Honeycomb-Cobweb and Radially Oriented Microchannel Structures for Broad-Spectrum and Rapid Adsorption of Water Contaminants. *ACS Appl. Mater. Interfaces* **9**, 21809–21819 (2017).

82. Shen, H. *et al.* Scalable Freeze-Tape-Casting Fabrication and Pore Structure Analysis of 3D LLZO Solid-State Electrolytes. *ACS Appl. Mater. Interfaces* **12**, 3494–3501 (2020).

83. Chen, Y., Bunch, J., Li, T., Mao, Z. & Chen, F. Novel functionally graded acicular electrode for solid oxide cells fabricated by the freeze-tape-casting process. *J. Power Sources* **213**, 93–99 (2012).

84. Guo, Y., Jiang, Y., Zhang, Q., Wan, D. & Huang, C. Directional LiFePO4 cathode structure by freeze tape casting to improve lithium ion diffusion kinetics. *J. Power Sources* **506**, 230052 (2021).

85. Hwa, Y. *et al.* Three-Dimensionally Aligned Sulfur Electrodes by Directional Freeze Tape Casting. *Nano Lett.* **19**, 4731–4737 (2019).

86. Parikh, D. & Li, J. Bilayer hybrid graphite anodes via freeze tape casting for extreme fast charging applications. *Carbon* **196**, 525–531 (2022).

87. Sofie, S. W. Fabrication of Functionally Graded and Aligned Porosity in Thin Ceramic Substrates With the Novel Freeze–Tape-Casting Process. *J. Am. Ceram. Soc.* **90**, 2024–2031 (2007).

88. Yang, W. *et al.* Freeze-assisted Tape Casting of Vertically Aligned MXene Films for High Rate Performance Supercapacitors. *ENERGY Environ. Mater.* **3**, 380–388 (2020).

89. Xiong, Z., Yan, Y., Wang, S., Zhang, R. & Zhang, C. Fabrication of porous scaffolds for bone tissue engineering via low-temperature deposition. *Scr. Mater.* **46**, 771–776 (2002).

90. Song, X. *et al.* Biomimetic 3D Printing of Hierarchical and Interconnected Porous Hydroxyapatite Structures with High Mechanical Strength for Bone Cell Culture. *Adv. Eng. Mater.* **21**, 1800678 (2019).

91. Snyder, J. E. *et al.* Combined multi-nozzle deposition and freeze casting process to superimpose two porous networks for hierarchical three-dimensional microenvironment. *Biofabrication* **6**, 015007 (2014).

92. Reed, S. *et al.* Macro- and micro-designed chitosan-alginate scaffold architecture by three-dimensional printing and directional freezing. *Biofabrication* **8**, 015003 (2016).

93. Körber, C., Scheiwe, M.-W. & Wollhöver, K. A cryomicroscope for the analysis of solute polarization during freezing. *Cryobiology* **21**, 68–80 (1984).

94. Körber, Ch. *et al.* Low temperature light microscopy and its application to study freezing in aqueous solutions and biological cell suspensions. *J. Microsc.* **141**, 263–276 (1986).

95. Rubinsky, B. & Ikeda, M. A cryomicroscope using directional solidification for the controlled freezing of biological material. *Cryobiology* **22**, 55–68 (1985).

96. Dedovets, D., Monteux, C. & Deville, S. Five-dimensional imaging of freezing emulsions with solute effects. *Science* **360**, 303–306 (2018).

97. Dedovets, D., Monteux, C. & Deville, S. A temperature-controlled stage for laser scanning confocal microscopy and case studies in materials science. *Ultramicroscopy* **195**, 1–11 (2018).

98. Dedovets, D. & Deville, S. Multiphase imaging of freezing particle suspensions by confocal microscopy. *J. Eur. Ceram. Soc.* **38**, 2687–2693 (2018).

99. Marcellini, M., Noirjean, C., Dedovets, D., Maria, J. & Deville, S. Time-lapse, in situ imaging of ice crystal growth using confocal microscopy. *ACS Omega* **1**, 1019–1026 (2016).

100. Körber, Ch., Rau, G., Cosman, M. D. & Cravalho, E. G. Interaction of particles and a moving ice-liquid interface. *J. Cryst. Growth* **72**, 649–662 (1985).

101. Lipp, G., Körber, Ch. & Rau, G. Critical growth rates of advancing ice-water interfaces for particle encapsulation. *J. Cryst. Growth* **99**, 206–210 (1990).

102. Fabietti, L. M., Seetharaman, V. & Trivedi, R. The development of solidification microstructures in the presence of lateral constraints. *Metall. Trans. A* **21**, 1299–1310 (1990).

103. Mota, F. L., Fabietti, L. M., Bergeon, N. & Trivedi, R. The effect of confinement on thermal convection and longitudinal macrosegregation in directionally solidified dilute succinonitrile–camphor alloy. *Comptes Rendus Mécanique* **351**, 1–14 (2023).

104. Hoshino, M., Uesugi, K. & Yagi, N. 4D x-ray phase contrast tomography for repeatable motion of biological samples. *Rev. Sci. Instrum.* **87**, 093705 (2016).

105. Escauriza, E. M. *et al.* Ultra-high-speed indirect x-ray imaging system with versatile spatiotemporal sampling capabilities. *Appl. Opt.* **57**, 5004–5010 (2018).

106. Vagovič, P. *et al.* Megahertz x-ray microscopy at x-ray free-electron laser and synchrotron sources. *Optica* **6**, 1106–1109 (2019).

107. Bareggi, A., Maire, E., Lasalle, A. & Deville, S. Dynamics of the Freezing Front During the Solidification of a Colloidal Alumina Aqueous Suspension: In Situ X-Ray Radiography, Tomography, and Modeling. *J. Am. Ceram. Soc.* **94**, 3570–3578 (2011).

108. Yang, G. *et al. In situ* imaging of three dimensional freeze printing process using rapid x-ray synchrotron radiography. *Rev. Sci. Instrum.* **93**, 013703 (2022).

109. Lohse, L. M. *et al.* A phase-retrieval toolbox for X-ray holography and tomography. *J. Synchrotron Radiat.* **27**, 852–859 (2020).

110. Paganin, D., Mayo, S. C., Gureyev, T. E., Miller, P. R. & Wilkins, S. W. Simultaneous phase and amplitude extraction from a single defocused image of a homogeneous object. *J. Microsc.* **206**, 33–40 (2002).

111. Weitkamp, T., Haas, D., Wegrzynek, D. & Rack, A. ANKAphase: software for single-distance phase retrieval from inline X-ray phase-contrast radiographs. *J. Synchrotron Radiat.* **18**, 617–629 (2011).

112. Schneider, C. A., Rasband, W. S. & Eliceiri, K. W. NIH Image to ImageJ: 25 years of image analysis. *Nat. Methods* **9**, 671–675 (2012).

113. Schindelin, J. *et al.* Fiji: an open-source platform for biological-image analysis. *Nat. Methods* **9**, 676–682 (2012).

114. Object Research Systems. Dragonfly. (2023).

115. Thermo Fisher Scientific. Avizo. (2023).

116. Tsai, E. H. R., Marone, F. & Guizar-Sicairos, M. Gridrec-MS: an algorithm for multi-slice tomography. *Opt. Lett.* **44**, 2181–2184 (2019).

117. Arganda-Carreras, I. *et al.* Trainable Weka Segmentation: a machine learning tool for microscopy pixel classification. *Bioinformatics* **33**, 2424–2426 (2017).

118. Arzt, M. *et al.* LABKIT: Labeling and Segmentation Toolkit for Big Image Data. *Front. Comput. Sci.* **4**, 777728 (2022).

119. Ronneberger, O., Fischer, P. & Brox, T. U-Net: Convolutional Networks for Biomedical Image Segmentation. in *Medical Image Computing and Computer-Assisted Intervention – MICCAI 2015* (eds. Navab, N., Hornegger, J., Wells, W. M. & Frangi, A. F.) vol. 9351 234–241 (Springer International Publishing, 2015).

120. Berg, S. *et al.* ilastik: interactive machine learning for (bio)image analysis. *Nat. Methods* **16**, 1226–1232 (2019).

121. Ollion, J., Cochennec, J., Loll, F., Escudé, C. & Boudier, T. TANGO: a generic tool for high-throughput 3D image analysis for studying nuclear organization. *Bioinformatics* **29**, 1840–1841 (2013).

122. Van Der Walt, S. *et al.* scikit-image: image processing in Python. *PeerJ* **2**, e453 (2014).

123. Legland, D., Arganda-Carreras, I. & Andrey, P. MorphoLibJ: integrated library and plugins for mathematical morphology with ImageJ. *Bioinformatics* **32**, 3532–3534 (2016).

124. Haase, R. *et al.* CLIJ: GPU-accelerated image processing for everyone. *Nat. Methods* **17**, 5–6 (2020).

125. Abdullayev, A., Kamm, P. H., Bekheet, M. F. & Gurlo, A. Fabrication and Characterization of Ice Templated Membrane Supports from Portland Cement. *Membranes* **10**, 93 (2020).

126. Henning, L. M. *et al.* Manufacturing and Characterization of Highly Porous Bioactive Glass Composite Scaffolds Using Unidirectional Freeze Casting. *Adv. Eng. Mater.* **19**, 1700129 (2017).

127. Yin, K., Primel, T., Harrington, M. J. & Wegst, U. G. K. Collagen Fibrillation and Chitosan Self-assembly by Dynamic Shear during Freeze Casting. *submitted* (2023).

128. Püspöki, Z., Storath, M., Sage, D. & Unser, M. Transforms and Operators for Directional Bioimage Analysis: A Survey. in *Focus on Bio-Image Informatics* (eds. De Vos, W. H., Munck, S. & Timmermans, J.-P.) 69–93 (Springer International Publishing, 2016). doi:10.1007/978-3-319-28549-8_3.

129. Ashby, M. F. The properties of foams and lattices. *Philos. Trans. R. Soc. Math. Phys. Eng. Sci.* **364**, 15–30 (2006).

130. Gibson, L. J. & Ashby, M. F. *Cellular Solids: Structure and Properties*. (Cambridge University Press, 1997).

131. Hua, M. *et al.* Strong tough hydrogels via the synergy of freeze-casting and salting out. *Nature* **590**, 594–599 (2021).

132. Delattre, B. *et al.* Impact of Pore Tortuosity on Electrode Kinetics in Lithium Battery Electrodes: Study in Directionally Freeze-Cast LiNi0.8Co0.15Al0.05O2 (NCA). *J. Electrochem. Soc.* **165**, A388 (2018).

133. Miao, S., Wang, Y., Sun, L. & Zhao, Y. Freeze-derived heterogeneous structural color films. *Nat. Commun.* **13**, 4044 (2022).

134. Shao, G., Hanaor, D. A. H., Shen, X. & Gurlo, A. Freeze Casting: From Low-Dimensional Building Blocks to Aligned Porous Structures—A Review of Novel Materials, Methods, and Applications. *Adv. Mater.* **32**, 1907176 (2020).

135. Liu, Y., Zhu, W., Guan, K., Peng, C. & Wu, J. Freeze-casting of alumina ultra-filtration membranes with good performance for anionic dye separation. *Ceram. Int.* **44**, 11901–11904 (2018).

136. Du, Z. *et al.* The sound absorption performance of the highly porous silica ceramics prepared using freeze casting method. *J. Am. Ceram. Soc.* **103**, 5990–5998 (2020).

137. Bian, R. *et al.* Ultralight MXene-based aerogels with high electromagnetic interference shielding performance. *J. Mater. Chem. C* **7**, 474–478 (2019).

138. Li, P.-X. *et al.* Bidirectionally aligned MXene hybrid aerogels assembled with MXene nanosheets and microgels for supercapacitors. *Rare Met.* **42**, 1249–1260 (2023).

139. Sani, E., Landi, E., Sciti, D. & Medri, V. Optical properties of ZrB2 porous architectures. *Sol. Energy Mater. Sol. Cells* **144**, 608–615 (2016).

140. Huang, J. *et al.* Oriented freeze-casting fabrication of resilient copper nanowire-based aerogel as robust piezoresistive sensor. *Chem. Eng. J.* **364**, 28–36 (2019).

141. Ezekwo, G., Tong, H.-M. & Gryte, C. C. On the mechanism of dewatering colloidal aqueous solutions by freeze-thaw processes. *Water Res.* **14**, 1079–1088 (1980).

142. Tong, H. & Gryte, C. Mechanism of lamellar spacing adjustment in directionally frozen agar gels. *Colloid Polym. Sci.* **263**, 147–155 (1985).

143. Campbell, J. J., Husmann, A., Hume, R. D., Watson, C. J. & Cameron, R. E. Development of three-dimensional collagen scaffolds with controlled architecture for cell migration studies using breast cancer cell lines. *Biomaterials* **114**, 34–43 (2017).

144. Davidenko, N. *et al.* Biomimetic collagen scaffolds with anisotropic pore architecture. *Acta Biomater.* **8**, 667–676 (2012).

145. Offeddu, G. S., Ashworth, J. C., Cameron, R. E. & Oyen, M. L. Multi-scale mechanical response of freeze-dried collagen scaffolds for tissue engineering applications. *J. Mech. Behav. Biomed. Mater.* **42**, 19–25 (2015).

146. Schoof, H., Apel, J., Heschel, I. & Rau, G. Control of pore structure and size in freeze-dried collagen sponges. *J. Biomed. Mater. Res.* **58**, 352–357 (2001).

147. Kuberka, M., Heschel, I. & Glasmacher, B. Preparation of Collagen Scaffolds and their Applications in Tissue Engineering. *Biomed. Tech. Eng.* **47**, 485–487 (2002).

148. Munier, P., Gordeyeva, K., Bergström, L. & Fall, A. B. Directional freezing of nanocellulose dispersions aligns the rod-like particles and produces low-density and robust particle networks. *Biomacromolecules* **17**, 1875–1881 (2016).

149. Bai, H. *et al.* Biomimetic gradient scaffold from ice-templating for self-seeding of cells with capillary effect. *Acta Biomater.* **20**, 113–119 (2015).

150. Bozkurt, A. *et al.* In vitro cell alignment obtained with a Schwann cell enriched microstructured nerve guide with longitudinal guidance channels. *Biomaterials* **30**, 169–179 (2009).

151. Meghri, N. W. *et al.* Directionally solidified biopolymer scaffolds: Mechanical properties and endothelial cell responses. *JOM* **62**, 71–75 (2010).

152. Mohan, S. *et al.* Fluorescent Reporter Mice for Nerve Guidance Conduit Assessment: A High-Throughput in vivo Model. *The Laryngoscope* **128**, E386–E392 (2018).

153. von Heimburg, D. *et al.* Human preadipocytes seeded on freeze-dried collagen scaffolds investigated in vitro and in vivo. *Biomaterials* **22**, 429–438 (2001).

154. Möllers, S. *et al.* Cytocompatibility of a Novel, Longitudinally Microstructured Collagen Scaffold Intended for Nerve Tissue Repair. *Tissue Eng. Part A* **15**, 461–472 (2009).

155. Bozkurt, A. *et al.* Efficient bridging of 20 mm rat sciatic nerve lesions with a longitudinally micro-structured collagen scaffold. *Biomaterials* **75**, 112–122 (2016).

156. Divakar, P. *et al.* High-plex expression profiling reveals that implants drive spatiotemporal protein production and innate immune activation for tissue repair. *Acta Biomater.* **138**, 342–350 (2022).

157. Divakar, P., Moodie, K. L., Demidenko, E., Hoopes, P. J. & Wegst, U. G. K. Quantitative evaluation of the in vivo biocompatibility and performance of freeze-cast tissue scaffolds. *Biomed. Mater.* (2019) doi:10.1088/1748-605X/ab316a.

158. Divakar, P. *et al.* Design, Manufacture, and In vivo Testing of a Tissue Scaffold for Permanent Female Sterilization by Tubal Occlusion. *MRS Adv.* **3**, 1685–1690 (2018).

159. Jiang, S.-J. *et al.* Radially Porous Nanocomposite Scaffolds with Enhanced Capability for Guiding Bone Regeneration In Vivo. *Adv. Funct. Mater.* **32**, 2110931 (2022).

160. Yin, K. *et al.* Freeze-cast Porous Chitosan Conduit for Peripheral Nerve Repair. *MRS Adv* **3**, 1677–1683 (2018).

161. Divakar, P., Trembly, B. S., Moodie, K. L., Hoopes, P. J. & Wegst, U. G. K. Preliminary assessment of a hysteroscopic fallopian tube heat and biomaterial

technology for permanent female sterilization. in (ed. Ryan, T. P.) 100660A (2017). doi:10.1117/12.2255843.

162. Li, J. *et al.* Radial Sponges Facilitate Wound Healing by Promoting Cell Migration and Angiogenesis. *Adv. Healthc. Mater.* **12**, 2202737 (2023).
163. Fu, Q., Rahaman, M. N., Dogan, F. & Bal, B. S. Freeze-cast hydroxyapatite scaffolds for bone tissue engineering applications. *Biomed. Mater.* **3**, 025005 (2008).
164. Xia, Z. *et al.* Fabrication and characterization of biomimetic collagen–apatite scaffolds with tunable structures for bone tissue engineering. *Acta Biomater.* **9**, 7308–7319 (2013).
165. Fu, Q., Rahaman, M. N., Dogan, F. & Bal, B. S. Freeze casting of porous hydroxyapatite scaffolds. I. Processing and general microstructure. *J. Biomed. Mater. Res. B Appl. Biomater.* **86B**, 125–135 (2008).
166. Fu, Q., Rahaman, M. N., Dogan, F. & Bal, B. S. Freeze casting of porous hydroxyapatite scaffolds. II. Sintering, microstructure, and mechanical behavior. *J. Biomed. Mater. Res. B Appl. Biomater.* **86B**, 514–522 (2008).
167. Yin, T. J. & Naleway, S. E. Freeze Casting with Bioceramics for Bone Graft Substitutes. *Biomed. Mater. Devices* **1**, 366–387 (2023).
168. Jackson, A. P., Vincent, J. F. V., Turner, R. M. & Alexander, R. M. The mechanical design of nacre. *Proc. R. Soc. Lond. B Biol. Sci.* **234**, 415–440 (1988).
169. Deville, S., Saiz, E. & Tomsia, A. P. Ice-templated porous alumina structures. *Acta Mater.* **55**, 1965–1974 (2007).
170. Launey, M. E. *et al.* Designing highly toughened hybrid composites through nature-inspired hierarchical complexity. *Acta Mater.* **57**, 2919–2932 (2009).
171. Wegst, U. G. K., Bai, H., Saiz, E., Tomsia, A. P. & Ritchie, R. O. Bioinspired structural materials. *Nat. Mater.* **14**, 23–36 (2015).

172. Roy, S., Frohnheiser, J. & Wanner, A. Effect of ceramic preform freeze-casting temperature and melt infiltration technique on the mechanical properties of a lamellar metal/ceramic composite. *J. Compos. Mater.* **54**, 2001–2011 (2020).

173. Zeng, Z., Wu, N., Liu, J. & Nyström, G. Mimicking biological architectures via freeze casting. *Matter* **5**, 2519–2522 (2022).

174. Huang, L. *et al.* A compound scaffold with uniform longitudinally oriented guidance cues and a porous sheath promotes peripheral nerve regeneration in vivo. *Acta Biomater.* **68**, 223–236 (2018).

175. Francis, N. L. *et al.* An ice-templated, linearly aligned chitosan-alginate scaffold for neural tissue engineering. *J. Biomed. Mater. Res. A* **101**, 3493–3503 (2013).

176. Stokols, S. & Tuszynski, M. H. The fabrication and characterization of linearly oriented nerve guidance scaffolds for spinal cord injury. *Biomaterials* **25**, 5839–5846 (2004).

177. Chen, J. *et al.* Freeze-casting osteochondral scaffolds: The presence of a nutrient-permeable film between the bone and cartilage defect reduces cartilage regeneration. *Acta Biomater.* **154**, 168–179 (2022).

178. Stoppel, W. L., Hu, D., Domian, I. J., Kaplan, D. L. & Lauren D. Black, I. I. I. Anisotropic Silk Biomaterials Containing Cardiac Extracellular Matrix for Cardiac Tissue Engineering. *Biomed. Mater. Bristol Engl.* **10**, 034105 (2015).

179. Cao, S. *et al.* Shape memory and antibacterial chitosan-based cryogel with hemostasis and skin wound repair. *Carbohydr. Polym.* **305**, 120545 (2023).

180. Wegst, U. G. K., Allen, T. & Sridharan, K. *Freeze-casting as a Novel Manufacturing Process for Fast Reactor Fuels. Final Report*. DOE/NEUP--10-848, 1154737 http://www.osti.gov/servlets/purl/1154737/ (2014) doi:10.2172/1154737.

181. Wang, J., Xu, Z., Eloi, J.-C., Titirici, M.-M. & Eichhorn, S. J. Ice-Templated, Sustainable Carbon Aerogels with Hierarchically Tailored Channels for Sodium- and Potassium-Ion Batteries. *Adv. Funct. Mater.* **32**, 2110862 (2022).

182. Amin, R., Delattre, B., Tomsia, A. P. & Chiang, Y.-M. Electrochemical Characterization of High Energy Density Graphite Electrodes Made by Freeze-Casting. *ACS Appl. Energy Mater.* **1**, 4976–4981 (2018).

183. Sun, H. *et al.* Hierarchical 3D electrodes for electrochemical energy storage. *Nat. Rev. Mater.* **4**, 45–60 (2019).

184. Dang, D., Wang, Y., Gao, S. & Cheng, Y.-T. Freeze-dried low-tortuous graphite electrodes with enhanced capacity utilization and rate capability. *Carbon* **159**, 133–139 (2020).

185. Parikh, D. & Li, J. Bilayer hybrid graphite anodes via freeze tape casting for extreme fast charging applications. *Carbon* **196**, 525–531 (2022).

186. Thomas, B. *et al.* Ice-Templating of Lignin and Cellulose Nanofiber-Based Carbon Aerogels: Implications for Energy Storage Applications. *ACS Appl. Nano Mater.* **5**, 7954–7966 (2022).

187. Shao, Y. *et al.* 3D Freeze-Casting of Cellular Graphene Films for Ultrahigh-Power-Density Supercapacitors. *Adv. Mater.* **28**, 6719–6726 (2016).

188. Wilke, S. K. & Dunand, D. C. Structural evolution of directionally freeze-cast iron foams during oxidation/reduction cycles. *Acta Mater.* **162**, 90–102 (2019).

189. Zhao, Z. *et al.* Sandwich, Vertical-Channeled Thick Electrodes with High Rate and Cycle Performance. *Adv. Funct. Mater.* **29**, 1809196 (2019).

190. Zhang, X. *et al.* Tunable Porous Electrode Architectures for Enhanced Li-Ion Storage Kinetics in Thick Electrodes. *Nano Lett.* **21**, 5896–5904 (2021).

191. Lee, J. T., Jo, C. & De Volder, M. Bicontinuous phase separation of lithium-ion battery electrodes for ultrahigh areal loading. *Proc. Natl. Acad. Sci.* **117**, 21155–21161 (2020).

192. Huang, C. & Grant, P. S. Coral-like directional porosity lithium ion battery cathodes by ice templating. *J. Mater. Chem. A* **6**, 14689–14699 (2018).

193. Azami-Ghadkolai, M., Yousefi, M., Allu, S., Creager, S. & Bordia, R. Effect of isotropic and anisotropic porous microstructure on electrochemical performance of Li ion battery cathodes: An experimental and computational study. *J. Power Sources* **474**, 228490 (2020).

194. Noël, J. A. & White, M. A. Freeze-cast form-stable phase change materials for thermal energy storage. *Sol. Energy Mater. Sol. Cells* **223**, 110956 (2021).

195. Andrews, E. W., Gioux, G., Onck, P. & Gibson, L. J. Size effects in ductile cellular solids. Part II: experimental results. *Int. J. Mech. Sci.* **43**, 701–713 (2001).

196. Onck, P. R., Andrews, E. W. & Gibson, L. J. Size effects in ductile cellular solids. Part I: modeling. *Int. J. Mech. Sci.* **43**, 681–699 (2001).

197. ASTM E9-09. Standard Test Methods of Compression Testing of Metallic Materials at Room Temperature. (2018) doi:10.1520/E0009-09.

198. Abba, M. T., Hunger, P. M., Kalidindi, S. R. & Wegst, U. G. K. Nacre-like hybrid films: Structure, properties, and the effect of relative humidity. *J. Mech. Behav. Biomed. Mater.* **55**, 140–150 (2016).

199. Offeddu, G. S., Ashworth, J. C., Cameron, R. E. & Oyen, M. L. Structural determinants of hydration, mechanics and fluid flow in freeze-dried collagen scaffolds. *Acta Biomater.* **41**, 193–203 (2016).

200. Liu, Y., Zhai, W. & Zeng, K. Study of the Freeze Casting Process by Artificial Neural Networks. *ACS Appl. Mater. Interfaces* **12**, 40465–40474 (2020).

201. Ashby, M. F. *Materials selection in mechanical design*. (Elsevier, 2016).

202. Ansys. Granta Constructor & Selector 2020 Software. (2020).

203. Lao, W., Yin, K., Li, T. & Huang, H. BEANS: Property Chart Plotter. (2022) doi:10.5281/zenodo.7261667.

204. Fast tomography data base. http://tinyurl.com/Fast-Tomography (2023).

205. Kamm, P. H., Garcia-Moreno, F. & Schlepütz, C. M. Tomoscopy Experiments Data Base. http://resolution.tomoscopy.net (2023).

206. Carlo, F. D. *et al.* TomoBank: a tomographic data repository for computational x-ray science. *Meas. Sci. Technol.* **29**, 034004 (2018).

207. Liu, H., Jiang, J. & Zhai, W. Bubble freeze casting artificial rattan. *Chem. Eng. J.* **449**, 137870 (2022).

208. Petersen, A. *et al.* A biomaterial with a channel-like pore architecture induces endochondral healing of bone defects. *Nat. Commun.* **9**, 4430 (2018).

209. Chen, D. *et al.* Drilling by light: ice-templated photo-patterning enabled by a dynamically crosslinked hydrogel. *Mater. Horiz.* **6**, 1013–1019 (2019).

210. Erlandsson, J. *et al.* On the mechanism behind freezing-induced chemical crosslinking in ice-templated cellulose nanofibril aerogels. *J. Mater. Chem. A* **6**, 19371–19380 (2018).

211. Warburton, L. & Rubinsky, B. Freezing-modulated-crosslinking: A crosslinking approach for 3D cryoprinting. *Bioprinting* **27**, e00225 (2022).

212. Nelson, I., Gardner, L., Carlson, K. & Naleway, S. E. Freeze casting of iron oxide subject to a tri-axial nested Helmholtz-coils driven uniform magnetic field for tailored porous scaffolds. *Acta Mater.* **173**, 106–116 (2019).

213. Jha, P. K., Xanthakis, E., Jury, V. & Le-Bail, A. An Overview on Magnetic Field and Electric Field Interactions with Ice Crystallisation; Application in the Case of Frozen Food. *Crystals* **7**, 299 (2017).

214. *Fennema's Food Chemistry*. (CRC Press, 2007). doi:10.1201/9781420020526.

215. Guan, J., Porter, D., Tian, K., Shao, Z. & Chen, X. Morphology and mechanical properties of soy protein scaffolds made by directional freezing. *J. Appl. Polym. Sci.* **118**, 1658–1665 (2010).

216. Deville, S. *et al.* Ice Shaping Properties, Similar to That of Antifreeze Proteins, of a Zirconium Acetate Complex. *PLoS ONE* **6**, (2011).

217. Dang, D., Wang, Y., Gao, S. & Cheng, Y.-T. Freeze-dried low-tortuous graphite electrodes with enhanced capacity utilization and rate capability. *Carbon* **159**, 133–139 (2020).

218. Deville, S., Meille, S. & Seuba, J. A meta-analysis of the mechanical properties of ice-templated ceramics and metals. *Sci. Technol. Adv. Mater.* **16**, 043501 (2015).

219. Hautcoeur, D. *et al.* Thermal conductivity of ceramic/metal composites from preforms produced by freeze casting. *Ceram. Int.* **42**, 14077–14085 (2016).

220. Pawelec, K. M., Husmann, A., Best, S. M. & Cameron, R. E. A design protocol for tailoring ice-templated scaffold structure. *J. R. Soc. Interface* **11**, 20130958 (2014).

221. Labconco Corporation. *A Guide to Freeze Drying for the Laboratory*. (2010).

222. Tang, Y., Miao, Q., Qiu, S., Zhao, K. & Hu, L. Novel freeze-casting fabrication of aligned lamellar porous alumina with a centrosymmetric structure. *J. Eur. Ceram. Soc.* **34**, 4077–4082 (2014).

223. Barnett, E., Angeles, J., Pasini, D. & Sijpkes, P. Robot-assisted Rapid Prototyping for ice structures. in *2009 IEEE International Conference on Robotics and Automation* 146–151 (2009). doi:10.1109/ROBOT.2009.5152317.

Ten References of Particular Importance

Cui et al. (2018) doi: 10.1002/adma.201706807
Introduces continuous freeze-casting, in their case "freeze spinning," for the manufacture of continuous fibers with a controlled and aligned pore architecture.

Donius et al. (2014) doi: 10.1016/j.matchar.2014.04.003
The only cryogenic EBSD and SEM study, to date, reveals crystallographic orientation and morphology of a directionally solidified ice–polymer composite in the as frozen state.

Hunger et al. (2013) doi: 10.1016/j.jmbbm.2012.10.013.
Reported is the discovery of interdendritic shear flow as the mechanism for particle self-assembly and structure formation through the observation of ceramic platelets self-assembling into porous nacre during directional solidification.

Porter et al. (2012) doi: 10.1016/j.msea.2012.07.058
This first report on structural control via an externally applied field, here a magnetic one, inspires the use also of other externally applied fields, such as electric and acoustic to custom-design and control a freeze-cast materials structure and properties.

Tong et al. (1984) doi: 10.1007/BF01451524
The first report correlating temperature gradient, freezing front velocity, and lamellar spacing, and the discovery of birefringence in a freeze-cast bulk sample, implying preferential molecular alignment during the directional solidification of an aqueous binary polymer solution.

Yin et al. (2023) doi: 10.1073/pnas.2210242120
The fundamental science of ice crystal growth and ice-templating is presented with an integrated experimental and phase-field simulation approach.

Paganin et al. (2002) doi: 10.1046/j.1365-2818.2002.01010.x
Introduced is a new phase retrieval method based on the use of only one radiographic projection which signifantly enhances image contrast and data processing speeds in X-ray tomography and tomoscopy.

Mokso et al. (2017) doi: 10.1107/S1600577517013522
The high-speed X-ray image detection and readout system presented dramatically increases the total acquisition time so that dynamic processes can be observed not only at high speeds but also for a long duration of several minutes.

García Moreno et al. (2021) doi: 10.1002/adma.202104659
Several applications for X-ray tomoscopy are presented to illustrate how the dynamics of processes can be visualized and quantified with imaging rates up to 1000 tomograms per second over a period of minutes.

Kamm et al. (2023) doi: 10.1002/adfm.202304738
Introduced is X-ray tomoscopy as currently the only technique to image and quantify in 3D with high spatial and temporal resolution the dynamics of ice-crystal growth, instability formation, and ice-templating of the hierarchical architecture typical of freeze-cast materials.

Acknowledgements

The authors gratefully acknowledge financial support through through NASA Awards 80NSSC18K0305 and 80NSSC21K0039 (U.G.K.W.) and NSF-CMMI Award 1538094 (U.G.K.W.), the DFG Reinhart-Koselleck Project 408321454, Ba 1170/40 (F.G.M) and BMBF Award 05K18KTA (F.G.M), the Alexander von Humboldt Foundation for a Humboldt Research Fellowship (K.Y.), and the Paul Scherrer Institute, Villigen, Switzerland for the provision of synchrotron radiation beamtime at the TOMCAT beamline X02DA of the Swiss Light Source.

Competing Interests

The authors declare no competing interests.

Figure Captions

Figure 1. ***Schematic of the freeze casting process (centre) and examples of structural features templated in freeze-cast polymers, ceramics, and metals.*** (a) PTFE mould, sealed with copper bottom plate, filled with a solution or slurry, on a copper coldfinger, to apply a controlled cooling rate. The fastest ice crystal growth direction $\langle 11\bar{2}0 \rangle$ parallels the temperature gradient. Phase separation into pure ice and a second ice-templated phase. The graphs illustrate freezing front progressing at velocity, V, pushing ahead of it the solute partitioned into the liquid phase with an exponentially decaying concentration profile, $C > C_0$, with C_0 the initial solute concentration; solutal diffusion length $l_D = D/V$, with D the diffusion coefficient in the liquid phase. Growing ice crystals template both pore morphology and predominantly unilateral features on the cell walls: (1) smooth 'ridges' that sometimes partially detach, (2) triangular, 'shark teeth'-like undulating tips; (3) 'jellyfish'-like caps; (4) 'jellyfish tentacle'-like protrusions, which may be partially or completely detached; (5) wavy or wrinkled cell walls. (b) Schematic and freeze-cast sample illustrating the evolution of the scaffold structure with height: a thin chill layer, a cellular layer, and the desired lamellar layer.[31] The structural anisotropy of a freeze-cast material is illustrated with a transverse and a longitudinal cross sections of a freeze cast chitosan scaffold (figures adapted from [21]). (c) Schematic of a freeze cast collagen scaffold illustrating fibrillar pillars and bridges that are typical for materials made from fibrillar slurries.[29] Differences in particle packing of small and large particles, a bimodal particle size distribution of 7:3 large:small, and platelets. [22,2]

Figure 2. ***(a) An overview of freeze caster and mould designs and resulting domain shape and lamellar orientation in (b) 2D and (c) 3D.*** Typical moulds for batch-type coldfinger-based freeze casting include: (a) PTFE tubes for unidirectional solidification starting at the copper mould bottom cooled by a coldfinger [1,5,48] (b) Controlling the temperature at both ends of the mould, two different solidification scenarios can be achieved: a constant thermal gradient, G, which results in uniform structural features along the length of the mould, well controlled variations of G during sample manufacture, or ice nucleation and growth from both mould ends [52,146]. (c) Adding an insulating polydimethylsiloxane (PDMS) wedge, usually in a mould with a square cross-section, a dual temperature gradient is formed; with this approach almost mono-domain samples with long-range order at the centimeter scale can be achieved [66]. (d) By adding a copper or other thermally conducting centre pin to a thermally conductive cylindrical mould, radial porosity is created, which nucleates at both cold surfaces with freezing fronts meeting at a position, which can be defined by the relative thermal conductivities of mould wall and pin [70,71]. (e) An externally applied magnetic field (B-field), generated either by a permanent magnet or Helmholtz coils, determine particle orientation and distribution of magnetic and surface magnetized materials: uniform B-field results in particle rotation without translation [75,212]; the application of a magnetic field also affects ice crystal growth [213].

Figure 3. ***Dynamic structural characterization of crystal growth processes with tomoscopy***. (a) Schematic of the typical configuration of an X-ray tomoscopic setup at a synchrotron [34]. (b) Schematic view of the freeze casting process (for details see Figure 1). The temperature of the copper coldfinger, with which the applied cooling rate is defined, is controlled by a cryogenic jet. (c) Schematic comparing absorption and phase contrast signals during a Synchrotron X-ray tomography [38]. A small distance between sample and detector leads to mainly absorption contrast, a larger distance improves the phase contrast. The corresponding reconstructed images are shown. (d) Tomogram of a freeze-cast sample with color-coded ice lamella mean thickness. (e) A 2D slice with a magnified section of a vertical cut through a tomogram during crystal growth [34].

Figure 4. ***Overview of in situ and post mortem techniques to characterize the dynamics of ice crystal growth and ice templating during solidification and the hierarchical material***

architecture that results ordered by length scale. In situ techniques: (A) Optical microscopy [8]. (B) Confocal microscopy [96]. (C) X-ray radioscopy [42]. (D) X-ray tomoscopy [34]. Post mortem techniques: Optical microscopy, X-ray tomography, Confocal microscopy, Scanning Electron Microscopy (SEM), and Transmission electron microscopy (TEM). (E) Hierarchical sample architecture imaged by X-ray tomography. [5] (F) Pore size, geometry and distribution observed with confocal microscopy. [29] (G) Crystal orientation of ice obtained with electron backscatter diffraction in an SEM.[2] The c-axis {0001} and a-axis $\{11\bar{2}0\}$ pole figures for 23 ice crystals sampled in six different domains are plotted.[2] (H) Focused Ion Beam (FIB) milling revealing the cell wall packing. [8] (I) molecular alignment and fibrillar alignment of polymeric scaffolds, in particular, measured with polarized light (optical) microscopy and Raman spectroscopy [127]. These post mortem and in situ techniques, depending on their underlying physics, are best suited to reveal features at particular length scales (centre scale with blue arrows showing their range). The sample size required to obtain valid measurements is usually limited; in X-ray tomography and tomoscopy, for example, the resolution of the detector limits the ratio between the observed volume to the minimum feature size.

Figure 5. ***Quantitative in situ characterization of the structure evolution, features formation and particle arrangements*** [34]. (A) 3D rendered tomograms obtained in situ by X-ray tomoscopy at differesnt times (Aa to Ad) during processing, showing ice crystals in blue, sucrose in red and Kapton® tubes in yellow with a masked out mixed liquid phase to better show the solidification front. (B) Average freezing front progression along the mould height and the corresponding average freezing front velocity over time. (C) Longitudinal, lateral, and thickness growth velocities, as well as volume increase over time, showing the highly anisotropic crystal growth of the ice lamella. (Da–Dc) 3D rendered tomograms of a growing ice lamella at different times showing a lateral angle of 13°. Instabilities form at 150 s (Db). (E) The temporal evolution of the sucrose phase structure from (Ea)130 s to (Eb) 170 s showing the formation and temporal evolution of the 'jellyfish cap' array (Ec). Schematic view of the particle arrangements and orientation evolution of (Fa–Fd) polymeric chains [127] and (Ga-Gd) plate-like particles [8] between the lamellas in the course of crystal growth.

Figure 6. ***Structure-property correlations.*** Anisotropic mechanical, magnetic, and electrical properties of the freeze cast scaffolds. (Aa), (Ab) Distinctly different modulus, yield strength, and toughness are measured in compression parallel to the freezing direction, magnetic field direction and the direction perpendicular to both. (Ac) The geometry of the samples after compression along the three indicated directions. [75] Schematic of the microstructure of the magnetic flake composite freeze cast (B) without and (C) with a magnetic field, and the corresponding quality factor and magnetic permeability magnetic flake composite freeze cast without and with a magnetic field. [75] (D) Four-point probe method to determine the orthotropic electric properties on the axial, parallel, and perpendicular directions of the freeze cast composite.[18]

Figure 7. ***Example sample sectioning schemes for material analysis and mechanical testing aids.*** Examples of standardized sample preparation and testing schemes. (a) A small diameter sample divided into top and a bottom sections to determine structure, mechanical, physical (e.g. electrical conductivity), and functional (e.g. biocompatibility) properties as a function of mould height [28–31,33]. Structural characterisation section reflects structure also of adjacent mechanical and functional testing sections. Mechanical testing section is typically the thickest, structural characterization sections, e.g. for microscopy, may be thin. (b) Delicate samples like thin material films and small diameter rods or tubes benefit from gripping via protective paper frames to prevent premature loading; the frame is cut just before the start of mechanical testing [198]. (c) Protective frame design, 3D printed, aligned with long screws used for small diameter cylindrical scaffolds to hold samples glued into plastic tubes or similar; the screw is removed just before loading.[28] (d)Cutting scheme example for wine-cork sized samples (20 mm diameter, 45 mm height). (e) Layers centred at 7 mm, 17.5 mm, 28 mm sample height divided into 4–5

cubes of 4–5 mm side length for mechanical testing. Correction cuts between the layers ensure height accuracy. Miter box assist razor blade sectioning of 5 mm cubes from a low modulus material.

Box 1 – The Freeze Casting Process

The freeze casting process is fundamentally composed of two steps. The first step is solvent crystal nucleation, which remains comparatively little understood [53,55]., followed by phase separation and directional solidification. The second step is the removal of the solidified solvent, here ice phase, by sublimation during a process termed freeze-drying or lyophilization [5]. Since the second step contributes less to structure formation and more to structure consolidation [214], we will omit it in this Primer.

Phase Separation. During directional solidification the water-based solutions and slurries phase separate into pure ice and a second phase composed of the dissolved polymer(s) and/or suspended particles, which is increasingly upconcentrated between the growing ice crystals[1,2,5,141]. The ice crystals template the second phase in highly dynamic processes, which are complex, because a large number of parameters determine structure and properties of the final freeze-cast material.

Solution or Slurry Composition. Solvent, solute(s), particle size and geometry, and their concentrations and respective material properties from density to surface charges, the pH of the solution[4,5,146], impurities and additives, can affect and/or interact with either the solvent, the solute(s), the particles, the solid-liquid interface, and the ice phase. The components of a materials system must therefore be chosen carefully to achieve the required solvent viscosity, avoid particle agglomeration and sedimentation, and achieve the desired component packing.

Processing Conditions. For a given freeze casting system and mould, the applied cooling rate determines the temperature field and effective local cooling rate.[2] Additionally, the thermal properties of both the mould and the sample material system define solvent nucleation, crystal growth and solvent templating outcomes[56]. Through a careful choice of processing parameters for a particular mould and materials system it is possible to custom-design material properties such as overall porosity, pore size, pore geometry, and cell wall topography and the mechanical and physical performance of the final cellular solid[29,31,53,61,146,151,215].

Experimental observation of and ice crystal growth in 2D and 3D.
Ice crystal growth experiments in 2D in Hele-Shaw cells, which enclose a thin film of material and are pushed through a Bridgman-like thermal gradient to drive directional solidification under well-defined experimental conditions provide first insights into the fundamental science of ice crystal growth. The arrival of 3D tomoscopy now permits to study quantitatively and in considerably less constrained samples the dynamics of ice templating and structure formation.

Additives. With additives, such as sucrose and ethanol, and those that change the pH, the phase transition temperature can be altered, which is reflected in, for example, pore size changes [53]. With antifreeze proteins and compounds with similar effects, such as zirconium acetate, the ice crystal growth direction and also the crystal morphology can be affected significantly [216].

Crystal Growth Simulations. Complementing experimental observations with quantitative 3D phase-field simulations and their implementation for the ice-water system, it is now possible to gain new insights into the mechanisms of that drive material self-assembly and structure formation [21].

Structure-property-processing Correlations to Custom-design Materials. Empirically, over the past 15-20 years, strategies have been developed for the custom-design and manufacture in a single processing step of materials with a hierarchical architecture that spans several length-scales and associated, often novel mechanical and physical properties [7,18,26,31,75,136,217]. Most commonly reported are correlations between applied cooling rate and pore size, typically

determined by collating predominantly "post mortem" 3D structural features, and between pore size and mechanical or physical properties [4,28,136,182,218–220].

Sintering and Carbonization. Freeze-cast ceramics and metals, which after lyophilization, may be considered “green bodies,” are frequently sintered after lyophilization; freeze-cast polymer scaffolds can be further processed by adding a chemical or thermal reduction or carbonization step. How freeze-cast materials sinter, how well their overall shape and structural features such as overall porosity within and between the cell walls, for example, is preserved, depends on parameters such as particle size and geometry, binder type, and freezing rate, to name but three, because these determine how thick the cell walls are and how efficiently the components are packed in them [14].

Box 2 – Tomoscopy

To obtain high quality X-ray tomoscopy results, imaging parameters such as spatial and temporal resolution, the field of view, number of projections, and exposure and experimental time must be set. All of these parameters are interdependent and have a direct influence on the quality of the results so that the most appropriate compromise needs to be found for each sample, and scientific question and goal.

Spatial resolution

Spatial resolution is defined as the smallest distance at which two features can be distinguished and is a quantity which depends strongly on many factors such as the thickness of the scintillator, the beam divergence, the quality of the optical magnification system or the pixel size of the resulting images among others. The latter is considered a guide for the spatial resolution as it is easy to determine, but it is usually 2–5 times lower that the spatial resolution. Typically, microtomography facilities offer spatial resolutions of 0.5–10 μm.

Temporal resolution

As a rough estimate, the time required for a single tomogram (t) should be less than or at least equal to the ratio between the pixel size (x) and the velocity of evolution of the changing event (v) to avoid blurred images and tomograms [35]:

$$t \leq \frac{x}{v}$$

The higher v is, the shorter the exposure time should be for a complete tomogram. The acquisition rate is determined by the number of tomograms acquired per second (tps).

Field of view

The field of view is primarily limited by the beam geometry and the pixel size of the detector system. A reduction of this area in vertical or horizontal direction has a direct influence on the acquired data density and very often also on the acquisition speed, depending on the readout mechanism. In general, reducing the field of view is an effective means of increasing temporal resolution. Typical fields of views are in the range of 1–25 mm^2.

Number of projections

A high number of projections allows for high quality reconstructions, maintaining the requested spatial resolution also at the edges to the tomogram. The number of projections can be reduced if the field of view is reduced, increasing the temporal resolution.

Exposure time

Short exposure times allow higher temporal resolution, but usually at the expense of lower contrast and increasing noise. At high temporal resolutions, not only the exposure time but also the data transfer time becomes more important, and the sum of the two must be minimized.

Experimental time

High-speed CMOS cameras have only a limited amount of internal RAM to storage the immense amounts of data required for tomoscopy with high temporal resolution over a few seconds. Data interfaces are not fast enough for direct storage on hard disks. A special high-end solution is offered by the Gigafrost camera at the Tomcat beamline,[12] which can record hundreds of tomograms per second over minutes.[6]

Glossary

Anisotropy
We observe anisotropy in crystal growth, growth characteristics depend on crystallographic direction. In freeze-cast materials we observe anisotry in structure and properties, which means that in contrast to isotropic materials, in which structure and properties are independent of the direction in which they are measured, the properties vary with direction.

Applied Cooling Rate
The rate at which the temperature decreases per unit time, $\dot{C}$, at the cold source.

Attenuation Coefficient (μ).
A measure of how easily X- rays can penetrate a material, given by the fraction of incident photons in a monoenergetic beam that are attenuated per unit thickness of that material.

Dendritic Ice Crystal Growth
Branched or tree-like crystal growth.

Directional Solidification
Controlled crystal growth in a well-defined direction defined by the applied thermal gradient.

Domain
A volume of solid, akin to a grain, in which ice crystals and templated lamellae exhibit the same orientation and alignment.

Extensional Shear Flow
The 9% volumetric expansion of water upon solidification into ice results in an extensional shear flow. An additional thermal mould contraction can enhance this flow when batch processing. The extensional shear flow contributes to the preferential alignments of components during directional solidification

Field of view (FOV)
Projected area imaged, the FOV corresponds to the region of interest, usually measured in pixels.

Freeze Casting
Directional solidification of solvent-based solutions or slurries, followed by the removal of the solvent in its solid state by sublimation or solvent exchange.

Freezing Front Velocity
The speed of the progression of the solid-liquid interface, in dendritic crystal growth defined by the crystal tip array.

Fully Faceted Crystal Growth
Crystal growth forming atomically or molecularly smooth faces, the facets, whose crystallographic orientations are well defined and characteristic for a compound.

Greyscale
A synonym for the range of voxel values within a slice, volume or tomographic data set.

Hierarchical Pore Architecture
Porosity at different length scales contributed by different levels of the hierarchy; in freeze-cast materials frequently composed of particle porosity, porosity in the cell walls, and porosity defined by the cell walls.

Ice Templating
The shaping of the solute phase by ice the crystals growing from an aqueous solution or slurry.

Instability
A crystal instability forms, when a planar solid-liquid interface is perturbed and a stable array of dendrites starts to form, for example.

Lamellar Spacing
The periodic lamellar spacing defines how coarse or fine the structure of a freeze cast material is. It is defined as $\lambda = S + w$, the sum of the short pore axis, S, and the cell wall thickness, w. The lamellar spacing depends on the local cooling rate.

Local Cooling Rate
The rate at which the temperature decreases per unit time, $\dot{C}_{\mathrm{loc}}$, at a well-defined position within the sample.

Nucleation
Nucleation is the formation of a small cluster (or nucleus) of atoms, once a critical number assemble, crystal growth begins. Homogeneous ice nucleation can occur in the liquid phase, heterogeneous nucleation on the mould bottom surface.

Partially Faceted Crystal Growth
Crystal growth that is faceted in some and non-faceted in other directions.

Phase Contrast
Contrast in a radiograph or tomogram resulting from the difference in phase developed by beams as they pass through an object.

Phase Separation
Two or more phases forming from a single-phase mixture of components.

Pore Size
The pore size is defined by its area, A, the length of the short, S, and long, L, pore axes, their aspect ratio, R, and the cell wall thickness, w.

Principal Component Analysis
Principal component analysis (PCA) is a statistical technique used to analyse the variability of a multi-dimensional dataset. PCA is used to identify the dominant patterns in the data and analyse the 3D spatial orientation of the segmented objects. This is typically done by projecting the voxel coordinates of that object onto a lower-dimensional subspace that captures the most significant variations in the data.

Projections
Radiographs of the object acquired at a given angle of illumination that, when combined with many others, provide the data for numerically reconstructing the object. Typically, between 100 and 3,600 projections are used to reconstruct a tomogram.

Spatial Resolution
The smallest linear distance between two points that can be distinguished in the reconstructed image; usually by a factor of 2-3 larger than the voxel size, depending on the scanned materials and the scanning conditions.

Thermal Gradient
The rate at which the temperature varies per unit distance in a well-defined direction, *G*, a 3D vector.

Tomogram
Originally a two- dimensional (2D) slice through an object reconstructed computationally from a sinogram. Now often used to refer to the 3D reconstructed sample volume.

Tomograms per Second (tps)
Unit for the temporal resolution, with which the recording speed of continuous full tomograms is given in a tomoscopic experiment.

Voxel
The abbreviation for volume element: the basic unit of a three- dimensional digital representation of a volume or object. The voxel size should not be confused with the spatial resolution.

Supplementary Information: Text, Tables, Figures, Videos

[H1] Lyophilization

Once the sample is completely solidified, it is placed in a lyophilizer to remove the ice phase by freeze drying. By converting the ice phase into vapor without first forming a liquid phase, which would happen at ambient conditions, it is possible to preserve the ice-templated sample structure.

Typical freeze-cast samples consist predominantly of the solvent water. The solute and particles that becomes increasingly upconcentrated in the interdendritic spaces possesses a freezing temperature lower than that of water. This means that samples may appear to be fully frozen when the second solute-rich phase has not yet reached its phase transition temperature. Only when also this second phase, a eutectic, has reached its eutectic temperature, is the sample fully solidified. When the solute or one of its components is a polymer that upon upconcentration becomes increasingly viscous and finally undergoes a glass transition, the fully solidified state is reached when the second phase is vitrified. For the freeze-drying process to be successful, it is critical that the sample placed in the lyophilizer has a temperature below the eutectic or glass transition temperature, whichever applies.

Lyophilization is a two-step process that starts with primary and concludes with secondary drying. For the primary drying step, in which the water phase is removed by sublimation, the rate of sublimation is determined by the difference in vapor pressure between the sample and the ice collector, which determines how quickly the water molecules migrate from the higher to the lower vapor pressure site. Because the vapor pressure increases with increasing temperature, this means that the temperature of the sample must be higher than the temperature of the ice collector while keeping the sample temperature below its eutectic or glass transition temperature.

To fulfill both the temperature and the vapor pressure requirements for freeze drying, lyophilizers possess a cold trap that serves as ice collector and a vacuum pump to lower the pressure. The temperature of the cold trap should be at least 20 °C cooler than the eutectic or glass transition temperature. Commercial lyophilizers typically offer temperatures in the three ranges of -50 °C to – 55 °C and -75 °C to -85 °C, and -105 °C. The condenser temperature determines which solute compositions can be dried and which gases can be trapped; all gases that are not collected on the condenser, because the temperature of the condenser is too high, enter the vacuum pump, which should therefore be protected by its own trap. The vacuum pump lowers the pressure within the lyophilizer and must at all times be kept lower than the ice vapor pressure of the sample to prevent sample melting. Because an increase in sample temperature has a greater effect on the vapor pressure differential than lowering the ice collector temperature, the sample temperature is of particular importance as a control parameter and must be carefully controlled to prevent melting.

Two types of lyophilizers are commonly used: manifold lyophilizers (Figure S7A) and shelf lyophilizers (Figure S7B). The first type is a manifold lyophilizer with constant heat and vacuum applied. To freeze dry, the sample is placed in flask that has at least two to three times the volume of the sample. The sample temperature should be at least 20 °C below the eutectic or glass transition temperature of the sample, and the vacuum should be applied swiftly to the flask. To prevent sample melting due to contact with the flask walls, samples can be loosely held in tissue paper or a wide-open container that serves as spacer but does not compromise the vacuum to be pulled. The vaccum is applied when the flask is individually connected via a nozzle and valve to the lyophilizer's drying chamber port. In the manifold lyophilizer, the sample vapor pressure is increased by the heat applied by the ambient room temperature, while the vacuum is kept as low as possible, typically 0.008 mbar; the resulting evaporative cooling prevents the sample from melting. Advantages of the manifold freeze dryer are that the close proximity to the

ice collector maximizes drying efficiency, and that several different samples can be dried at the same time and removed separately.

The second type of a lyophilizer is a shelf lyophilizers, in which the sample is placed on a temperature-controlled shelf within the vacuum chamber, whose pressure is varied in parallel to the shelf and the ice collector temperatures to optimize drying efficiency. The ideal is to freeze dry the sample slightly below its eutectic or glass transition temperature, because the lower vapor pressure at a lower temperature would require also a lower ice collector temperature and prolong the drying process.

Primary drying of the sample begins, when sample temperature and chamber pressure correspond to the sublimation conditions defined by the sublimation line on the pressure-temperature phase diagram (Figure S7C, [221]). The fully solidified samples cooled to a temperature at least 20 °C their eutectic or glass transition point (Point A) are placed in the flask or on the drying shelf. The sample temperature is raised but kept below this sample specific critical temperature (Point B) while the pressure is reduced to reach the sublimation line, which marks the conditions at which sublimation and with it the first lyophilization step starts. To increase the vapor pressure differential further, a higher vacuum is applied (Point C) and the ice collector temperature lowered (Point D) .

Secondary drying starts, once the pure ice phase has been removed completely. At this point the sample may appear dry, but the solute that forms the cell walls of the cellular solid may still contain bound water (frequently 5-8%). Isothermal desorption is the process by which this remaining moisture is removed. In shelf lyophilizers, in which the sample temperature can be elevated, the desorption process is typically performed at higher than ambient temperature while keeping pressure and collector temperature as low as possible. In manifold lyophiliers, pressure and sample and collector temperature remain the same. This secondary drying step typically takes up to one third of the overall drying time. A typical freeze-drying cycle for samples lyophilized in a shelf lyophilizer is depicted in Figure S7D, [221]).

Sample drying starts at the surface of the sample and decreases in efficiency the further the drying front moves towards the sample core. This is because the water vapor must pass through an increasing amount of dry sample material. How easily the water molecules move through the sample is thus not only determined by the sample composition but also affected by the initial ice crystal size: the larger they were, the larger the pores revealed during drying, and the easier the water molecule can progress, thus the faster the drying.

An adjustment to the freezing and lyophilization parameters or cycle might be required when, for example, purely polymeric samples exhibit an hourglass rather than a regular cylindrical wine-cork-like shape after lyophilization, or cracks form in green bodies freeze-cast from ceramic or metals slurries. Such artifacts can occur, when residual moisture is retained in the polymer phase of the sample, which then acts as a plasticizer permitting plastic sample deformation to occur when the vacuum is acting on it. Reasons for retained moisture tend do be incomplete freezing or incomplete drying of the solute phase. Also too high a temperature applied during the lyophilzation process, can lead to deformation and sample damage.

Finally, when the solute can, like for example sucrose, undergo structural changes during the drying process, a phenomenon known as collapse may occur, even when the sample was being fully solidified and the temperature kept well below it glass transition temperature. This structural collapse occurs at the boundary of the drying front, when the sample is warmed during the freeze drying process. Collapse can be prevented by keeping the sample temperature below the collapse temperature of the solute phase during primary drying. To give an example, the collapse temperature for freeze-concentrated aqueous sucrose solutions is -32 °C.

Figure Captions

Figure S1. (Aa) Transverse cross secton of still frozen ice-polymer composite with ice-templated polymer ridges.[2] (Ab-d) Chitosan scaffold exhibiting the unilateral cell wall surface features 1-5 defined in Figure 1A.[21]. (Ba, Bb) Slurries containing fibrillar components for pillars and bridges between fibre mat-like cell walls.[29,31] (Ca-Cd) Particles more or less efficiently packed, depending on particle size distribution and shape.[7](Cd) Platelets or flakes assembled into a nacre-like structure[8].

Figure S2. (a) Equipping the mould with thermocouples just underneath the inner surface, for example, fundamental processing parameters such as the local thermal gradients, G, local cooling rates, $\dot{C}$, and the freezing front velocity, v, can be determined [7,21]. (b) A thermally conducting mould wall made from, for example, copper or alumina, in contact with the cold source and sealed by a thermally insulating mould bottom, creates a radial thermal gradient. [29,222] (c) Enclosing the sample in a thermally conducting container and applying identical cooling rates on all sides, e.g. by dropping the mould into liquid nitrogen, or placing it in a freezer, results in directional crystal growth towards the sample centre; sample properties can include a negative Poisson's ratio. [72,73] (d) An externally applied magnetic field (B-field), generated either by a permanent magnet or Helmholtz coils, determine particle orientation and distribution of magnetic and surface magnetized materials: a non-uniform B-field results in both particle rotation and translation.[13] (e) An externally applied electric field affects ice crystal growth and orientation.[76,77,213] (f) Standing waves within the mould, generated by ultrasound, for example, affect particle mobility during solidification and thereby particle packing in the final product.[78]

Figure S3. Typical systems for continuous freeze casting generate: (a) droplets and spherical particles, thus 0D structures with radial porosity created when the solution or slurry is sprayed or electrosprayed [81] into a cold bath or chilled air [70,71]. (b) Fibres, rods and tubes, thus 1D structures are formed, when the solution or slurry flows or is extruded through a cold zone; here, the cold zone shape, temperature gradients, and flow rate determine pore size and orientation [26]. (c) Freeze-cast sheets, thus 2D structures are formed, when solution or slurry films are passed through a cold zone; also here, cold zone shape, temperature gradients, and flow rate determine pore size and orientation [82,87]. (d) Spraying solutions or slurries on an existing scaffolds in a cold environment, additional tubular scaffold layers can be created [70,71]. (e) Complex 3D material architectures can be created by 3D freeze printing [27,223].

Figure S4. ***2D In Situ Freezing Stage***. A thin layer of an aqueous solution or slurry is sandwiched between two glass slides or in a glass capillary (Hele-Shaw Cell). A defined thermal gradient is created between the two temperature zones through which the Hele-Shaw cell is moved at a controlled velocity achieving a well defined cooling rate. The freezing behavior in 2D is imaged under an optical microscope, or confocal microscopy.

Figure S5. ***Processing-structure correlations.*** Micrographs of fully hydrated and dry scaffolds obtained with (A) confocal microscopy and (B) SEM allow quantification of pore sizes, in particular, short and long pore axes, and pore area.[33] Robust processing-structure correlations between (Ca) long and (Cb) short pore axes and applied cooling rate. [28] (D) Domain size and orientation distribution of the pores analyzed and color coded.[66] (Da) Multidominal structure created by freeze casting under single thermal gradient. (Db) Single domanial structure generated by freeze casting under dual thermal gradients.

Figure S6. Mechanical Anisotropy – Gibson-Ashby Scaling Laws. (A) Two types of cellular solids are compared: foams, in which the pores are more or less equiaxed, and honeycombs, in which the pores are unidirectional and aligned. The graphs illustrate how the modulus and strength of foams and honeycombs scale as a function of relative density, which is the density of

the foam, ρ^*, divided by the density of the solid, ρ_s, from which it is made. (B) Plotting the modulus of freeze cast alumina ceramics freeze cast from spherical and platelet-like particles and magnetic Sendust flakes freeze cast in the absence and the presence of an externally applied field versus their respective relative densities, illustrates how significant structural optimization is for improved material performance.

Figure S7. Lyophilization. (A) Schematic of a manifold lyophilizer, illustrating how flasks are attached to a port of the vacuum chamber which contains the cold trap (ice collector). (B) Schematic of a shelf lyophilizer. (C) A typical phase diagram illustrating the freeze drying process. The fully solidified sample at a temperature at least 20 °C below its eutectic or glass transition point (Point A) is placed in the flask or on the drying shelf. The sample temperature is raised but kept below this sample specific critical temperature (Point B) while the pressure is reduced to reach the sublimation line, which marks the conditions at which sublimation and with it the first lyophilization step starts. To increase the vapor pressure differential further, a higher vacuum is applied (C) and the ice collector temperature lowered (D) .
(D) A typical freeze-drying cycle for samples lyophilized in a shelf lyophilizer is depicted in Figure 7D.

Video Captions

Video S1. ***Unidirectional solidification of a cylindrical freeze cast specimen***
Shown is the unidirectional solidification of a section of the cylindrical sample in a 2 mm diameter polyimide tube observed for 267 seconds. The video illustrates the dynamics of crystal growth and solution templating during freeze casting. The solidified ice crystals are shown in blue and the ice-templated sucrose phase in yellow. The solidification front advances with an average velocity of ~11 μm/s. Domains are defined by differences in lamellar orientation. The process was imaged at one tomoscopy per second. The video plays at 10 frames per second.

Video S2. ***Growth of an extracted single ice lamella***
The video shows the crystal growth of a single ice lamella from one of the central domains in a unidirectionally solidifying 3% w/v sucrose in water solution. In the 267 seconds shown, different types of secondary instabilities form unilaterally on the side of the ice lamella, which faces the cold end of the mould; noteworthy is the sometimes transient nature of the instabilities. The lamella expands in thickness and width with increasing height due to a decrease in the local cooling rate. The slight directional changes at about t = 70 s and t = 150 s from 4.4° to 10°, respectively, is paralleled by the formation of secondary instabilities and the lamella splitting into two. The video plays at 10 frames per second.

Video S3. ***Evolution of ice-templated structure.***
The video shows the structural evolution of the ice-templated sucrose lamella for 160 s. Noteworthy is that the progressing freezing front pushes surface features, in this case a "jellyfish cap" array along with it parallel to the direction of solidification. Also show is the formation of first attached, then detached "tentacle"-like features, whose structural development is detailed in Video S4 at higher magnification. The video plays at 9 frames per second.

Video S4. ***Formation of a "Jellyfish Cap" Array with "Tentacles"***
Shown in this video at high magnification is the formation over 30 s of first attached, then detached 'tentacle'-like surface features extending from the 'jellyfish cap' array parallel to the freezing direction. The video plays at 10 frames per second.

Fig. 1: Schematic of the freeze casting process and examples of structural features templated in freeze-cast polymers, ceramics and metals.

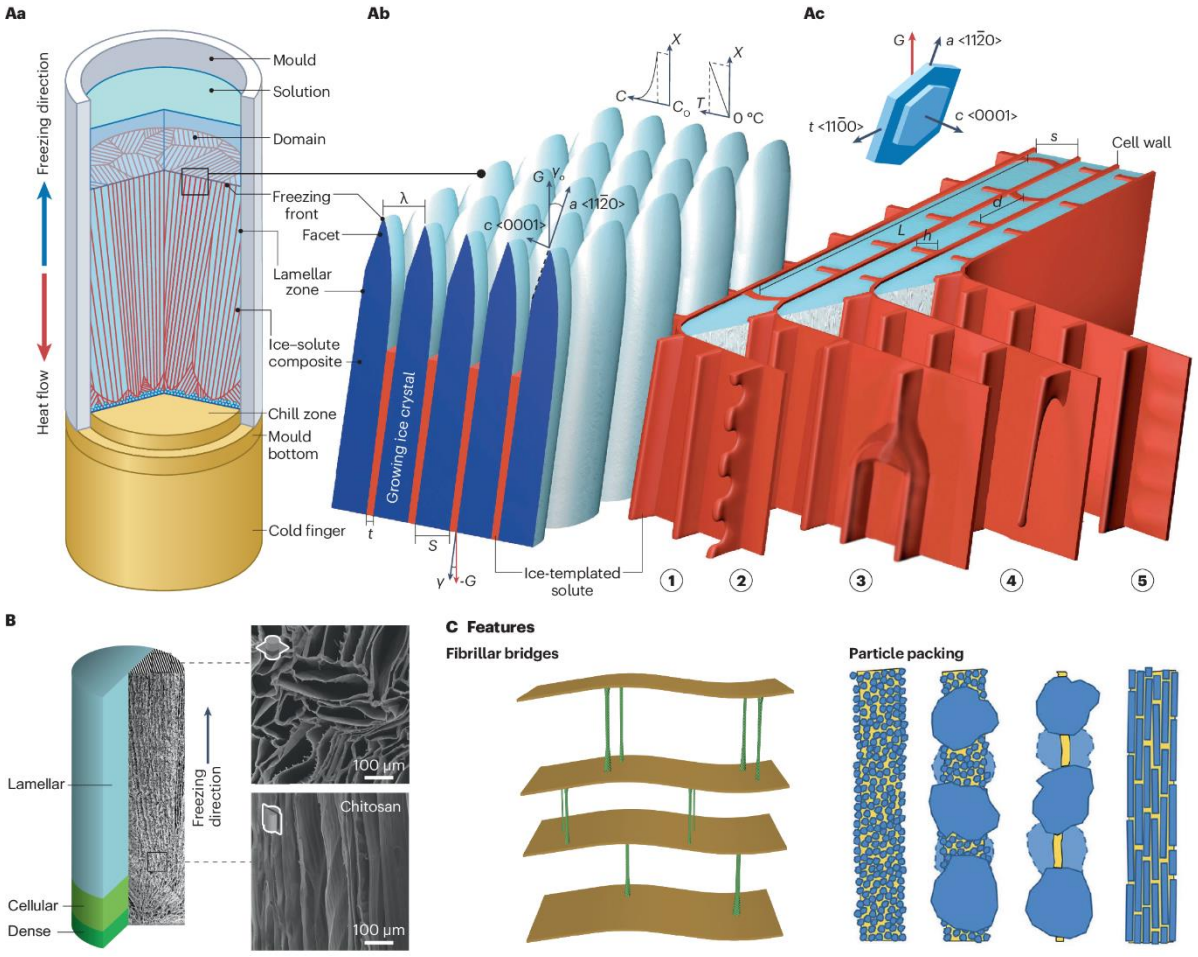

Fig. 2: An overview of freeze caster, mould designs, resulting domain shape and lamellar orientation in two and three dimensions.

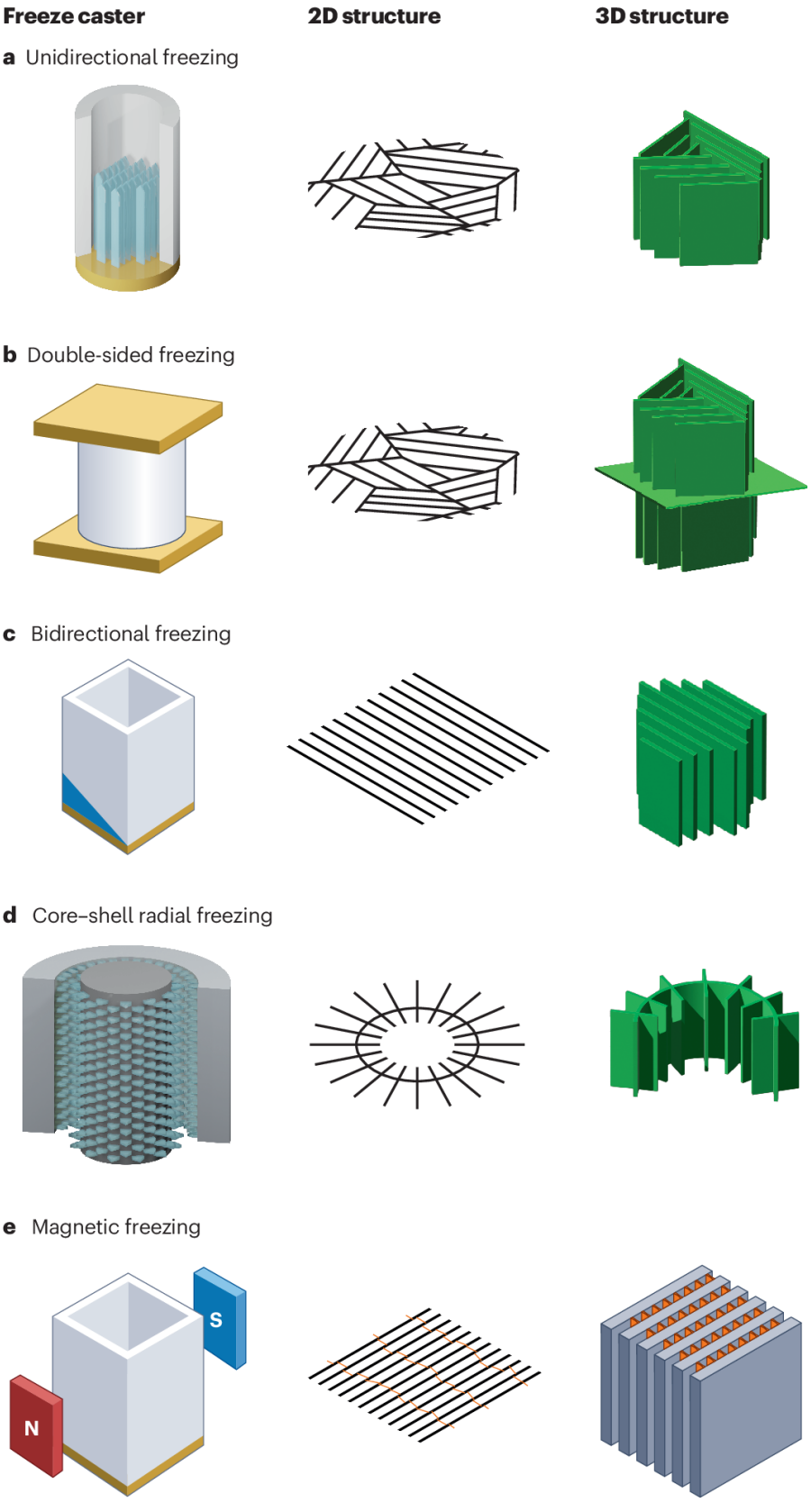

Fig. 3: Dynamic structural characterization of crystal growth processes with tomoscopy.

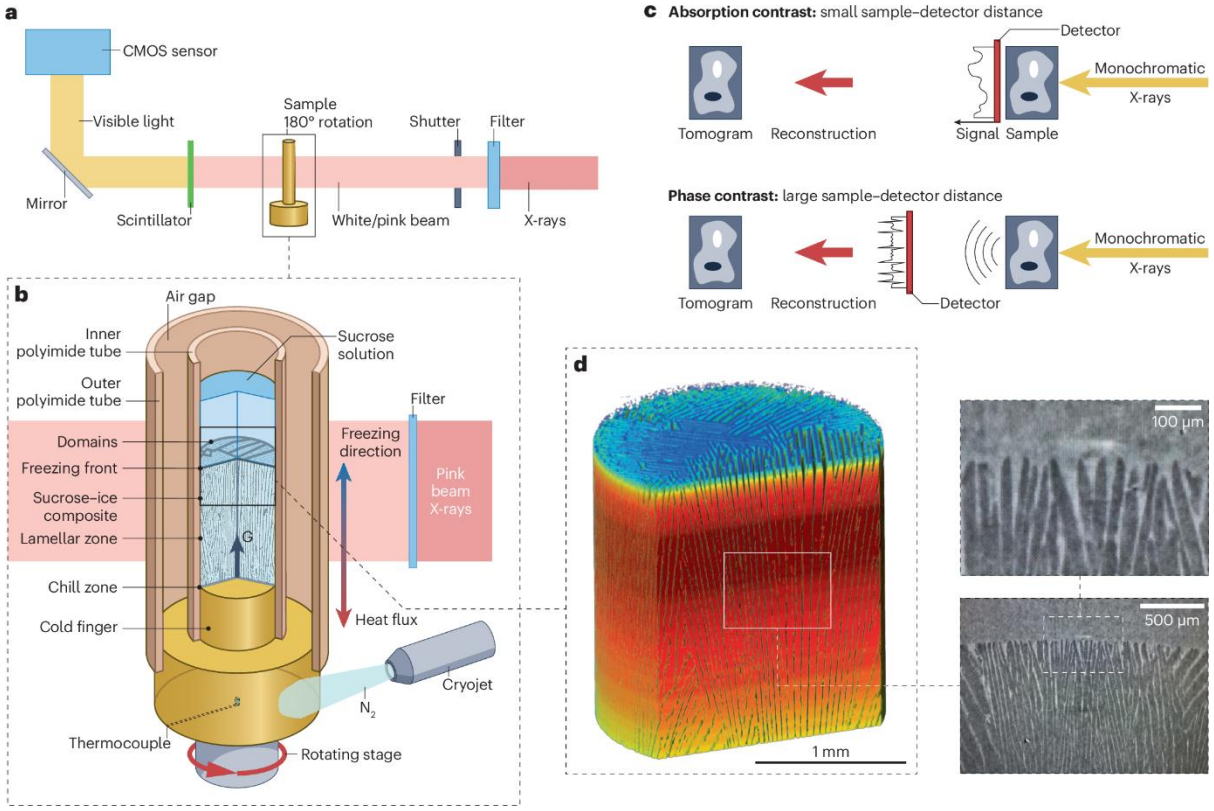

Fig. 4: Overview of in situ and post-mortem techniques to characterize the dynamics of ice crystal growth and ice templating during solidification and the hierarchical material architecture that results ordered by length scale.

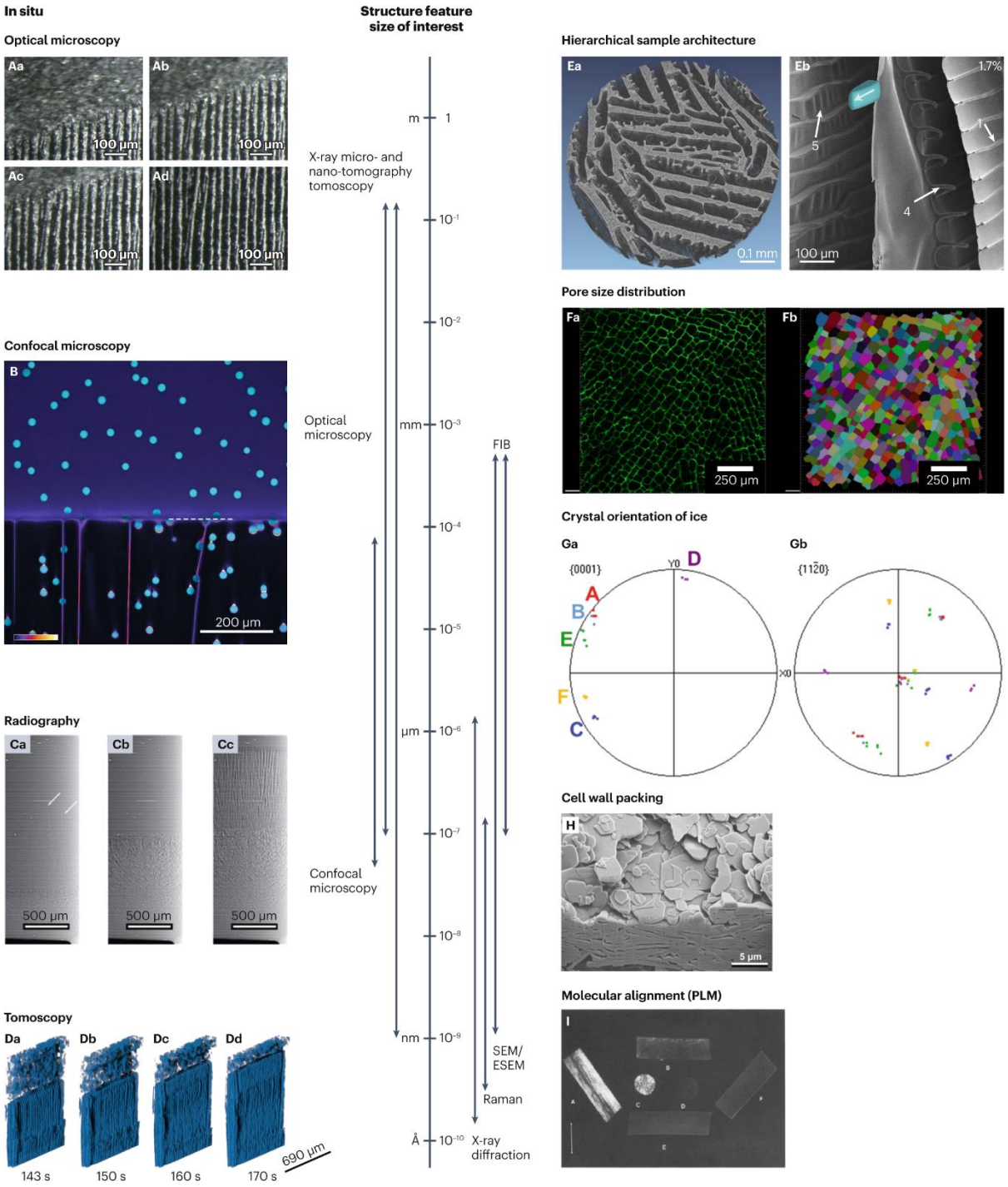

Fig. 5: Quantitative in situ characterization of the structure evolution, features formation and particle arrangements.

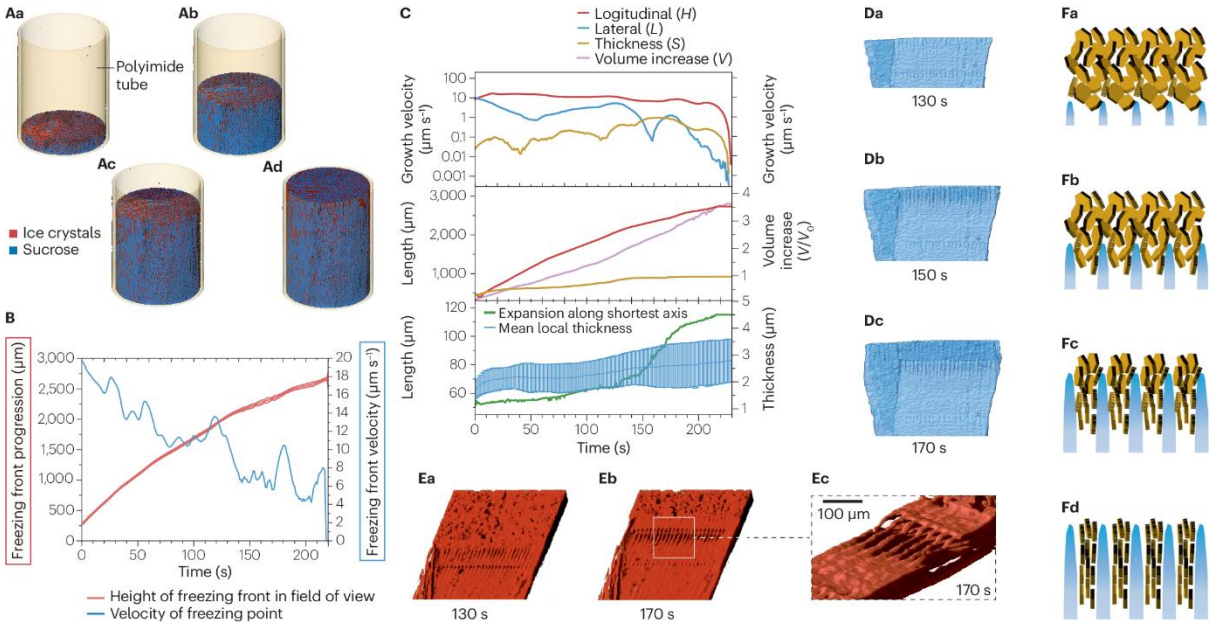

Fig. 6: Structure–property correlations.

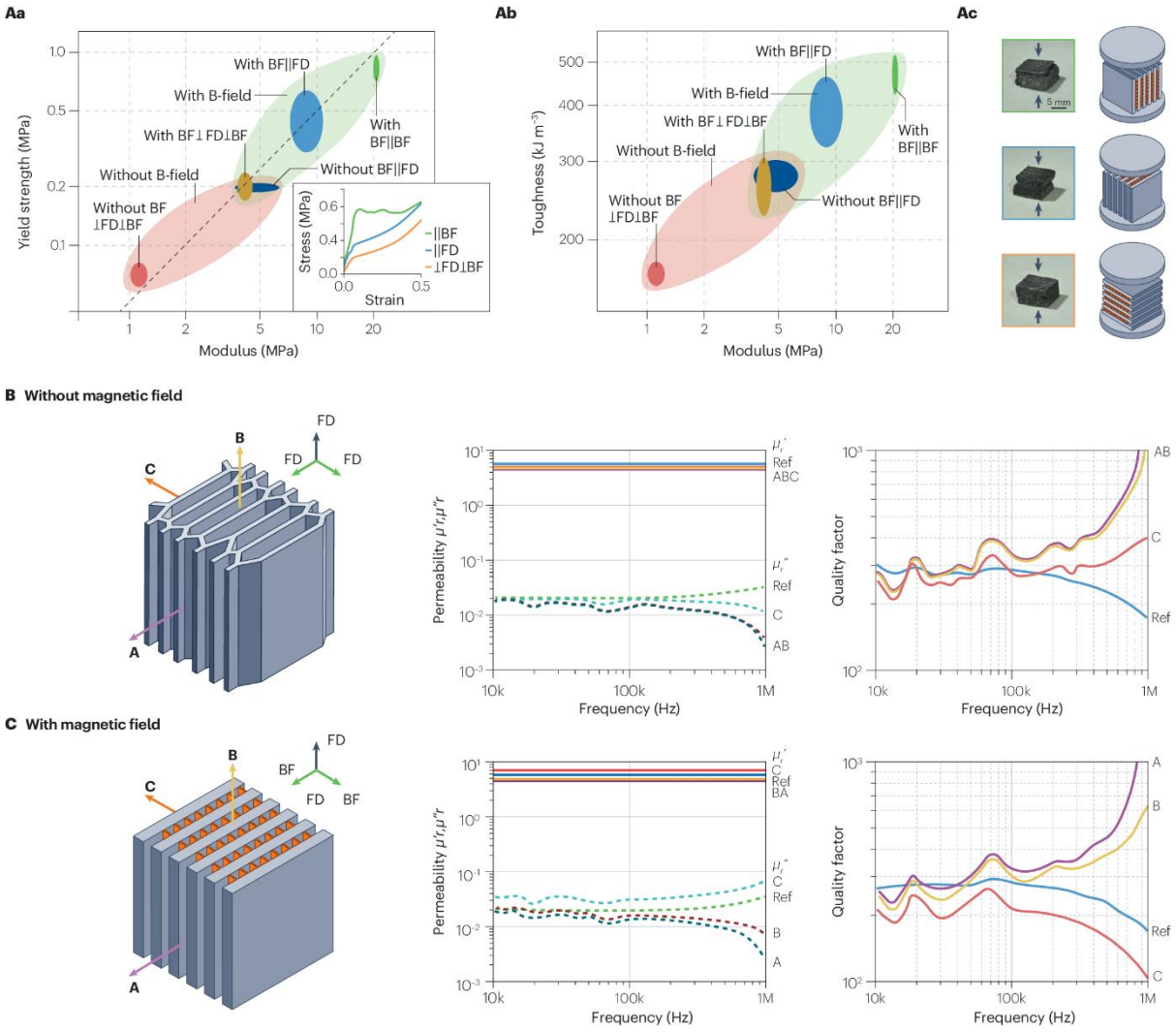

Fig. 7: Example sample sectioning schemes for material analysis and mechanical testing.

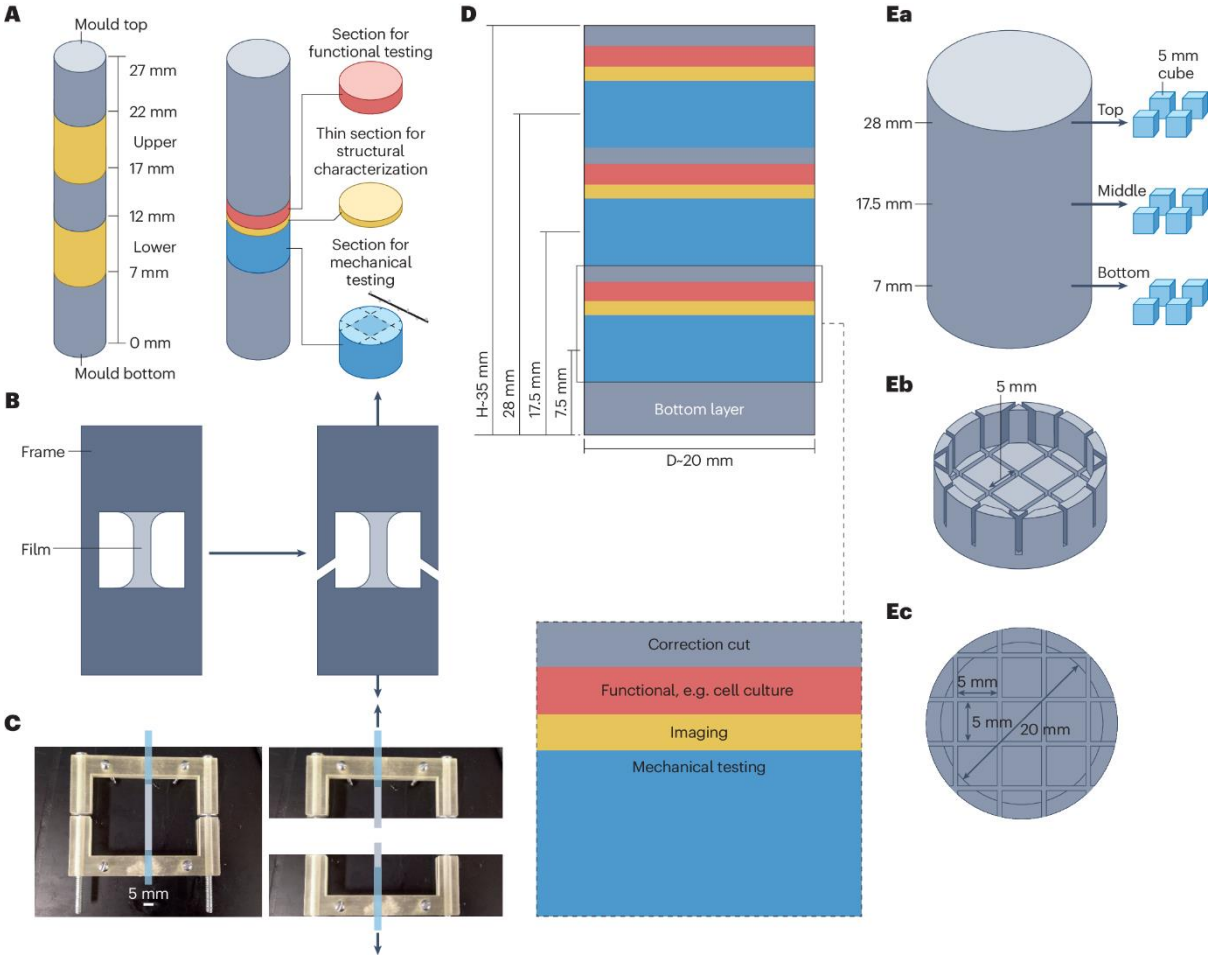

Supplementary Information

Freeze Casting

Ulrike G. K. Wegst,[1,2,†], Paul H. Kamm[2,3,5], Kaiyang Yin[4,5], Francisco García-Moreno[2,3,†]

[1] Biomimetic Design Laboratory, Department of Physics,
Northeastern University, Boston, MA, USA
[2] Process Imaging Laboratory, Institute of Materials Science and Technology,
Technische Universität Berlin, Berlin, Germany
[3] Process Imaging Laboratory, Institute of Applied Materials,
Helmholtz-Zentrum Berlin für Materialien und Energie, Berlin, Germany
[4] Laboratory of Micro and Materials Mechanics, Department of Microsystems Engineering,
University of Freiburg, Freiburg, Germany
[5] These authors contributed equally: Paul H. Kamm, Kaiyang Yin

[†]email: ulrike.wegst@northeastern.edu, garcia-moreno@helmholtz-berlin.de

Supplementary Note 1 - Lyophilization

Once the freeze-cast sample is completely solidified, it is placed in a lyophilizer (Figures S6A, B) to remove the ice phase by freeze drying. By converting the ice phase into vapor without first forming a liquid phase, which would happen at ambient conditions, it is possible to preserve the ice-templated sample structure. Typical freeze-cast samples consist predominantly of the solvent water. The solute and particles that become increasingly upconcentrated in the interdendritic spaces possess a freezing temperature lower than that of water.[1,2] This means that samples may appear to be fully frozen when the second solute-rich phase has not yet reached its phase transition temperature. Only when also this second phase, a eutectic, has reached its eutectic temperature, is the sample fully solidified.[3,4] When the solute or one of its components is a polymer that, upon upconcentration, becomes increasingly viscous and finally undergoes a glass transition, the fully solidified state is reached when the second phase is vitrified.[5] For the freeze-drying process to be successful, it is critical that the sample placed in the lyophilizer has a temperature below the eutectic or glass transition temperature, whichever applies.[3,4]

Lyophilization is a two-step process that starts with primary and concludes with secondary drying (Figures SC,D).[3,4] For the primary drying step, in which the water phase is removed by sublimation, the rate of sublimation is determined by the difference in vapor pressure between the sample and the ice collector, which determines how quickly the water molecules migrate from the higher to the lower vapor pressure site.[3,4] Because the vapor pressure increases with increasing temperature, this means that the temperature of the sample must be higher than the temperature of the ice collector, while keeping the sample temperature below its eutectic or glass transition temperature.[3,4]

To fulfil both the temperature and the vapor pressure requirements for freeze drying, lyophilizers possess a cold trap that serves as ice collector and a vacuum pump to lower the pressure.[3,4] The temperature of the cold trap should be at least 20 °C cooler than the eutectic or glass transition temperature.[3] Commercial lyophilizers typically offer temperatures in the three ranges of -50 °C to -55 °C, -75 °C to -85 °C, and -105 °C.[3,4] The condenser temperature determines which solute compositions can be dried and which gases can be trapped. All gases that are not collected on the condenser, because the temperature of the condenser is too high, enter the vacuum pump, which should therefore be protected by its own trap.[3,4] The vacuum pump lowers the pressure within the lyophilizer and must at all times be kept lower than the ice vapor pressure of the sample to prevent sample melting.[3,4] Because an increase in sample temperature has a greater effect on the vapor pressure differential than lowering the ice collector temperature, the sample temperature is of particular importance as a control parameter and must be carefully controlled to prevent melting.[3,4]

Two types of lyophilizers are commonly used: manifold lyophilizers (Figure S6A) and shelf lyophilizers (Figure S6B).[3,4] The first type is a manifold lyophilizer with constant heat and vacuum applied.[3,4] To freeze dry, the sample is placed in a flask that has at least two to three times the volume of the sample. The sample temperature should be at least 20 °C below the eutectic or glass transition temperature of the sample, and the vacuum should be applied swiftly to the flask.[3,4] To prevent sample melting due to contact with the flask walls, samples can be loosely held in tissue paper or a wide-open container that serves as spacer but does not compromise the vacuum to be pulled. The vacuum is applied when the flask is individually connected via a nozzle and the valve to the lyophilizer's drying chamber port is opened.[3,4] In the manifold lyophilizer, the sample vapor pressure is increased by the heat applied by the ambient room temperature, while the vacuum is kept as low as possible. A vacuum of at least 0.13 mbar is required, typically, values down to 0.008 mbar are achieved.[3,4] The resulting evaporative cooling prevents the sample from melting.[3,4] Advantages of the manifold freeze

dryer are that the close proximity to the ice collector maximizes drying efficiency, and that several different samples can be dried at the same time and removed separately.

The second type of a lyophilizer is a shelf lyophilizers, in which the sample is placed on a temperature-controlled shelf within the vacuum chamber, whose pressure is varied in parallel to the shelf and the ice collector temperatures to optimize drying efficiency.[3,4] The ideal is to freeze dry the sample slightly below its eutectic or glass transition temperature, because the lower vapor pressure at a lower temperature would require also a lower ice collector temperature and prolong the drying process.[3,4]

Primary drying of the sample begins, when sample temperature and chamber pressure correspond to the sublimation conditions defined by the sublimation line on the pressure-temperature phase diagram (Figure S6C).[3,4] The fully solidified samples, cooled to a temperature at least 20 °C below their eutectic or glass transition point (Point 1), are placed in the flask or on the drying shelf. The sample temperature is raised but kept below this sample specific critical temperature (Point 2) while the pressure is reduced to reach the sublimation line, which marks the conditions at which sublimation and with it the first lyophilization step starts.[3,4] To increase the vapor pressure differential further, a higher vacuum is applied (Point 3) and the ice collector temperature lowered (Point 4).[3,4]

Secondary drying starts once the pure ice phase has been removed completely. At this point, the sample may appear dry but the solute that forms the cell walls of the cellular solid may still contain bound water (frequently 5-8%). Isothermal desorption is the process by which this remaining moisture is removed.[3,4] In shelf lyophilizers, in which the sample temperature can be elevated, the desorption process is typically performed at higher than ambient temperature while keeping pressure and collector temperature as low as possible.[3,4] In manifold lyophilizers, pressure and sample and collector temperature remain the same.[3,4] This secondary drying step typically takes up to one third of the overall drying time. A typical freeze-drying cycle for samples lyophilized in a shelf lyophilizer is depicted in Figure S6D.[3,4]

Sample drying starts at the surface of the sample and decreases in efficiency the further the drying front moves towards the sample core.[3,4] This is because the water vapor must pass through an increasing amount of dry sample material. How easily the water molecules move through the sample is thus not only determined by the sample composition but also affected by the initial ice crystal size: the larger they were, the larger are the pores revealed during drying, and the easier the water molecule can progress, thus the faster the drying.[3,4]

An adjustment to the freezing and lyophilization parameters or cycle might be required when, for example, purely polymeric samples exhibit an hourglass rather than a regular cylindrical wine-cork-like shape after lyophilization, or cracks form in green bodies freeze-cast from ceramic or metals slurries.[3,4,6] Such artifacts can occur, when residual moisture is retained in the polymer phase of the sample, which then acts as a plasticizer permitting plastic sample deformation to occur when the vacuum is acting on it.[3,4,6] Reasons for retained moisture tend to be incomplete freezing or incomplete drying of the solute phase. Also too high a temperature applied during the lyophilization processs can lead to deformation and sample damage.[3,4]

Finally, when a solute can undergo structural changes during the drying process, like sucrose, for example, a phenomenon known as collapse may occur, even when the sample was fully solidified and the temperature kept well below it glass transition temperature.[3] This structural collapse occurs at the boundary of the drying front, when the sample is warmed during the freeze-drying process.[3] Collapse can be prevented by keeping the sample temperature below the collapse temperature of the solute phase during primary drying.[3] To give an example, the collapse temperature for freeze-concentrated aqueous sucrose solutions is -32 °C.[3]

Figure S1

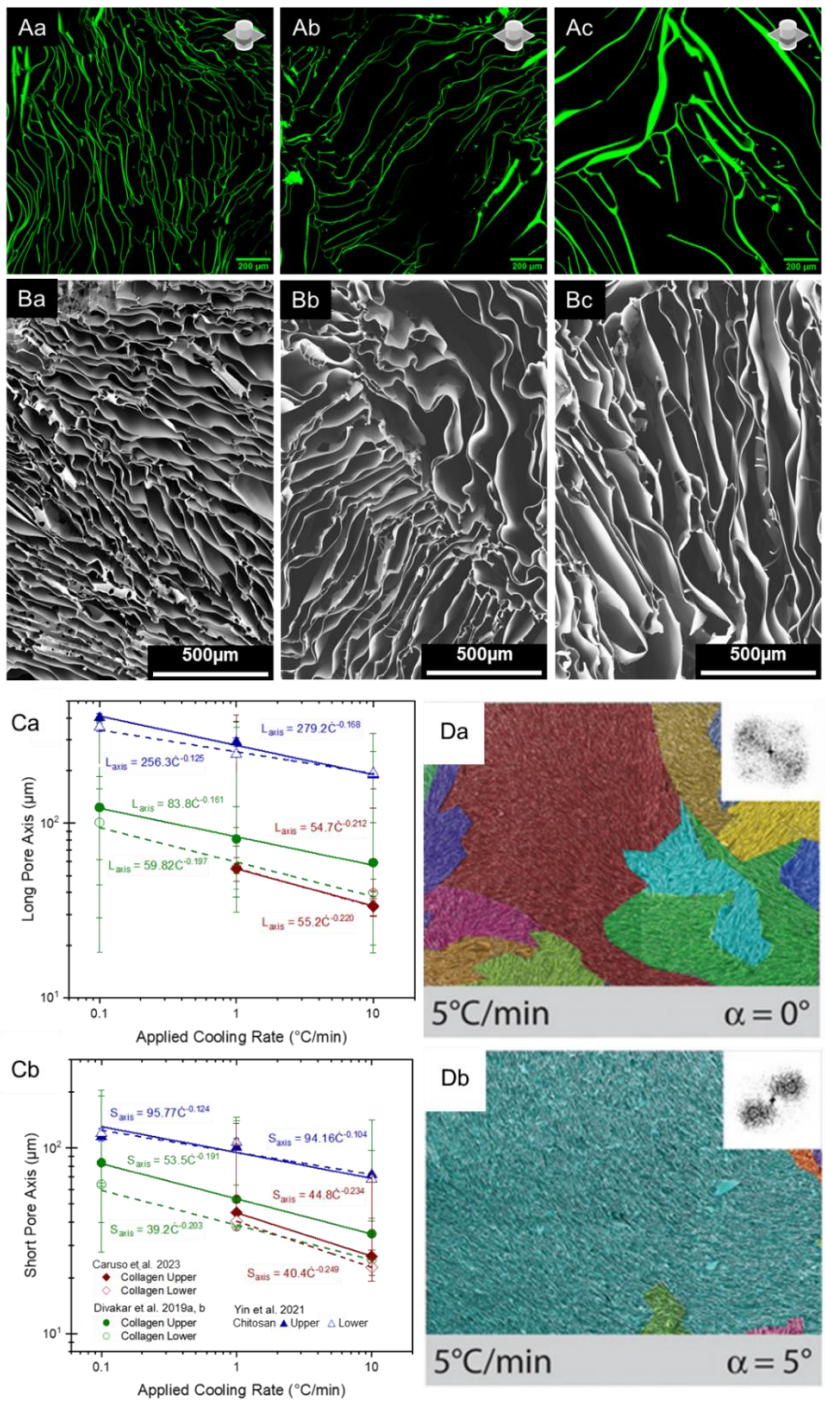

Processing-structure correlations. Micrographs of fully hydrated and dry scaffolds obtained with **(A)** confocal and **(B)** scanning electron microscopy allow quantification of pore sizes, in particular, short and long pore axes, and pore area.[7]

Samples prepared with applied cooling rates of **(Aa, Ba)** 10 °C/min, **(Ab, Bb)** 1 °C/min, **(Ac, Bc)** 0.1 °C/min. Robust processing-structure correlations between **(Ca)** long, *L*, and **(Cb)** short, *S*, pore axes and the applied cooling rate, $\dot{C}$.[8]

(D) Domain size and orientation distribution of the pores analyzed and color coded.[9]

(Da) Multidominal structure created by freeze casting under single thermal gradient. **(Db)** Single domain structure generated by freeze casting with a dual thermal gradient created with an insulating wedge placed in the mould.

Figure S2

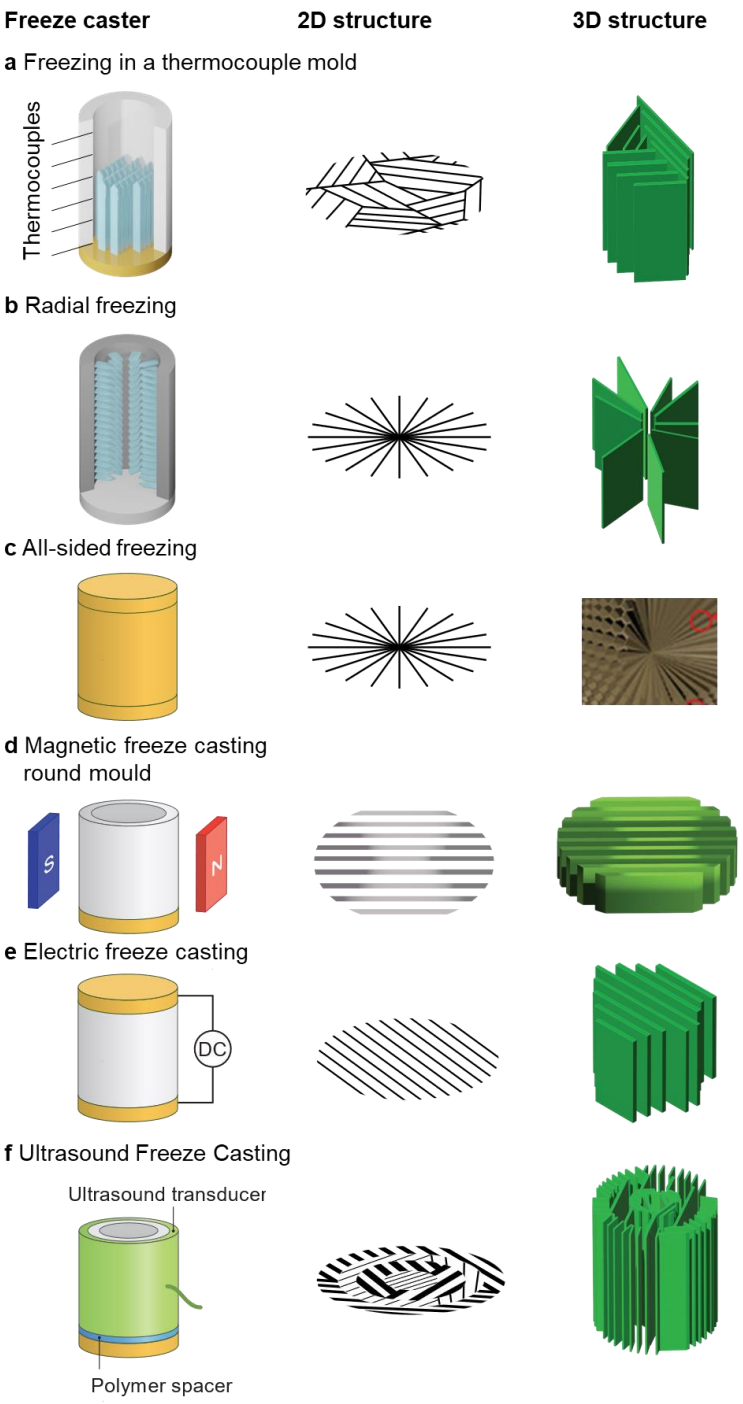

Mould Designs. (a) Equipping the mould with thermocouples just underneath the inner surface, for example, fundamental processing parameters such as the local thermal gradients, G, local cooling rates, $\dot{C}$, and the freezing front velocity, V, can be determined.2,10. (b) A thermally conducting mould wall made from, for example, copper or alumina, in contact with the cold source and sealed by a thermally insulating mould bottom, creates a radial thermal gradient.11,12 (c) Enclosing the sample in a thermally conducting container and applying identical cooling rates on all sides, e.g. by dropping the mould into liquid nitrogen, or placing it in a freezer, results in directional crystal growth towards the sample centre; sample properties can include a negative Poisson's ratio.13,14 (d) An externally applied magnetic field (B-field), generated either by a permanent magnet or Helmholtz coils, determine particle orientation and distribution of magnetic and surface magnetized materials: a non-uniform B-field results in both particle rotation and translation.15 (e) A during solidification externally applied electric field affects ice crystal growth and orientation.16–18 (f) Standing waves within the mould, generated by ultrasound, for example, affect particle mobility during solidification and thereby particle packing in the final product.19 Part a (left) reprinted with permission from ref 12, Elsevier. Part a (middle), b (middle), c (middle), d (left), e (left), e (middle), f (left) and f (middle) adapted with permission from ref 34, Wiley. Part d (middle) adapted with permission from ref 35, Wiley. Reprinted (adapted) with permission from

Figure S3

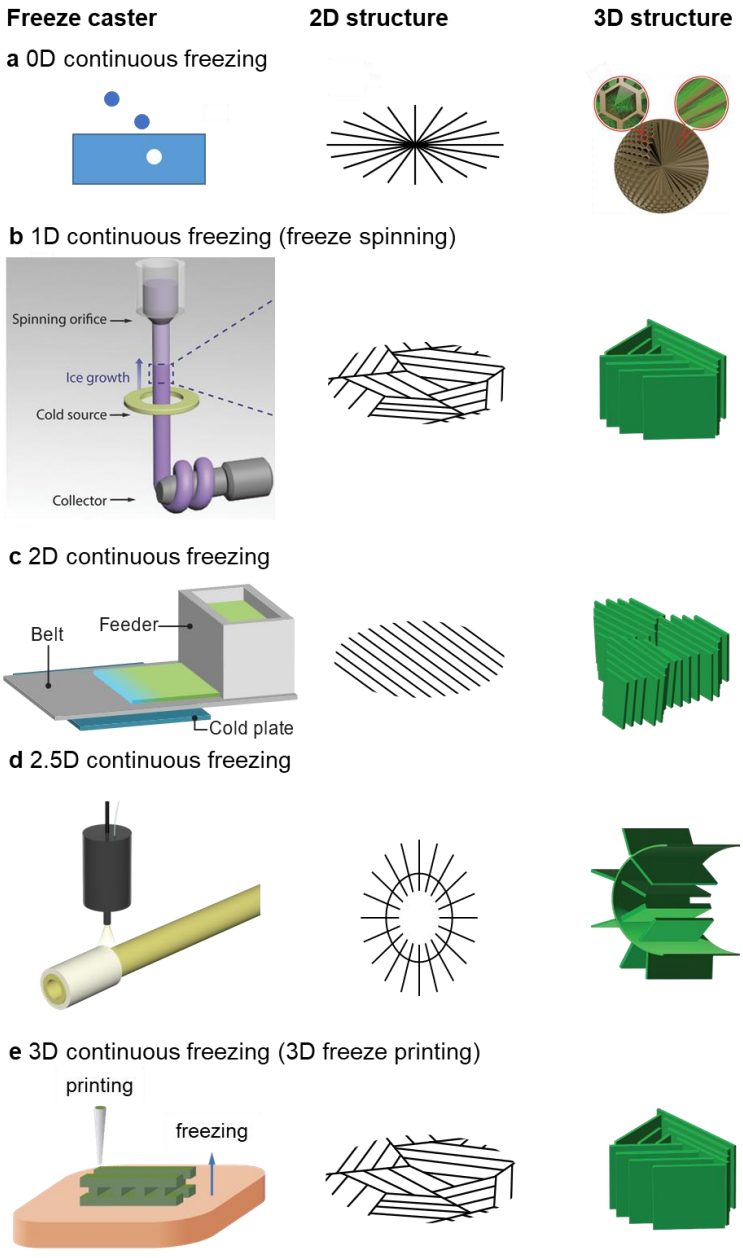

Continuous Freeze Casting. Typical systems for continuous freeze casting generate: (a) droplets and spherical particles, thus 0D structures with radial porosity created when the solution or slurry is sprayed into a cold bath or chilled air.20–22 (b) Fibres, rods and tubes, thus 1D structures are formed, when the solution or slurry flows or is extruded through a cold zone; here, the cold zone shape, temperature gradients, and flow rate determine pore size and orientation.23 (c) Freeze-cast sheets, thus 2D structures are formed, when solution or slurry films are passed through a cold zone; also here, cold zone shape, temperature gradients, and flow rate determine pore size and orientation.24,25 (d) Spraying solutions or slurries on an existing scaffolds in a cold environment, additional tubular scaffold layers can be created.20,21 (e) Complex 3D material architectures can be created by 3D freeze printing.26,27 Part a (middle) adapted with permission from ref 34, Wiley. Reprinted (adapted) with permission from ref 22, American Chemical Society. Part b (left) reprinted with permission from ref 23, Wiley. Part b (middle), c (middle), d (middle) and e (middle) reprinted with permission from ref 34, Wiley. Reprinted (adapted) with permission from ref 25, American Chemical Society. Part d (left) adapted with permission from ref 21, Elsevier. Part e (left) adapted

with permission from ref 36, Wiley

Figure S4

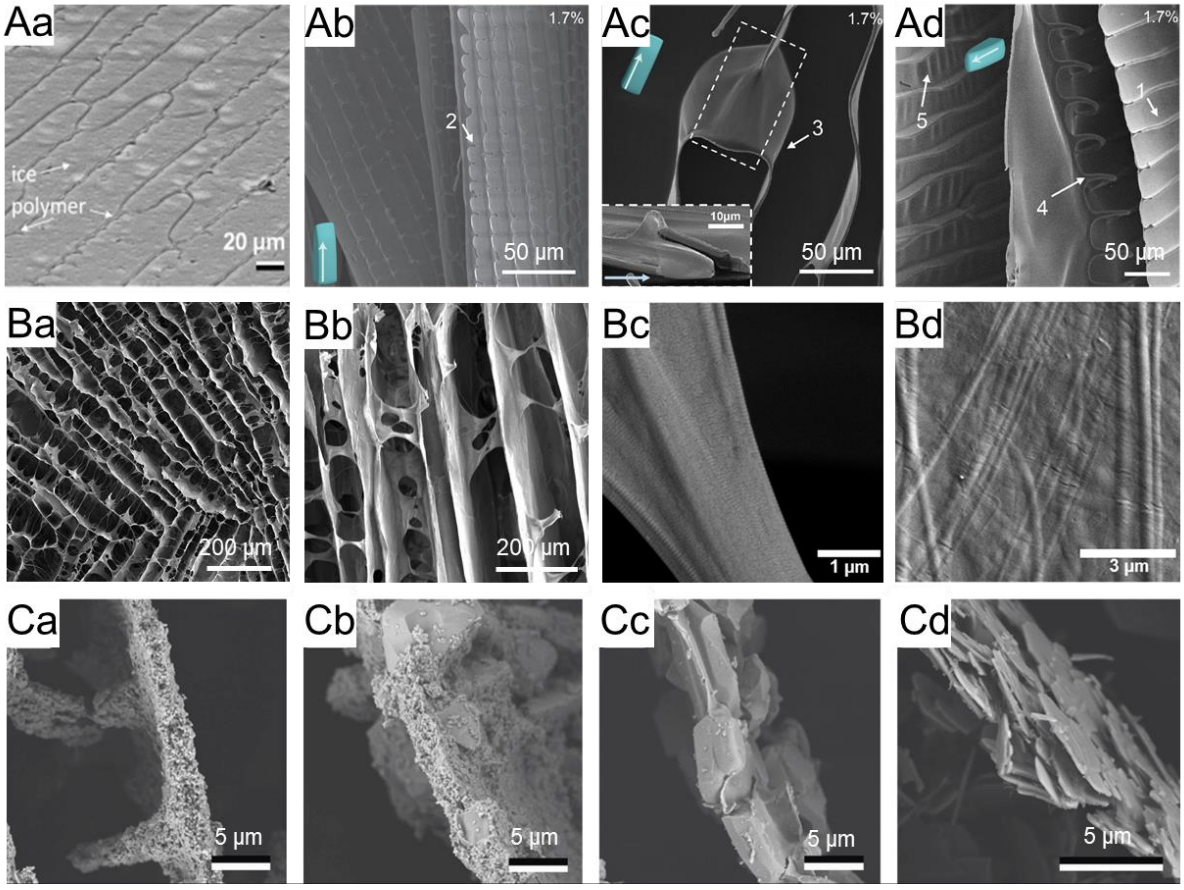

Experimentally Obtained Material Structures. (Aa) Transverse cross-section of still frozen ice-polymer composite with ice-templated polymer ridges.28 (Ab-Ad) Chitosan scaffold exhibiting the unilateral cell wall surface features 1-5 defined in Figure 1A.2 (Ba, Bb) Slurries containing fibrillar components for pillars and bridges between fibre mat-like cell walls.12,29 (CaCd) Particles more or less efficiently packed, depending on particle size distribution and shape.10 (Cd) Platelets or flakes assembled into a nacre-like structure.30 Part Aa reprinted with permission from ref 28, Elsevier. Parts Ab-Ad are reprinted from ref 2, CC BY 4.0 (https://creativecommons.org/licenses/by/4.0/). Part B re-printed with permission from ref 12, Elsevier. Part C adapted with permission from ref 30, Elsevier.

Figure S2

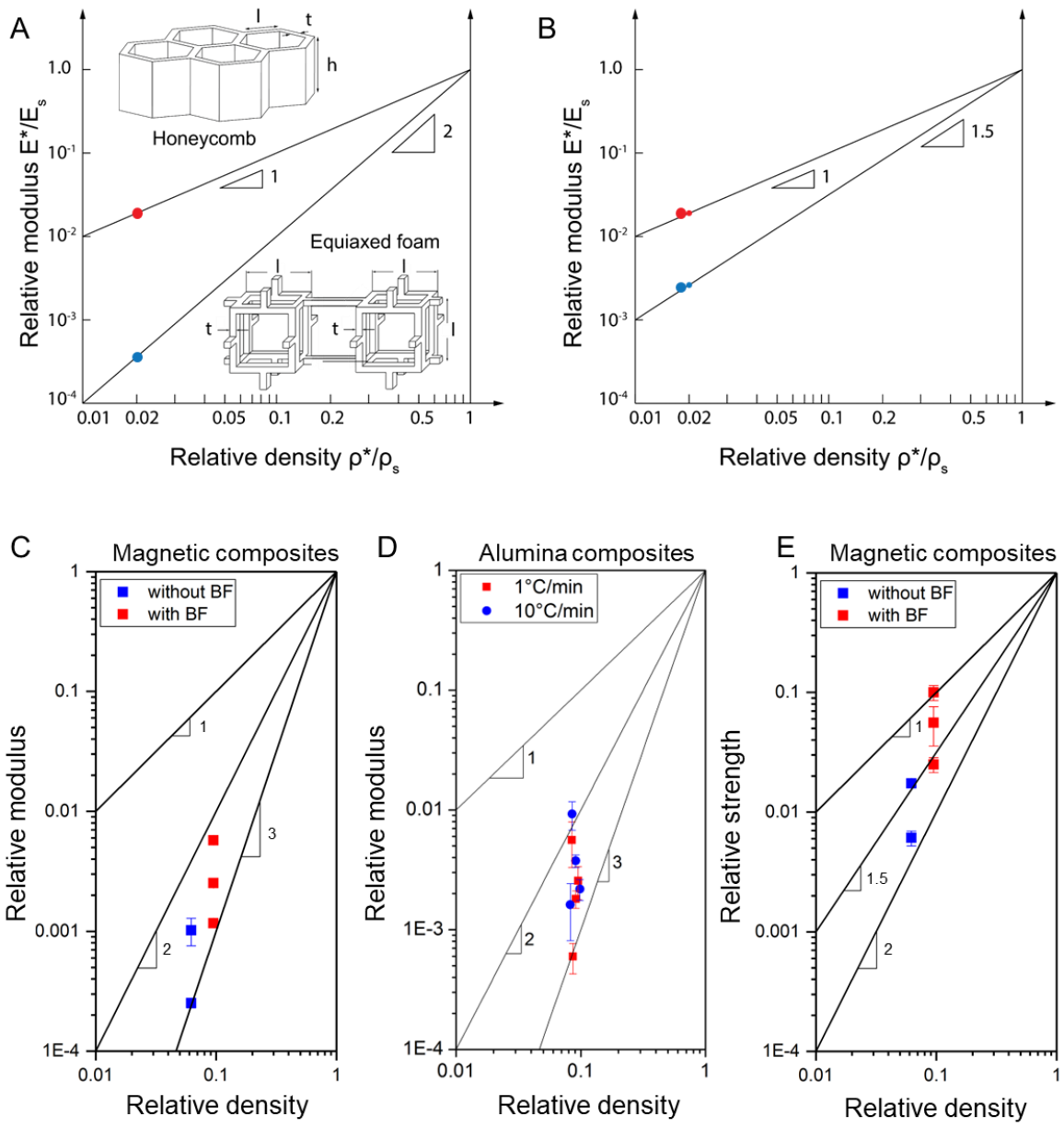

Mechanical Anisotropy – Gibson-Ashby Scaling Laws. Two types of cellular solids are compared: foams, in which the pores are more or less equiaxed, and honeycombs, in which the pores are unidirectional and aligned. The graphs illustrate how the (A) relative modulus and (B) relative strength of foams and honeycombs scale as a function of relative density, which is the density of the foam, r*, divided by the density of the solid, rs, from which it is made. Plots of (C) relative modulus and (E) relative strength versus their respective relative densities for magnetic Sendust flakes freeze cast in the presence and the absence of an externally applied field, and (D) relative modulus versus relative density for alumina ceramics freeze cast from spherical and platelet-like particles. The plots of C-E illustrate how significantly material performance can be improved by structural optimization. Parts A-B reprinted with permission from ref 37, Royal Society. Part A (inset) reprinted with permission from ref 10, Elsevier. Parts C-E adapted with permission from ref 35, Wiley.

Figure S6

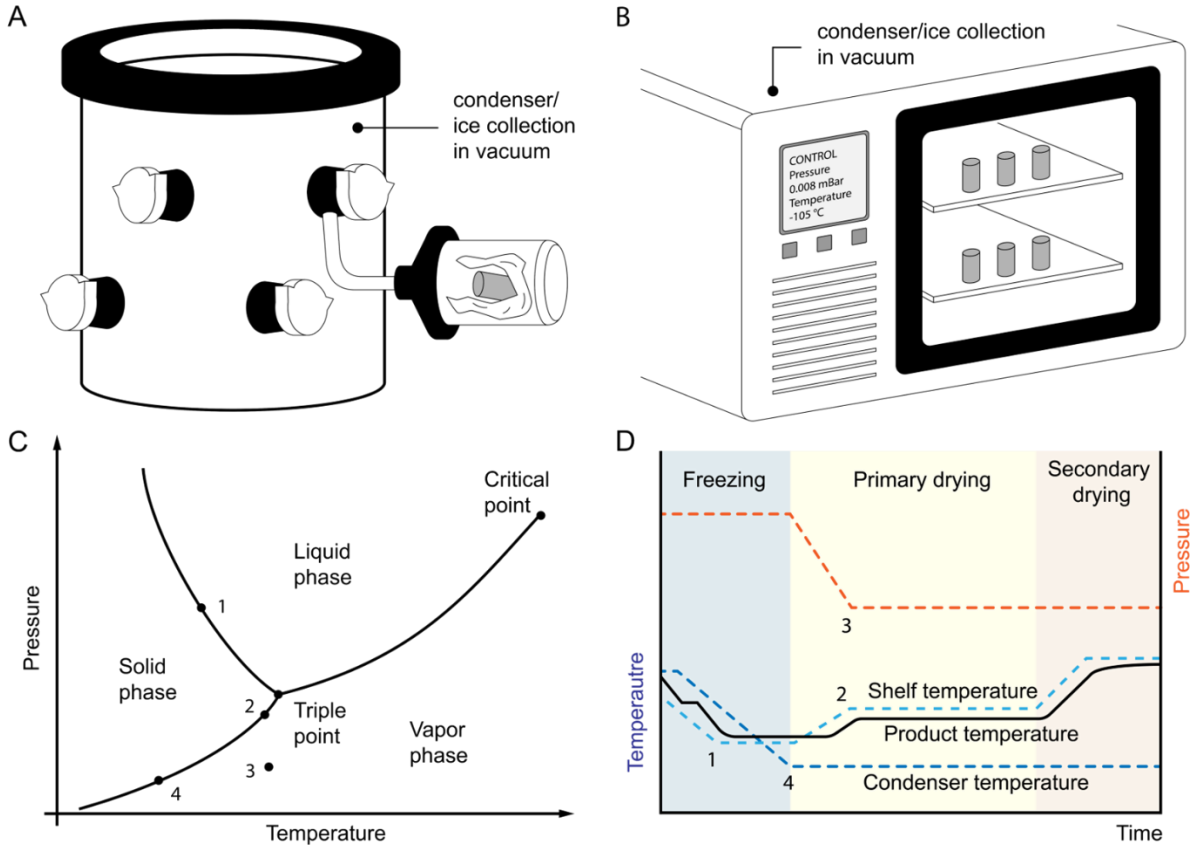

Lyophilization.3,4 (A) Schematic of a manifold lyophilizer, illustrating how flasks are attached to a port of the vacuum chamber which contains the cold trap (ice collector). (B) Schematic of a shelf lyophilizer. (C) A typical phase diagram illustrating the freeze-drying process. (D) A typical freeze-drying cycle for samples lyophilized in a shelf lyophilizer is depicted. (C, D) The fully solidified sample at a temperature of at least 20 °C below its eutectic or glass transition point (1) is placed in the flask or on the drying shelf. The sample temperature is raised but kept below this sample specific critical temperature (2) while the pressure is reduced to reach the sublimation line, which marks the conditions at which sublimation and with it the first lyophilization step starts. To increase the vapor pressure differential further, a higher vacuum is applied (3) and the ice collector temperature is lowered (4).

Figure S7

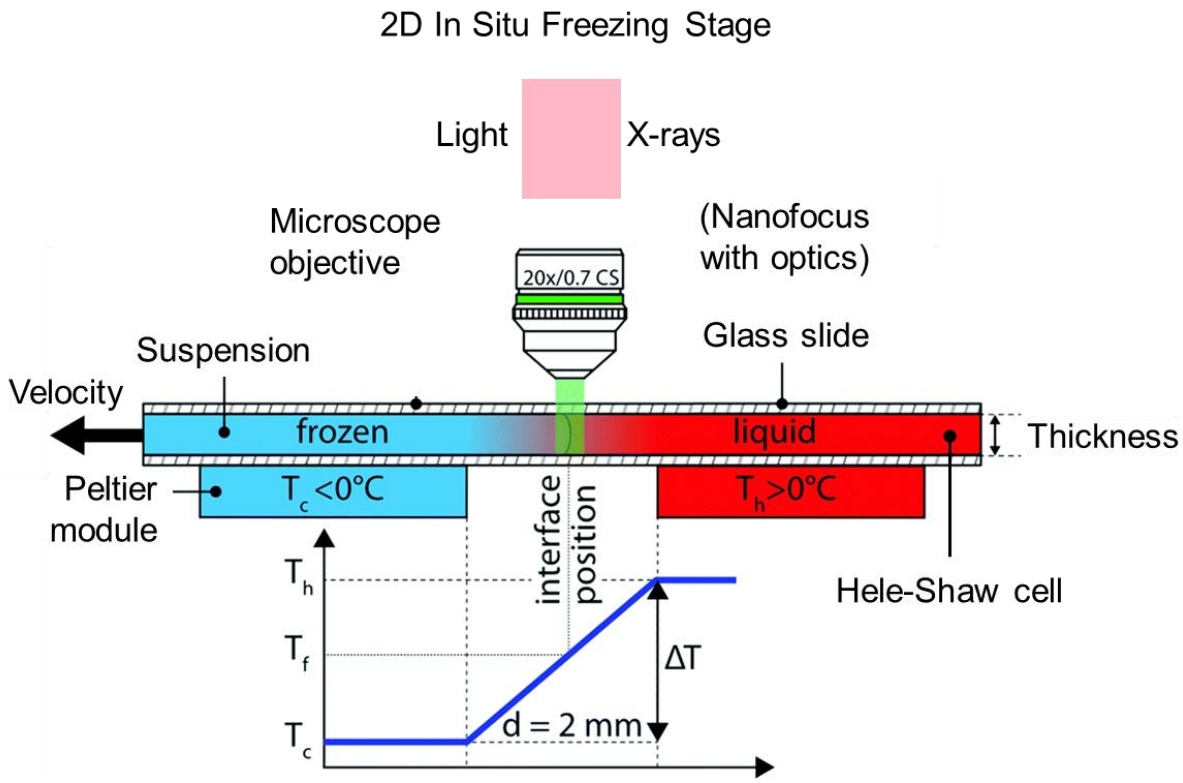

2D In Situ Freezing Stage. A thin layer of an aqueous solution or slurry is sandwiched between two glass slides or in a glass capillary (Hele-Shaw Cell). A defined thermal gradient is created between the two temperature zones through which the Hele-Shaw cell is moved at a controlled velocity achieving a well-defined cooling rate. The freezing behaviour in 2D is imaged under an optical or confocal microscope. 31–33 Adapted from ref 31, CC BY 4.0 (https://creativecommons.org/licenses/by/4.0/).

References

1. Kurz, W. & Fisher, D. J. *Fundamentals of solidification*. (Trans Tech Publications, 1998).
2. Yin, K. *et al.* Hierarchical Structure Formation by Crystal Growth-Front Instabilities During Ice Templating. *Proceedings of the National Academy of Sciences* **120**, e2210242120 (2023).
3. Labconco Corporation. *A Guide to Freeze Drying for the Laboratory*. (2010).
4. Buchi Corporation. *Freeze Drying Vol. 1 Basic Theory & Applications*. (2024).
5. Fennema, O. R. *Food chemistry*. vol. 76 (CRC Press, 1996).
6. Pinches, S. & Franks, G. V. Cracking during freeze-drying in dense freeze cast ceramics: Role of drying rate. *J Am Ceram Soc.* **106**, 5167–5177 (2023).
7. Yin, K., Divakar, P. & Wegst, U. G. K. Structure-property-processing correlations of longitudinal freeze-cast chitosan scaffolds for biomedical applications. *J Mech Behav Biomed Mater* **121**, 104589 (2021).
8. Caruso, I., Yin, K., Divakar, P. & Wegst, U. G. K. Tensile properties of freeze-cast collagen scaffolds: How processing conditions affect structure and performance in the dry and fully hydrated states. *Journal of the Mechanical Behavior of Biomedical Materials* 105897 (2023)
9. Bai, H., Chen, Y., Delattre, B., Tomsia, A. P. & Ritchie, R. O. Bioinspired large-scale aligned porous materials assembled with dual temperature gradients. *Science Advances* **1**, e1500849 (2015).
10. Hunger, P. M., Donius, A. E. & Wegst, U. G. K. Structure–property-processing correlations in freeze-cast composite scaffolds. *Acta Biomaterialia* **9**, 6338–6348 (2013).

11. Tang, Y., Miao, Q., Qiu, S., Zhao, K. & Hu, L. Novel freeze-casting fabrication of aligned lamellar porous alumina with a centrosymmetric structure. *Journal of the European Ceramic Society* **34**, 4077–4082 (2014).
12. Divakar, P., Yin, K. & Wegst, U. G. K. Anisotropic freeze-cast collagen scaffolds for tissue regeneration: How processing conditions affect structure and properties in the dry and fully hydrated states. *Journal of the Mechanical Behavior of Biomedical Materials* **90**, 350–364 (2019).
13. Tian, L. *et al.* Tailoring centripetal metamaterial with superelasticity and negative Poisson's ratio for organic solvents adsorption. *Science Advances* **8**, eabo1014 (2022).
14. Li, D., Bu, X., Xu, Z., Luo, Y. & Bai, H. Bioinspired Multifunctional Cellular Plastics with a Negative Poisson's Ratio for High Energy Dissipation. *Advanced Materials* **32**, 2001222 (2020).
15. Porter, M. M. *et al.* Magnetic freeze casting inspired by nature. *Materials Science and Engineering: A* **556**, 741–750 (2012).
16. Tang, Y. F., Zhao, K., Wei, J. Q. & Qin, Y. S. Fabrication of aligned lamellar porous alumina using directional solidification of aqueous slurries with an applied electrostatic field. *Journal of the European Ceramic Society* **30**, 1963–1965 (2010).
17. Tang, Y., Qiu, S., Miao, Q. & Wu, C. Fabrication of lamellar porous alumina with axisymmetric structure by directional solidification with applied electric and magnetic fields. *Journal of the European Ceramic Society* **36**, 1233–1240 (2016).
18. Jha, P. K., Xanthakis, E., Jury, V. & Le-Bail, A. An Overview on Magnetic Field and Electric Field Interactions with Ice Crystallisation; Application in the Case of Frozen Food. *Crystals* **7**, 299 (2017).

19. Ogden, T. A., Prisbrey, M., Nelson, I., Raeymaekers, B. & Naleway, S. E. Ultrasound freeze casting: Fabricating bioinspired porous scaffolds through combining freeze casting and ultrasound directed self-assembly. *Materials & Design* **164**, 107561 (2019).
20. Yin, K., Mylo, M. D., Speck, T. & Wegst, U. G. K. 2D and 3D graphical datasets for bamboo-inspired tubular scaffolds with functional gradients: micrographs and tomograms. *Data Brief* **31**, 105870 (2020).
21. Yin, K., Mylo, M. D., Speck, T. & Wegst, U. G. K. Bamboo-inspired tubular scaffolds with functional gradients. *J Mech Behav Biomed Mater* **110**, 103826 (2020).
22. Yu, R. *et al.* Graphene Oxide/Chitosan Aerogel Microspheres with Honeycomb-Cobweb and Radially Oriented Microchannel Structures for Broad-Spectrum and Rapid Adsorption of Water Contaminants. *ACS Appl. Mater. Interfaces* **9**, 21809–21819 (2017).
23. Cui, Y., Gong, H., Wang, Y., Li, D. & Bai, H. A Thermally Insulating Textile Inspired by Polar Bear Hair. *Advanced Materials* **30**, 1706807 (2018).
24. Sofie, S. W. Fabrication of Functionally Graded and Aligned Porosity in Thin Ceramic Substrates With the Novel Freeze–Tape-Casting Process. *Journal of the American Ceramic Society* **90**, 2024–2031 (2007).
25. Shen, H. *et al.* Scalable Freeze-Tape-Casting Fabrication and Pore Structure Analysis of 3D LLZO Solid-State Electrolytes. *ACS Appl. Mater. Interfaces* **12**, 3494–3501 (2020).
26. Barnett, E., Angeles, J., Pasini, D. & Sijpkes, P. Robot-assisted Rapid Prototyping for ice structures. in *2009 IEEE International Conference on Robotics and Automation* 146–151 (2009). doi:10.1109/ROBOT.2009.5152317.
27. Zhang, Q. *et al.* 3D Printing of Graphene Aerogels. *Small* **12**, 1702–1708 (2016).
28. Donius, A. E. *et al.* Cryogenic EBSD reveals structure of directionally solidified ice–polymer composite. *Materials Characterization* **93**, 184–190 (2014).

29. Yin, K., Divakar, P. & Wegst, U. G. K. Plant-Derived Nanocellulose as Structural and Mechanical Reinforcement of Freeze-Cast Chitosan Scaffolds for Biomedical Applications. *Biomacromolecules* **20**, 3733–3745 (2019).
30. Hunger, P. M., Donius, A. E. & Wegst, U. G. K. Platelets self-assemble into porous nacre during freeze casting. *Journal of the Mechanical Behavior of Biomedical Materials* **19**, 87–93 (2013).
31. Dedovets, D. & Deville, S. Multiphase imaging of freezing particle suspensions by confocal microscopy. *Journal of the European Ceramic Society* **38**, 2687–2693 (2018).
32. Dedovets, D., Monteux, C. & Deville, S. Five-dimensional imaging of freezing emulsions with solute effects. *Science* **360**, 303–306 (2018).
33. Dedovets, D., Monteux, C. & Deville, S. A temperature-controlled stage for laser scanning confocal microscopy and case studies in materials science. *Ultramicroscopy* **195**,
1–11 (2018).